

Photoionized Herbig-Haro objects in the Orion Nebula through VLT's deep spectroscopy I: HH529 II-III

J. E. Méndez-Delgado^{1,2} , C. Esteban^{1,2}, J. García-Rojas^{1,2}, W. J. Henney³
and K. Z. Arellano-Córdova¹

¹Instituto de Astrofísica de Canarias (IAC), E-38205 La Laguna, Spain

²Departamento de Astrofísica, Universidad de La Laguna, E-38206 La Laguna, Spain

³Instituto de Radioastronomía y Astrofísica, Universidad Nacional Autónoma de México, Apartado Postal 3-72, 58090 Morelia, Michoacán, México

Accepted XXX. Received YYY; in original form ZZZ

ABSTRACT

This is the abstract.

Key words: ISM:Abundances – ISM: Herbig–Haro objects – ISM: individual: Orion Nebula – ISM: individual: HH 529III.

1 INTRODUCTION

Herbig-Haro objects are shocks associated to

2 OBSERVATIONS AND DATA REDUCTION

The observations were made under photometric conditions during the November 28 and 29, 2013 nights using the Ultraviolet Visual Echelle Spectrograph (UVES) (D'Odorico et al. 2000) in the UT2 (Kueyen) of the Very Large Telescope (VLT) in Cerro Paranal, Chile. The slit position was centred at the coordinates RA(J2000)=05^h35^m16^s.80, DEC(J2000)=−05°23'57.48'', having a length of 10 arcsec in the blue arm and 12 arcsec in the red arm looking for an adequate interorder separation. Table 1 shows the observational features of the night. The slit width was set to 1 arcsec, which is equivalent to an effective spectral resolution $\lambda/\Delta\lambda \approx 40000$ (6.5 km s^{−1}). To perform the flux calibration of the data, three exposures of 150s of the standard star GD71 (Moehler et al. 2014a,b) were taken under similar conditions of seeing and airmass than the science observations during the same night. The spatial coverage of the slit is shown in Fig. 1.

Our observations cover the spectral range between 3100–10420 Å, using standard features for two dichroic settings in UVES. Dichroic#1 setting split the light in two wavelengths ranges: from 3100 to 3885 Å in the blue arm and from 4785 to 6805 Å in the red one, while the dichroic#2 setting covers from 3750 to 4995 Å in the blue arm and from 6700 to 10420 Å in the red one. However, in our high resolution and wide spectral range observations, there are some observational gaps. The red arm use two CCDs, and due to their physical separation, spectral ranges 5773–5833 Å and 8540–8650 Å could not be observed. Additionally there are some narrow gaps that could not be observed in the redmost part of the red

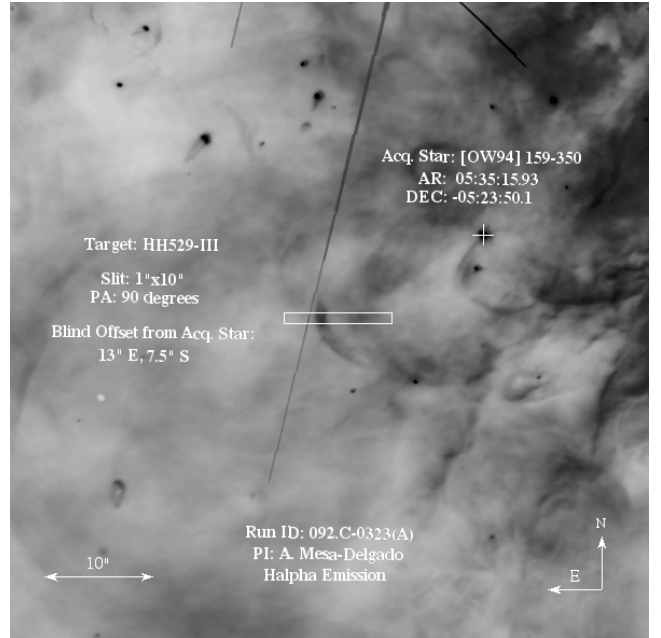


Figure 1. H α Hubble Space Telescope (HST) image of the central part of the Orion Nebula just at the south of θ^1 Ori C. Our slit position is indicated.

arm in the dichroic#2 setting because the spectral orders could not fit entirely within the CCD. These range are ~8911–8913 Å, 9042–9046 Å, 9178–9182 Å, 9317–9323 Å, 9460–9469 Å, 9608–9619 Å, 9760–9774 Å, 9918–9935 Å, 10080–10100 Å and 10248–10271 Å.

We reduced the spectra using a combination of tasks from the public ESO UVES pipeline (Ballester et al. 2000) under the GASGANO graphic user interface, and tasks built by ourselves based

* E-mail: jemd@iac.es

Table 1. UVES @VLT Observational features.

Date	$\Delta\lambda$ (Å)	Exp. time (s)	Seeing (arcsec)	Airmass
2013-11-29	3100-3885	5, 3×180	0.79	1.20
2013-11-29	3750-4995	5, 3×600	0.65	1.14
2013-11-29	4785-6805	5, 3×180	0.79	1.20
2013-11-29	6700-10420	5, 3×600	0.65	1.14

Table 2. HST observations used in proper motion study

Date	Program	Camera, CCD, Filter	Reference
1995-03	5469	WFPC2, PC, F656N	Bally et al. (1998)
2005-04	10246	ACS, WFC, F658N	Roberto et al. (2013)
2015-01	13419	WFC3, UVIS, F656N	Bally & Reipurth (2018)

on IRAF¹ (Tody 1993) and several python packages. Firstly, we used IRAF tasks FIXPIX and IMCOMBINE to mask known bad pixels in our images and to combine all the images with the same exposure time. Then, we used the ESO UVES pipeline for bias subtraction, background subtraction, aperture extraction, flat-fielding and wavelength calibration. As a product, we obtained a 2D spectrum of science for each arm in each dichroic setting without flux calibration. We followed the same procedure for GD 71 but extracting both a 2D and a 1D spectrum. The 2D spectrum of the calibration star helps us to perceive the presence of faint sky lines which are also present in the science spectra.

One crucial step of the data reduction is to perform adequate cuts in the spatial direction on the slit to extract 1D spectra. We chose these spatial cuts in order to study in detail each observed velocity component and trying to maximise the shock/nebular emission ratio. We relied on the [Fe III] $\lambda 4658$ line, which is relatively bright in the shock components to delimit the cuts. The seeing conditions permit us to separate two high-velocity components that can be distinguish (see Figure 2). One of them have a "ball shape" while the other presents an elongated distribution along the spectral axis. This is related with the morphology of the outflow system of HH529 (firstly identified by Bally et al. 2000). This system shows three notorious bright arcs, identified by the numbers I, II and III, being numbered by their position from west to east (O'Dell & Henney 2008). However, the system is more complex than just three homogeneous arcs as we will analyze in § 10. The length in the spatial direction covered by each cut is 1.23 arcsec, 4.43 arcsec, 2.46 arcsec and 1.23 arcsec for cuts 1, 2, 3 and 4, respectively. This numbering has been defined from west to east in the spatial position (see Fig. 1). Cut 1 is at the bottom and cut 4 at the top of Fig. 2. In the context of the nomenclature given by O'Dell & Henney (2008), the high-velocity component of the cut 3 corresponds to HH529III, while that of cut 2 is HH529II. We have also defined an additional 1D spectrum, labelled as "combined cuts". This was created by adding the flux of the lines measured in all the components of all cuts. The lines included in this spectrum were those detected and identified in the nebular component of all cuts. The spectrum of the combined cuts is useful to analyze the effect that a non-resolved shock component would have in the properties of a low-resolution spectrum. We used the Python-based Astropy package (Astropy Collaboration et al. 2013; Price-Whelan et al. 2018) to obtain 1D spectra for each cut,

doing the conversion between the different pixel scale of the CCDs in the blue and the red arm. Each spatial cut covers an area larger than the seeing size during the observations, as it is shown in Table 1. We used the IRAF tasks STANDARD, SENSFUNC and CALIBRATE to perform the flux calibration of each 1D spectra of all cuts. The radial velocity correction was made using Astropy.

For the determination of the proper motion of HH529, we take advantage of the 20 years of archival *Hubble Space Telescope* (*HST*) imaging that is now available. We employ three epochs of observations, as detailed in Table 2. All data was downloaded from the Barbara A. Mikulski Archive for Space Telescopes².

3 LINE INTENSITIES AND REDDENING

We used the SPLOT task from IRAF to measure line intensities and estimate their uncertainties. We applied a double Gaussian profile fit for the nebular and shock component, delimiting the continuum by eye. For each measured line, we estimate the value of the continuum and its *rms* on each side to propagate uncertainties associated to the flux measurement. In case of evident line blending, we applied as many Gaussians as necessary to properly reproduce the line profile. As it was mentioned in § 2, the observed wavelength range (3100-10420 Å) was covered in 4 sections (two dichroic settings splitting the light into two spectrograph arms). Between each section, there is an overlapping zone from where we used the most intense lines to normalize the entire spectrum with respect to H β . The measured flux of H I $\lambda 3835$, [O III] $\lambda 4959$ and [S II] $\lambda 6731$ lines were used to normalize the spectra from the blue arm of dichroic#1, the red arm of dichroic#1 and the red arm of dichroic#2 settings respectively (H β is in the blue arm of dichroic#2 setting). This normalization eliminates the differences in flux between each part of the spectrum due to the different pixel scale between the blue and the red arms.

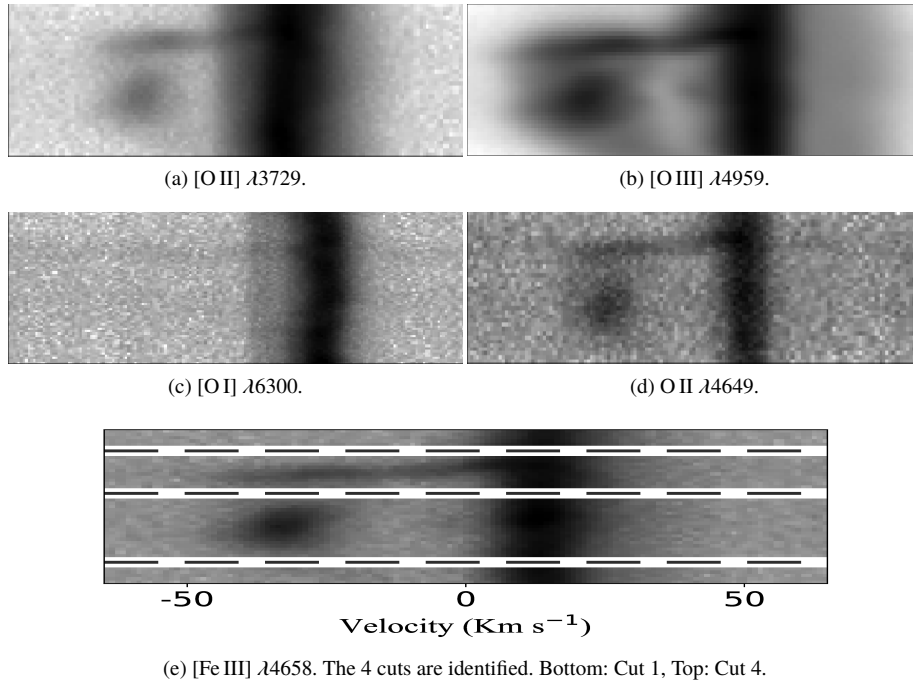
The emission lines were corrected for reddening using Eq. (1), where $f(\lambda)$ is the adopted extinction curve from Blagrave et al. (2007), normalized to H β . We calculate the reddening coefficient, $c(H\beta)$, by using the ratios of H ϵ , H δ , H γ and H α Balmer lines and the P12, P11, P10, P9 Paschen lines with respect to H β and the emissivity coefficients of Storey & Hummer (1995). The final adopted $c(H\beta)$ value is the weighted average value obtained from the aforementioned Balmer and Paschen lines and is shown in Table 3 for both the shock and nebular components. The selected HI lines are free of line-blending or telluric absorptions that may affect the determination of $c(H\beta)$. Despite there are more isolated and bright Balmer and Paschen lines available in the spectra, we did not use them since their emission depart from the case B values. This behaviour was reported previously in the Orion Nebula (Mesa-Delgado et al. 2009), the Magellanic Clouds (Domínguez-Guzmán et al. 2019) and in several Planetary Nebulae (PNe Rodríguez 2020).

$$\frac{I(\lambda)}{I(H\beta)} = \frac{F(\lambda)}{F(H\beta)} \times 10^{c(H\beta)f(\lambda)}. \quad (1)$$

Blagrave et al. (2006) observed the zone of the Orion Nebula that includes HH529III using the 4m Blanco telescope at the Cerro Tololo Inter-American Observatory, covering a more limited spectral region (3500-7500 Å). A comparison between the reddening corrected intensity of lines between their nebular component and the nebular component of cut 2 from this work is shown in Fig. 3. From Blagrave et al. (2006) spectra, we have excluded lines with

¹ IRAF is distributed by National Optical Astronomy Observatory, which is operated by Association of Universities for Research in Astronomy, under cooperative agreement with the National Science Foundation

² MAST, <https://archive.stsci.edu/>

Figure 2. Sample of emission lines in the 2D spectrum. All images are centred at λ_0 . The different cuts are shown in the bottom image.**Table 3.** Reddening coefficients for each component of each cut.

	c(Hβ)	
	Shock	Nebula
Cut 1	-	0.82 ± 0.02
Cut 2	0.90 ± 0.03	0.83 ± 0.02
Cut 3	0.89 ± 0.05	0.84 ± 0.03
Cut 4	-	0.83 ± 0.02
Combined cuts	-	0.85 ± 0.02

notes of "Avg, blend or small FWHM" for our comparison, due to their usual inconsistent fluxes. For example, [Ne III] λ3967.46 line, marked with an "Avg", is inconsistent with the measured intensity of [Ne III]λ3868.75, since their observed ratio is 2.02, quite far from the theoretical one of 3.29. A least squares linear fit yields the relationship $y = 1.00 (\pm 0.01) x + 0.05 (\pm 0.02)$, indicating that the spectrum of Blaggrave et al. (2006), shows systematically slightly larger intensity line ratios than ours. This is quite noticeable in the spectral region of the high-level Balmer lines (3660–3720Å), where this difference can reach up to 50%. This large difference may be due to the relative weakness of these lines, coupled with the abrupt change in the continuum due to the closeness of the Balmer discontinuity. For other lines, the slight discrepant tendency disappears considering an increase of about 10% in the intensity of I(Hβ). This possible underestimation of I(Hβ) in the Blaggrave et al. (2006) spectrum for the nebular component is the most likely explanation considering that the intensity ratios between other bright H I lines are consistent with the theoretical ones and not those with respect to Hβ. We did not compare their shock component with ours, because their slit position is slightly different than ours. In addition to this, the seeing conditions of 2–2.5 arcsec of the observations of Blaggrave et al. (2006) do not allow them to adequately separate HH529II and HH529III.

Fig. 4 shows Hβ in the different components of the different cuts. As it can be seen, the reddest component (corresponding to

the nebular component) has practically the same profile in all cuts except in cut 3, where the line is broadened by the presence of greater velocity dispersion in the high velocity component. This is quite evident from Fig. 2, where the shock component of cut 3 is clearly seen as an elongated arm. The complexity of the velocity components of HH529 is discussed in higher detail in §10.

Line identifications were consistently made by adopting the theoretical wavelengths of Peter Van Hoof's latest Atomic Line List v2.05b21³ (Van Hoof 2018) for all ions except for Cl III, Cl IV and Ne III due to some inconsistencies found (see §9 for a detailed discussion). Our spectra are very extensive and are attached in the online annexes to this article. In the nebular components, 514, 633, 579 and 522 lines were measured for cuts 1, 2, 3 and 4, respectively. For HH529II, 376 lines were detected, while for HH529III they were 245. In the case of a multi-line blend, this was counted as one detection.

4 PHYSICAL CONDITIONS

4.1 Physical conditions based on Collisionally Excited Lines

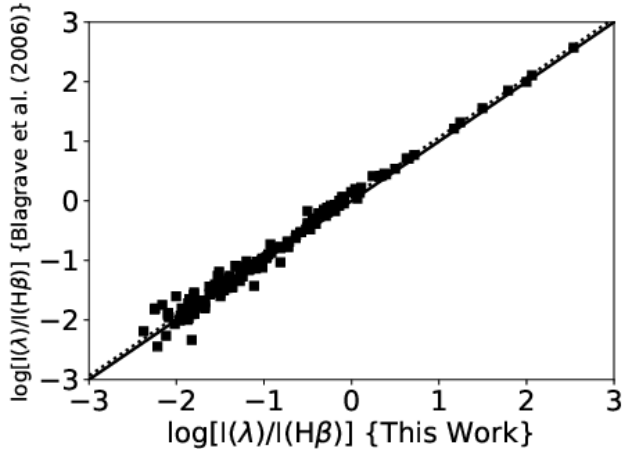
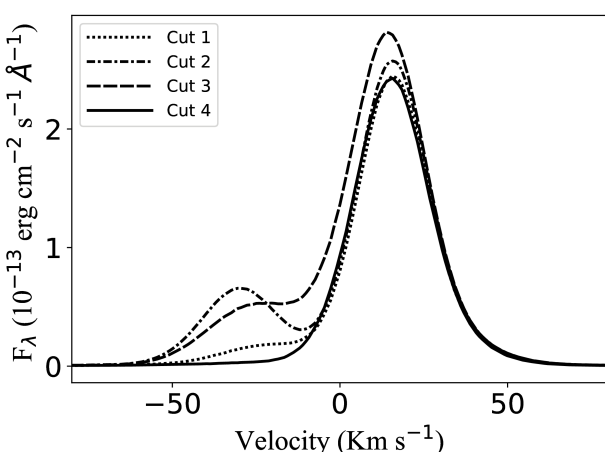
We use PyNeb (version 1.1.10) (Luridiana et al. 2015) and the updated atomic dataset listed in Table 4 to calculate physical conditions based on the intensity ratios of collisionally excited lines (CELs) from different ions.

The first step was to test all the intensity ratios of CELs that can serve as a temperature or density diagnostic using the PyNeb's task getCrossTemDen. This task uses two line ratios at the same time: one as density diagnostic and the other one for temperature, giving their convergence to a pair n_e, T_e as a result. We tried all possible permutations for all the available diagnostics in all components from all cuts. We only discarded the use of lines strongly affected

³ <http://www.pa.uky.edu/peter/newpage/>

Table 4. Atomic data set used for collisionally excited lines.

Ion	Transition Probabilities	Collision Strengths
O ⁺	Froese Fischer & Tachiev (2004)	Kisielius et al. (2009)
O ²⁺	Wiese et al. (1996), Storey & Zeippen (2000)	Storey et al. (2014)
N ⁺	Froese Fischer & Tachiev (2004)	Tayal (2011)
Ne ²⁺	McLaughlin et al. (2011)	McLaughlin et al. (2011)
S ⁺	Podobedova et al. (2009)	Tayal & Zatsarinny (2010)
S ²⁺	Podobedova et al. (2009)	Grieve et al. (2014)
Cl ⁺	Mendoza & Zeippen (1983)	Tayal (2004)
Cl ²⁺	Fritzsche et al. (1999)	Butler & Zeippen (1989)
Cl ³⁺	Kaufman & Sugar (1986), Mendoza & Zeippen (1982b), Ellis & Martinson (1984)	Galavis et al. (1995)
Ar ²⁺	Mendoza (1983), Kaufman & Sugar (1986)	Galavis, Mendoza & Zeippen (1995)
Ar ³⁺	Mendoza & Zeippen (1982a)	Ramsbottom & Bell (1997)
Fe ²⁺	Quinet (1996), Johansson et al. (2000)	Zhang, Hong Lin (1996)
Fe ³⁺	Froese Fischer et al. (2008)	Zhang & Pradhan (1997)
Ni ²⁺	Bautista (2001)	Bautista (2001)

**Figure 3.** Comparison between the intensity of the lines corrected of reddening in the nebular component of cut 2 and the nebular component of Blagrade et al. (2006). The dotted line represents the linear fit $y = 1.00x + 0.05$, while the solid line represents $y = x$.**Figure 4.** Line profile of H β in the spectra of the different extracted cuts.**Table 5.** Effective recombination coefficients used for recombination lines.

Ion	Reference
H ⁺	Storey & Hummer (1995)
He ⁺	Porter et al. (2012, 2013)
O ⁺	Pequignot et al. (1991)
O ²⁺	Storey et al. (2017)
C ²⁺	Davey et al. (2000)
Ne ²⁺	Kisielius et al. (1998)

Table 6. Critical densities of the usual density diagnostics at $T_e = 10000$ K.

Ion	$\lambda(\text{\AA})$	$n_{\text{crit}}(\text{cm}^{-3})$
[O II]	3729, 3726	$1.30 \times 10^3, 4.06 \times 10^3$
[S II]	6731, 6716	$3.06 \times 10^3, 1.16 \times 10^3$
[Cl III]	5538, 5518	$3.57 \times 10^4, 7.23 \times 10^3$
[Fe III]	4658, 4701	$5.17 \times 10^6, 3.09 \times 10^6$
[Ar IV]	4740, 4711	$1.26 \times 10^5, 1.39 \times 10^4$

by blends, telluric emissions and/or absorptions or reflections in the optical system of the spectrograph. We did not consider the n_e diagnostic based on the [N I] $\lambda\lambda 5198/5200$ doublet owing to their unphysical meaning in the Orion Nebula (Ferland et al. 2012).

Diagnostics based on [Ni III] λ_1/λ_2 , where $\lambda_1, \lambda_2 \in [6000, 6534, 6682, 6797, 6946, 7890]$ and $\lambda_1 \neq \lambda_2$ do not give any useful physical information since they either did not converge or showed convergences at values highly discordant with the other diagnostics. This will be commented in greater detail in § 5.1.2. Another interesting case is on the diagnostics based on [Fe III] λ_1/λ_2 , where $\lambda_1, \lambda_2 \in [4658, 4702, 4734, 4881, 5011, 4925, 4987, 5271]$ and $\lambda_1 \neq \lambda_2$. With the exception of [Fe III] 4658/4702, all the diagnostics converge in a fairly wide range of physical conditions. This is due to the ambivalence and/or high dependence of these ratios on both density and temperature. This will be discussed in § 4.2.

After the initial scan, we define the ratios we consider are good indicators of electron density and temperature. Then we use Monte Carlo simulations with 1000 points to estimate uncertainties in the physical conditions given by the PyNeb's `getCrossTempDen` task. For example, with [O III] $\lambda 4363/\lambda 4959+5007$ as a temperature indicator and [Cl III] $\lambda 5538/\lambda 5518$, [Fe III] $\lambda 4658/\lambda 4702$, [O II] $\lambda 3726/\lambda 3729$, [S II] $\lambda 6731/\lambda 6716$, [Ar IV] $\lambda 4740/\lambda 4711$ as density diagnostics, we estimate the convergence in T_e and n_e and their uncertainties in every case. The central value of T_e or n_e corre-

Table 7. Physical conditions determined from several diagnostics.

Diagnostic	Cut 1 Nebula	Cut 2 Shock	Cut 2 Nebula	Shock	Cut 3 Low Velocity Shock+Nebula	Cut 4 Nebula	Combined Cuts
n_e (cm ⁻³)							
[O II] $\lambda 3726/\lambda 3729$	5460 ⁺¹⁰⁰⁰ ₋₇₅₀	10570 ⁺³⁶⁸⁰ ₋₂₄₂₀	5220 ⁺⁹⁶⁰ ₋₇₂₀	18020 ⁺¹⁷¹⁷⁰ ₋₆₉₃₀	5530 ⁺¹⁰⁰⁰ ₋₈₀₀	5070 ⁺⁸⁸⁰ ₋₇₁₀	5530 ⁺⁹⁹⁰ ₋₈₁₀
[S II] $\lambda 6731/\lambda 6716$	4230 ⁺¹⁵⁰⁰ ₋₁₃₀₀	9390 ⁺¹⁰¹⁷⁰ ₋₃₂₅₀	4160 ⁺¹⁵⁷⁰ ₋₁₀₄₀	13130 ⁺¹⁵⁸²⁰ ₋₆₅₅₀	4130 ⁺²⁰²⁰ ₋₁₁₅₀	4160 ⁺¹⁴⁰⁰ ₋₉₆₀	4510 ⁺²²⁷⁰ ₋₁₁₅₀
[Cl III] $\lambda 5538/\lambda 5518$	7020 ⁺³⁸⁰⁰ ₋₉₀₀	8170 ⁺¹⁸¹⁰ ₋₅₁₀	6670 ⁺⁸⁶⁰ ₋₈₆₀	15040 ⁺⁴⁴⁹⁰ ₋₄₄₉₀	7370 ⁺¹¹²⁰ ₋₁₁₂₀	7000 ⁺⁹⁶⁰ ₋₉₀₀	7420 ⁺¹¹⁰⁰ ₋₁₁₀₀
[Fe III] $\lambda 4658/\lambda 4702$	9260 ⁺³⁷⁰⁰ ₋₂₈₉₀	12390 ⁺⁵⁰¹⁰ ₋₃₄₆₀	8990 ⁺²⁸⁴⁰ ₋₂₃₅₀	33800 ⁺³³⁸²⁰ ₋₁₀₅₃₀	10490 ⁺⁴²⁴⁰ ₋₃₀₉₀	8340 ⁺³⁶²⁰ ₋₂₅₃₀	9510 ⁺³⁷⁵⁰ ₋₂₇₅₀
[Ar IV] $\lambda 4740/\lambda 4711$	4480 ⁺¹⁷⁰⁰ ₋₁₆₄₀	6410 ⁺¹⁹⁰⁰ ₋₁₈₈₀	5920 ⁺⁹⁸⁰ ₋₉₄₀	15050 ⁺¹³³⁰⁰ ₋₉₂₄₀	6400 ⁺¹⁶⁹⁰ ₋₁₆₆₀	5460 ⁺¹⁰⁰⁰ ₋₁₀₅₀	6580 ⁺²⁰⁰⁰ ₋₁₈₇₀
O II*	4710 ± 710	3490 ± 340	4390 ± 400	3600 ± 850	4920 ± 550	4350 ± 610	5420 ± 690
[Fe III]*	8530 ± 1050	11880 ± 1860	9430 ± 1010	44090 ± 7580	8530 ± 1160	9020 ± 1170	10360 ± 1410
Adopted	5830 ± 1210	11880 ± 1860	5870 ± 970	44090 ± 7580	6180 ± 1220	5650 ± 1030	6290 ± 1130
T_e (K)							
T(H I) _{Balmer}	-	-	-	-	-	-	7520 ± 790
T(H I) _{Paschen}	-	-	-	-	-	-	7550 ± 1160
T(He I)	8280 ⁺⁵²⁰ ₋₅₇₀	7200 ± 550	8060 ⁺⁵⁴⁰ ₋₅₁₀	7340 ± 710	8090 ± 530	7390 ⁺⁴⁷⁰ ₋₅₈₀	7690 ⁺⁵⁰⁰ ₋₅₁₀
[N II] $\lambda 5755/\lambda 6584$	9910 ± 250	10150 ⁺⁵⁷⁰ ₋₅₁₀	9850 ± 240	10020 ⁺⁷⁴⁰ ₋₆₅₀	10060 ⁺²⁶⁰ ₋₂₈₀	9860 ⁺²⁷⁰ ₋₂₇₀	9990 ⁺²⁵⁰ ₋₂₇₀
[O II] $\lambda\lambda 3726+29/\lambda\lambda 7319+20+30+31$	10340 ⁺¹³³⁰ ₋₉₄₀	-	-	-	-	11230 ⁺¹³³⁰ ₋₁₁₁₀	10910 ⁺¹³²⁰ ₋₉₅₀
[S II] $\lambda\lambda 4069+76/\lambda\lambda 6716+31$	11430 ⁺³²⁹⁰ ₋₁₈₇₀	-	11070 ⁺²⁴²⁰ ₋₁₄₅₀	-	10550 ⁺²⁴⁵⁰ ₋₁₅₇₀	10790 ⁺²³⁴⁰ ₋₁₄₇₀	11000 ⁺²⁵¹⁰ ₋₁₆₀₀
[O III] $\lambda 4363/\lambda 4959+5007$	8430 ± 90	8240 ± 80	8410 ⁺⁹⁰ ₋₁₂₀	8500 ⁺¹¹⁰ ₋₁₂₀	8510 ± 90	8320 ± 90	8450 ⁺⁸⁰ ₋₉₀
[S III] $\lambda 6312/\lambda 9069+9531$	9220 ⁺²⁹⁰ ₋₃₃₀	8670 ± 310	8990 ⁺²⁹⁰ ₋₃₃₀	8960 ⁺¹⁷⁰ ₋₅₀₀	8920 ⁺³³⁰ ₋₃₀₀	8850 ⁺²⁹⁰ ₋₃₂₀	8970 ⁺²⁸⁰ ₋₂₉₀
[Ar III] $\lambda 5192/\lambda 7136+7751$	8280 ⁺²⁸⁰ ₋₃₁₀	8620 ⁺⁵⁰⁰ ₋₅₄₀	8390 ⁺²²⁰ ₋₂₈₀	-	8250 ⁺²⁶⁰ ₋₂₉₀	8280 ⁺³⁸⁰ ₋₄₂₀	8270 ⁺²⁸⁰ ₋₃₂₀
O II*	-	-	9350 ± 1090	-	-	-	-
[Fe III]*	7800 ± 800	8500 ± 1050	8450 ± 730	8440 ± 2260	7600 ± 710	7350 ± 590	8440 ± 710
T_e (low) Adopted	9930 ± 140	10150⁺⁵⁷⁰₋₅₁₀	9860 ± 240	10020⁺⁷⁴⁰₋₆₅₀	10070 ± 270	9920 ± 280	10040 ± 210
T_e (high) Adopted	8470 ± 200	8270 ± 110	8440 ± 140	8530 ± 100	8510 ± 120	8360 ± 140	8480 ± 150

* indicates that a maximum likelihood method was used.

sponds to the median of the Monte Carlo distribution and the errors are represented by the deviations to 84th and 16th percentiles. After this procedure, all diagnostics (either T_e or n_e), will have a result for each cross-comparison.

For the nebular components on each cut, we define the representative n_e as the weighted mean⁴ in each cross-comparison with all the temperature indicators. In the case of high-velocity components, the treatment is more complex since all the density diagnostics based on CELs reveal considerably higher densities than in the nebular components, reaching a zone of expected densities that far exceed the critical density of the atomic levels in some cases as it is shown in Table 6. At densities of $10^4 - 10^6$ cm⁻³, diagnostics based on [Fe III] lines are more reliable than other classic diagnoses such as [O II] $\lambda 3726/\lambda 3729$ or [S II] $\lambda 6731/\lambda 6716$. In addition, dust destruction processes release gaseous Fe in the shock front that should favor the conditions of the head of the gas flow over other zones that travel at the same velocity. In high-velocity components, the density determined with [Fe III] lines in a maximum-likelihood method is adopted. This procedure and its interpretation is described in detail in § 4.2.

Finally, using the adopted representative n_e , we calculate T_e with the available diagnostics using the PyNeb's *getTemDen* task. Within the scheme of two ionization zones, we define $T_e(\text{high})$ as the weighted mean T_e obtained from [Ar III] $\lambda 5192/\lambda 7136+7751$, [O III] $\lambda 4363/\lambda 4959+5007$ and [S III] $\lambda 6312/\lambda 9069+9531$ line ratios. Similarly, we define $T_e(\text{low})$ based on the resulting T_e obtained from [S II] $\lambda\lambda 4069+76/\lambda\lambda 6716+31$, [N II] $\lambda 5755/\lambda 6584$ and [O II] $\lambda\lambda 3726+29/\lambda\lambda 7319+20+30+31$ line ratios.

It is remarkable that in the nebular component of all cuts the observed [S III] $\lambda 9531/\lambda 9069$ line intensity ratio does not agree with the theoretical value. This is owing to strong telluric absorptions that affect the [S III] $\lambda 9069$ line. These telluric absorptions do not affect the blueshifted lines of the high velocity components.

⁴ The weights were defined as the inverse of the square of the error associated to each density diagnostic.

After an inspection in the 2D spectra of the calibration star and in the science object, we concluded that [S III] $\lambda 9531$ is not affected by telluric absorptions or emissions at the heliocentric motion at which the observations were taken. In the nebular component of all cuts, we used the theoretical ratio $I([S \text{ III}] 9531)/I([S \text{ III}] 9069) = 2.47$ obtained from the atomic data given in Table 4 to estimate $T([S \text{ III}])$.

Plasma diagnostic plots shown in Fig. A1, indicate that the resulting values of each diagnostic are consistent with each other. The numerical values in each case are presented in Table 7.

4.2 Physical conditions based on [Fe III] lines.

As it was mentioned in § 4, density diagnostics based on different line intensity ratios of [Fe III] apparently give discordant results. This is mainly due to the ambivalence in the density dependence of some observed intensity ratios and/or due to high dependence on T_e as well as on n_e . These two scenarios are exemplified in Fig. 5 for [Fe III] $\lambda 4881/\lambda 4658$ and $\lambda 5271/\lambda 4658$ line ratios. For the expected densities in the different components observed in this work (n_e between $\sim 10^3$ cm⁻³ and $\sim 10^5$ cm⁻³), these diagnostics are not very enlightening on their own. On the other hand, [Fe III] $\lambda 4658/\lambda 4702$ is the most reliable diagnostic in our case. However, although there is no ambivalence at the expected densities, the predicted value for the [Fe III] $\lambda 4658/\lambda 4702$ intensity ratio varies little in a relatively wide range of densities. As a consequence, the deduced density from [Fe III] $\lambda 4658/\lambda 4702$ inherently will have large uncertainties, even with relatively low errors in the line fluxes.

We consider that the best way to determine the physical conditions based on the observed intensity ratios of [Fe III] lines is with a maximum-likelihood process. This method is based on a χ^2 minimization by testing a wide range of parameters. χ^2 is defined in Eq. (2), as the sum of the quadratic differences between the abundance of ion X^i (in this case Fe²⁺) determined with each emission

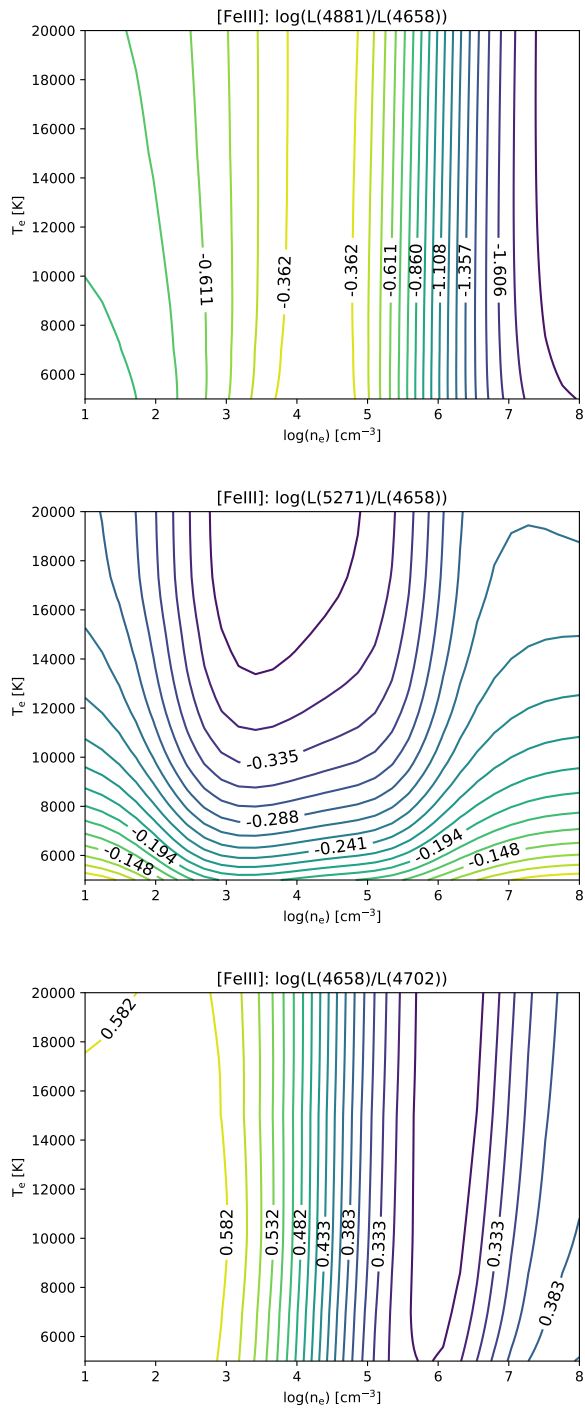


Figure 5. Predicted dependence of the [Fe III] $\lambda 4881/\lambda 4658$, $\lambda 5271/\lambda 4658$ and $\lambda 4658/\lambda 4702$ line intensity ratios with physical conditions using the data of Table 4.

line included in the procedure and the weighted average defined in Eq. (3).

$$\chi^2 = \sum_{\lambda} \frac{\left(n \left(\frac{X^i}{H^+} \right)_{\lambda} - \overline{n \left(\frac{X^i}{H^+} \right)} \right)^2}{\Delta n \left(\frac{X^i}{H^+} \right)_{\lambda}^2}, \quad (2)$$

$$\frac{n \left(\frac{X^i}{H^+} \right)}{\sum_{\lambda} \left(\frac{X^i}{H^+} \right)_{\lambda}} = \frac{\sum_{\lambda} \left(n \left(\frac{X^i}{H^+} \right)_{\lambda} / \Delta n \left(\frac{X^i}{H^+} \right)_{\lambda}^2 \right)}{\sum_{\lambda} \left(1 / \Delta n \left(\frac{X^i}{H^+} \right)_{\lambda}^2 \right)}. \quad (3)$$

As solution, this self-consistent procedure gives the physical parameters that minimize χ^2 with an associated uncertainty based on the resulting values within $\chi^2 - \chi^2_{\min} \leq 1$. This method requires a strict control on the variables that affect the line fluxes, otherwise a spurious contribution appears, and can change the resulting parameters that minimize χ^2 . For example, undetected blends in the studied lines can result in an incorrect density and/or temperature determination.

We have considered several aspects to choose the set of [Fe III] lines that should be included in the maximum-likelihood process. First, we discard lines with evident line blending or contamination by telluric emission or ghosts. To test unnoticed line blends or inaccuracies in flux estimations, we use ratios of observed lines that should depend only on transition probabilities and not on physical conditions. The results are shown in Table 8. As it can be seen, there is a good agreement between the theoretical and observed values in the cases of [Fe III] $\lambda 4778/\lambda 4734$, $\lambda 4702/\lambda 4770$ and $\lambda 4658/\lambda 4755$ line ratios. Deviations between the theoretical and the observed values in the cases of [Fe III] $\lambda 4667/\lambda 4734$, $\lambda 4778/\lambda 4667$, $\lambda 4607/\lambda 4702$ and $\lambda 4607/\lambda 4770$ line ratios are explained by the contamination of [Fe III] $\lambda 4667$ by a ghost and by the blend of [Fe III] $\lambda 4607$ with N II $\lambda 4607.15$. The line ratio with the largest deviation is [Fe III] $\lambda 5011/\lambda 4085$. This could be mainly due to the low signal-to-noise ratio of the [Fe III] $\lambda 4085$ line. However, [Fe III] $\lambda 5011$ is located close to [O III] $\lambda 5007$ that present broad wings in its line profile that affects the shape of the continuum close to [Fe III] $\lambda 5011$ and perhaps the measurement of its line flux.

We select the following [Fe III] lines for the maximum-likelihood process: $\lambda 4658.17, 4701.64, 4734.00, 4881.07, 5270.57$ and 5412.06 . This selection includes the brightest [Fe III] lines that are free of blends or telluric emissions and/or absorptions. We exclude fainter lines coming from the same upper level since they should have the same dependence on physical conditions and their incorporation would only increase the noise level of the results. This selection includes lines in a relatively small spectral range and hence, uncertainties in the reddening correction would have a negligible effect. This allows us to restrict the parameter space to electron density and temperature to test χ^2 . Studies on the primordial helium abundance have used similar maximum-likelihood procedures to calculate the He^+ abundance, noting that this procedure can lead to degeneracies in the fitted parameters and χ^2 (see Olive & Skillman 2004; Aver et al. 2011, and references therein). Because of this, it is important to have an overview of the behaviour of χ^2 in the complete parameter space.

In Fig. 6 we present the convergence of χ^2 in the $n_e - T_e$ space for both high-velocity and nebular components of cut 2. As it can be seen, χ^2 falls into a single minimum in each case, corresponding to $T_e = 8500 \pm 1050$ K and $n_e = 11880 \pm 1860 \text{ cm}^{-3}$ in the high-velocity component and $T_e = 8460 \pm 730$ K and $n_e = 9430 \pm 1010 \text{ cm}^{-3}$ in the nebular one. The T_e and n_e values obtained for the rest of cuts using this approach are presented in Table 7. The convergence to the resulting n_e is consistent with the diagnostic based on [Fe III] $\lambda 4658/\lambda 4702$ ratio but with a smaller uncertainty due to the application of the χ^2 maximum-likelihood procedure. It is remarkable that in all cases, [Fe III] lines give n_e values higher than the usual diagnostics based on CELs such as [S II] $\lambda 6731/\lambda 6716$.

Table 8. Comparison of the observed [Fe III] intensity ratios and theoretical ones from Quinet (1996).

Ratio	Cut 1 Nebula	Cut 2		Cut 3		Cut 4 Nebula	Combined cuts	Quinet (1996)
		Shock	Nebula	Shock	Nebula			
4667/4734*	-	0.52 ± 0.04	0.42 ± 0.02	-	0.45 ± 0.03	0.43 ± 0.03	-	0.28
4778/4734	0.51 ± 0.04	0.70 ± 0.06	0.51 ± 0.03	0.34 ± 0.08	0.49 ± 0.03	0.43 ± 0.04	0.51 ± 0.04	0.48
4778/4667*	-	1.35 ± 0.14	1.22 ± 0.06	-	1.09 ± 0.07	1.00 ± 0.09	-	1.74
4607/4702**	0.24 ± 0.01	0.22 ± 0.02	0.24 ± 0.01	0.24 ± 0.05	0.23 ± 0.02	0.24 ± 0.02	0.23 ± 0.02	0.17
4607/4770**	0.72 ± 0.05	0.60 ± 0.06	0.64 ± 0.03	0.52 ± 0.11	0.64 ± 0.06	0.68 ± 0.05	0.64 ± 0.05	0.51
4702/4770	2.96 ± 0.15	2.68 ± 0.16	2.73 ± 0.10	2.22 ± 0.27	2.74 ± 0.19	2.87 ± 0.14	2.72 ± 0.14	2.93
4658/4755	5.50 ± 0.20	5.28 ± 0.24	5.26 ± 0.15	4.70 ± 0.51	5.32 ± 0.24	5.30 ± 0.19	5.31 ± 0.19	5.49
5011/5085	3.19 ± 0.72	2.51 ± 0.93	5.00 ± 1.00	2.96 ± 1.22	3.61 ± 0.46	3.84 ± 0.94	3.66 ± 0.96	5.94

* $\lambda 4667$ affected by ghost.** [Fe III] $\lambda 4607.12$ blended with N II $\lambda 4607.15$.

or [O II] $\lambda 3726/\lambda 3729$. The largest difference is found in the high-velocity components, reaching almost a factor 3 in the high-velocity component of cut 3. In the case of nebular components this is due to the low sensitivity of the used [Fe III] lines at smaller densities than $\sim 10^3$, which gives more weight to the zones of higher density within the line of sight. On the other hand, in high-velocity components, the larger differences suggest the presence of high densities in the range of $10^4 - 10^5 \text{ cm}^{-3}$, where the usual density diagnostics are uncertain, being well above the critical densities as it is shown in Table 6. In addition, the geometry of HH529 flow and dust destruction (see § 10.1) can contribute to that difference. Using the radial velocity estimation, described in § 9.1 and the proper motion of the system, derived in § 10, we estimate a average flow angle of $\sim 62^\circ$ with respect to the sky plane for HH529, partially flowing towards the observer. Therefore, the volume of gas integrated in the high-velocity components should include not only the denser gas of the head of the shock but also the jet beam gas behind. As we will see in § 8.1.4, Fe abundance is higher at the shock components because of dust destruction (Mesa-Delgado et al. 2009; Espíritu et al. 2017), increasing the flux of [Fe III] lines relative to that of other CELs that are not so affected by this process. Therefore, the n_e determinations based on [Fe III] lines will be biased to the higher values of the density at the head of the shock.

Interestingly, the procedure indicates a higher affinity between T_e ([Fe III]) and T_e (high), contrary to what the ionization potential of Fe^{2+} would suggest, closer to N^+ than O^{2+} , representative ions of the low and high ionization zones, respectively. In the case of the nebular component, the fact that the [Fe III] density diagnostics weight more the high-density zones in the line of sight, as we mentioned previously, may condition the results to lower temperatures. On the other hand, in the high-velocity components, this may indicate that on the shock front, where further dust destruction and reincorporation of Fe into the gas phase is expected, the high-ionization gas dominates over the remaining low-ionization one, flowing behind of the shock front. This suggests that the optimal temperature to calculate the Fe^{2+} abundance in the high-velocity components is T_e (high). However, estimates of Fe^{2+} abundances based on both T_e (low) and T_e (high) will be discussed separately in § 8.1.4.

4.3 Physical conditions determined from recombination lines

4.3.1 Physical conditions based on O II recombination lines

To estimate physical conditions based on O II recombination lines, we use the effective recombination coefficients from Storey et al. (2017). These coefficients fully account the dependence on elec-

tron density and temperature of the distribution population among the ground levels of O II. We follow a similar maximum-likelihood procedure as described in §4.2. In this case, we chose the observed lines from multiplet 1 and $\lambda\lambda 4089.29, 4275.55$ from 3d-4f transitions, due to several reasons: (1) Lines from multiplet 1 are the brightest recombination lines of O II and are comparatively less affected by line blending or instrumental reflections as it is illustrated in Fig. 7. (2) The density dependence of intensity ratios of multiplet 1 lines relies on variations in the density population of 3P_J levels and formally reach the equilibrium with the statistical weight of the levels until $n_{\text{crit}} \approx 10^5 \text{ cm}^{-3}$ (Storey et al. 2017). (3) O II $\lambda\lambda 4089.29, 4275.55$ lines corresponding to 3d-4f transitions depend strongly on T_e . Nevertheless, these lines are relatively weak and we expect comparatively larger uncertainties in T_e determinations than using diagnostics based on CELs.

Fig. 8 shows χ^2 -maps in the space of T_e and n_e for the both components of cut 2. As it can be seen, the high velocity component has a temperature degeneracy within the 6000–23000 K range. This is not surprising, due to the fact that multiplet 1 is rather independent of T_e but highly dependent on n_e and the weak line $\lambda 4275.55$ is the only one that can break the degeneracy in this component since O II $\lambda 4089.29$ is blended with a ghost feature (see § 4.3.2). However, it is clear that the density dependence is well limited within a range of 3000–3700 cm^{-3} . Fixing the temperature to the adopted one for the high ionization zone using CELs, we obtain $n_e = 3490 \pm 340 \text{ cm}^{-3}$ for the high velocity component. On the other hand, since we were able to use the O II $\lambda 4089.29$ together with $\lambda 4275.55$ in the nebular component, we have a convergence within a more limited area, although the error ranges remain wide. The physical conditions that minimizes χ^2 in this case are $n_e = 4390 \pm 400 \text{ cm}^{-3}$ and $T_e = 9350 \pm 1090 \text{ K}$.

In Table 7, we can see that the density values obtained from O II lines are similar to those obtained from other diagnostics in the nebular components but somewhat lower in the high velocity ones. This is due to the weak dependence on density of O II lines from multiplet 1 from values $\sim 10^4 \text{ cm}^{-3}$, as it is shown in Fig. 4 from Storey et al. (2017). Therefore, the values obtained by this diagnostic may not be representative of the shock front.

4.3.2 The alleged observation of Si IV $\lambda 4088.86$ line

Several authors used the $I(\text{O II } \lambda 4649.13)/I(\text{O II } \lambda 4089.29)$ ratio to derive T_e based on its theoretical high dependence on T_e and low dependence on n_e (see e. g. García-Rojas & Esteban 2007; Fang & Liu 2013; McNabb et al. 2013; Wesson et al. 2018). The low dependence of this ratio on n_e is because both lines come from the

Figure 6. Distribution of χ^2 in the space of physical conditions derived from [Fe III] lines in the high-velocity component (left) and the nebular one (right) of cut 2.

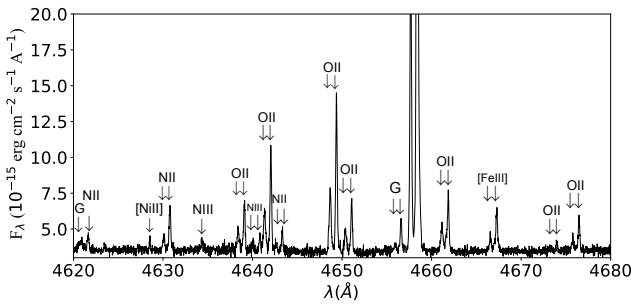
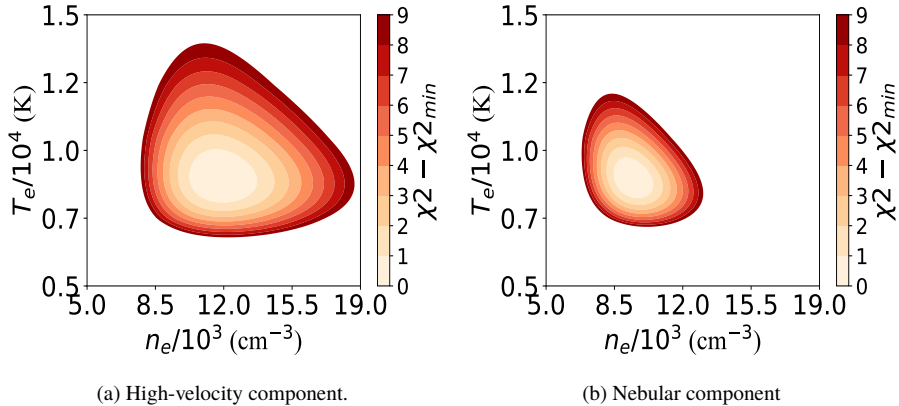


Figure 7. Section of the spectrum of cut 2 around the O II lines of multiplet 1.

highest J of 3P_J levels, depending both on the population of the 3P_2 ground level (Storey et al. 2017). Nevertheless, Peimbert & Peimbert (2013) discourages its use, due (among other reasons) to the possible contamination of O II $\lambda 4089.29$ by the Si IV $\lambda 4088.86$ line, granting lower T_e values. The authors consider that Si IV $\lambda 4088.86$ has been detected in 2 H II regions observed with UVES echelle spectrograph at VLT telescope: the Orion Nebula (Esteban et al. 2004) and 30 Doradus (Peimbert 2003). Although it is a real possibility that a line like Si IV $\lambda 4088.86$ may be detected in an H II region, much of the flux attributed to this line is actually due to an observational artifact of UVES spectrum.

Fig. A2 shows the echelle orders extracted in an UVES blue arm spectrum using dichroic 2 ($\Delta\lambda = 3750 - 4995$). Optical reflections produced by the dichroic 2 in the blue arm can be noted as vertical lines crossing the echelle orders. These artifacts are negligible with the exception of those produced by the most intense lines: [O III] $\lambda 4959$, H β and [O III] $\lambda 5007$ that, despite it does not enter in any complete echelle order in this arm, it is partially observed at the edge of the CCD, as well as its associated high-velocity component. As consequence 4 main sources of "ghost lines" can be immediately noticed, the third of them (from left to right), affects exactly the $\lambda 4089.07$ position in the echelle order number 11 (bottom up) in our observations. Approximately at this wavelength we expect to have the high velocity component of O II $\lambda 4089.29$ in cuts 2 and 3, but it must be free of emission from HH529III in cut 4. Fig. 9 shows the emission around $\lambda 4089.29$ in the spectra of cut 4, a pretty similar image than the Fig. 2 from Peimbert & Peimbert (2013).

In our spectra, the Si IV $\lambda 4088.86$ line, due to its high ion-

ization potential, should be observed at $\lambda 4089.08$, considering the kinematical structure of the nebular component (see § 9.1). This means that in case of being detected, the Si IV $\lambda 4088.86$ line would be indistinguishable from the ghost line at $\lambda 4089.07$. We have measured the intensity of ghost lines coming from the same source than $\lambda 4089.07$ along the echelle orders but excluding those ones which are blended with other nebular lines. Fig. A3 shows the decreasing trend of the intensity of ghost emission with respect to its source from higher to lower orders, as well as a least squares fit to predict ghost emission in order 11, where the emission feature at $\lambda 4089.07$ lies. The predicted ghost emission in $\lambda 4089.07$ is $\frac{F(\lambda)}{F(H\beta)} = 0.007$ while the rms of the noise associated with the continuum in cut 4 around $\lambda 4089.07$ represents a possible contribution of $\frac{F(\text{rms})}{F(H\beta)} = 0.004$. On the other hand, the measured flux of $\lambda 4089.07$ is $\frac{F(\lambda)}{F(H\beta)} = 0.012$. Thus, the emission observed at $\lambda 4089.07$ is consistent with purely ghost emission. This ghost emission affects in a similar way the spectra of the Orion Nebula and 30 Dor analyzed by Esteban et al. (2004) and Peimbert (2003), respectively.

The main drawback of the T_e diagnostic based on the $I(\text{O II } \lambda 4649.13)/I(\text{O II } \lambda 4089.29)$ ratio in H II regions is that $\lambda 4089.29$ is rather weak, providing uncertain T_e values. Therefore, this diagnostic will only be useful when the O II lines are well measured, or when the object shows significant difference between the T_e of the zone where the O II lines are formed and the rest of the nebula (Wesson et al. 2018). Finally, although Si IV lines are expected to be rather faint in normal H II regions, this may not be the case in high-ionization planetary nebulae (PNe) as NGC 3918 (García-Rojas et al. 2015).

4.3.3 Electron temperature from He I recombination line ratios

Following the procedure used by Zhang et al. (2005) for PNe, we have used the $I(\text{He I } \lambda 7281)/I(\text{He I } \lambda 6678)$ ratio for deriving T_e (He I) in our spectra. The use of those particular lines have several advantages. First, $\lambda 7281$ and $\lambda 6678$ are among the brightest He I RLs and their use minimizes observational errors. Second, they are produced in transitions between singlet levels, ensuring that they are free of significant self-absorption effects. We have explored the temperature dependence of other intensity ratios of He I $\lambda 7281/\lambda$ with respect to other relevant singlet lines apart of $\lambda 6678$ as $\lambda\lambda 4388, 4922, 4438, 3614, 3965$ and 5016 using the recombination coeffi-

Figure 8. Distribution of χ^2 in the space of physical conditions derived from O II lines in the high-velocity component (left) and the nebular one (right) of cut 2.

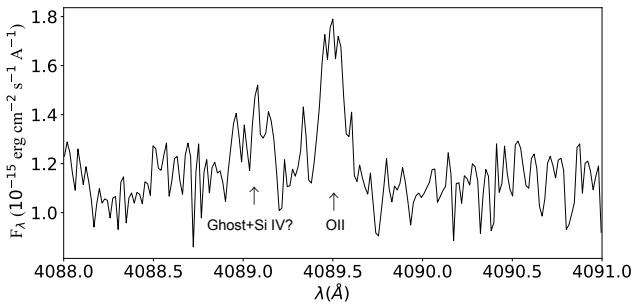
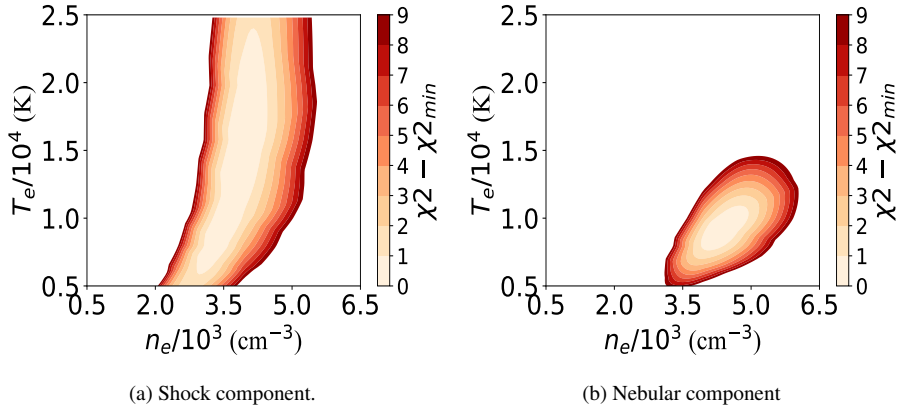


Figure 9. Emission spectrum of cut 4 around $\lambda 4089.29$. This cut does not contain high velocity components.

cients of Porter et al. (2012, 2013). The highest dependence on T_e for the studied ratios is reached with those transitions coming from 5^1D , 4^1D , 3^1D levels to 2^1P (see Fig. A4), the same down level of the transition that produces the He I $\lambda 7281$ line, which comes from the 3^1S level. On the other hand, comparatively, the $I(\text{He I } \lambda 7281)/I(\text{He I } \lambda 6678)$ ratio has the smallest n_e dependence, agreeing with the conclusion by Zhang et al. (2005), despite using different recombination coefficients.

Fig. A5 shows that the T_e dependence of $I(\text{He I } \lambda 7281)/I(\text{He I } \lambda 6678)$ ratio is practically linear in the interval $5000 \text{ K} \leq T_e(\text{K}) \leq 10000 \text{ K}$. The deviation between the determination of $T_e(\text{He I})$ using a linear fit (as in Eq. (4)) and a more complex interpolation of the recombination coefficients of Porter et al. (2012, 2013) is always smaller than 35 K. At $T_e > 10000 \text{ K}$, any linear fit will fail for almost all n_e values except for the lowest ones ($n_e \leq 100 \text{ cm}^{-3}$). In these cases, a more complex treatment is necessary to estimate $T_e(\text{He I})$. The linear fit (slope and intercept) varies significantly in the lower density ranges, and tends to remain almost constant for densities $n_e \geq 10000 \text{ cm}^{-3}$.

$$T_e(\text{He I}) (\text{K}) = \alpha \left[\frac{I(\lambda 7281)}{I(\lambda 6678)} \right] + \beta. \quad (4)$$

In Table A1, we present the slope and intercept values given by Eq. (4) for a density range representative for H II regions and some PNe. In this table we also include average $T_e(\text{He I})$ values obtained with $I(\lambda 7281)/I(\lambda 6678)$, $I(\lambda 7281)/I(\lambda 4922)$ and $I(\lambda 7281)/I(\lambda 4388)$ ratios, all consistent with each other, for all components of all spectra.

4.4 Electron temperature determinations from nebular continuum.

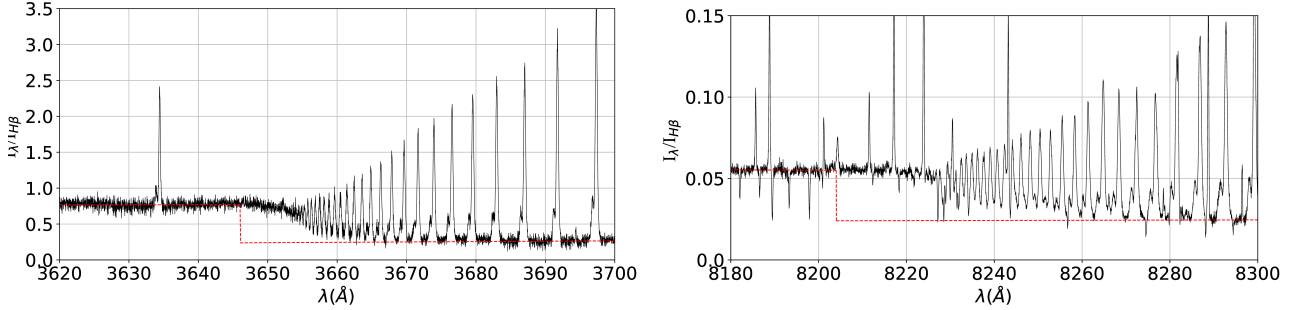
Thanks to the high signal-to-noise ratio of our spectra, we can obtain a reasonable determination of the Balmer and Paschen discontinuities of the nebular continuum in the spectrum resulting from adding all the cuts (see Fig. 10). We have determined the T_e for the nebular continuum using both discontinuities. We used Eq. (5), taken from Liu et al. (2001) for $\text{He}^{2+}/\text{H}^+ = 0$ to estimate $T_e(\text{HI})_{\text{Balmer}}$. This formula is based on theoretical continuum emission of HI, He I and He II calculated by Brown & Mathews (1970) and the theoretical line emission of HI $\lambda 3770.63$ (H11) from Storey & Hummer (1995). Analogously, we used Eq. (6), taken from Fang & Liu (2011) to estimate $T_e(\text{HI})_{\text{Paschen}}$ using the measured Paschen discontinuity and the intensity of HI $\lambda 8862.78$ (P11) line.

$$T_e(\text{HI})_{\text{Balmer}} (\text{K}) = 368 \times \left(1 + 0.259 \frac{\text{He}^+}{\text{H}^+} + 3.409 \frac{\text{He}^{2+}}{\text{H}^+} \right) \left(\frac{\text{BJ}}{\text{H11}} \right)^{-3/2}. \quad (5)$$

$$T_e(\text{HI})_{\text{Paschen}} (\text{K}) = 8.72 \times \left(1 + 0.52 \frac{\text{He}^+}{\text{H}^+} + 4.40 \frac{\text{He}^{2+}}{\text{H}^+} \right) \left(\frac{\text{PJ}}{\text{P11}} \right)^{-1.77}. \quad (6)$$

The estimation of the temperature requires a precise fit to the continuum emission at both sides of 3646 Å and 8204 Å, the approximate wavelengths of the Balmer and Paschen discontinuities, respectively, since both estimations are very sensitive to changes in the jump value. In all individual cuts, the noise level of the continuum results into large uncertainties in the estimation of the temperature. For this reason, the best estimate is obtained by using the spectrum resulting from adding all the cuts. However, this has the drawback of mixing the emission contributions of the nebular and the shock components in the continuum. As Bohigas (2015) remarks, the total $T_e(\text{HI})$ would be the weighted average of the individual values of the mixed nebular components, in this case, the high velocity and nebular components, where the weights would be the H^+ mass of each component.

Fig. 10 shows the discontinuities and the fitted Balmer and Paschen continua in the normalized and reddening corrected spectrum. The best fit is achieved with $\text{BJ}/I_{H\beta} = 0.532 \pm 0.036$ and $\text{PJ}/I_{H\beta} = 0.031 \pm 0.002$.

Figure 10. Balmer and Paschen discontinuities of the resulting spectrum after adding all cuts.

5 CHEMICAL ABUNDANCES

5.1 Ionic abundances from CELs

Using the transition probabilities and collisional strengths from Table 4, we estimate the ionic abundances based on the observed CELs using the PyNeb routines. Abundances for O⁺, N⁺, S⁺, Ni²⁺ and Cl⁺ were derived using the n_e and $T_e(\text{low})$ adopted for each component of each cut, while abundances for O²⁺, Ne²⁺, Cl³⁺, Fe³⁺, Ar²⁺ and Ar³⁺ rely on the adopted $T_e(\text{high})$. S²⁺ and Cl²⁺ abundances were derived using $T_e(\text{[S III]})$. In the case of Fe²⁺, estimations of its abundance are presented using both $T_e(\text{high})$ and $T_e(\text{low})$ (see Table A2 and Table A3), considering that in § 4.2 it was shown that the lines of [Fe III] converged at a temperature close to $T_e(\text{high})$. This will be analyzed in § 8, showing that considering any of both temperatures, there is an increase in the total abundance of Fe in the high-velocity components with respect to the nebular gas. General results are presented in Table 11.

5.1.1 Cl²⁺ and Cl abundances

Domínguez-Guzmán et al. (2019) have proposed the use of $T_e(\text{[N II]})$ to determine the Cl²⁺ abundance in a sample of 37 Galactic and extragalactic H II regions, including the Orion Nebula (they use the data by Esteban et al. 2004). They argue in favour of the use of such T_e indicator because it reduces the dispersion of the Cl/O ratio of their sample and remove trends in the Cl/O versus O/H relation. However, in a detailed study of each specific object, the optimal temperature to adopt can differ from what statistically would be the best choice. Assuming a two ionization zones approximation with two different T_e depending on the IP of the ions, it is not obvious which T_e is the most appropriate for an ion as Cl²⁺ whose threshold of existence (23.81–39.61 eV) is rather in between the N⁺ (14.53–29.6 eV) and O²⁺ (35.12–54.94 eV), whose representative T_e are normally assumed as the ones of the low and high ionization zone, respectively. In this sense, we expect that a T_e representative of an intermediate ionization zone as $T_e(\text{[S III]})$ should be more appropriate for Cl²⁺. However, in general, the measurement of $T_e(\text{[S III]})$ has the inconvenient that [S III] $\lambda\lambda 9069, 9531$ lines fall in a spectral region that is commonly affected by telluric absorption bands (Noll et al. 2012). In § 4 we commented that the [S III] $\lambda 9069$ line is affected by telluric absorption while [S III] $\lambda 9531$ is not. Berg et al. (2020), using observations of H II regions in four spiral galaxies, explore T_e relationships finding that the linear correlation between $T_e(\text{[N II]})$ and $T_e(\text{[S III]})$ shows a larger dispersion as ionization degree increases. For objects with the higher ionization degree, a linear correlation between $T_e(\text{[O III]})$ and $T_e(\text{[S III]})$ seems to be more appropriate. In this work, we are able to calculate the total Cl

abundance from our spectra because we measure CELs of all the ionization species of Cl that can be present in the Orion Nebula. We test the resulting Cl abundance taken three different temperatures: $T_e(\text{low})$, $T_e(\text{[S III]})$ and $T_e(\text{high})$. As it was said in §4.1, $T_e(\text{low})$ and $T_e(\text{high})$ were defined as the weighted average of the T_e values given by different diagnostics, but their values are actually very similar to $T_e(\text{[O III]})$ and $T_e(\text{[N II]})$, respectively. In Table A4, we present the Cl²⁺ and Cl abundances as well as their corresponding Cl/O ratios using the three aforementioned temperatures.

Using $T_e(\text{low})$, the Cl/O ratio in HH529II is smaller around 0.1 dex with respect to the value found in HH529III and in the nebular components, suggesting an underestimation of Cl, although it is within the limit of the uncertainties. When using $T_e(\text{[S III]})$ or $T_e(\text{high})$ to estimate the Cl²⁺/H abundance, this underestimation disappear. We obtain a mean Cl/O ratio of -3.63 ± 0.03 , -3.42 ± 0.03 and -3.50 ± 0.03 when adopting $T_e(\text{low})$, $T_e(\text{high})$ or $T_e(\text{[S III]})$ to calculate the Cl²⁺ abundance, respectively. The Cl/O ratio obtained using $T_e(\text{[S III]})$ is the one closest to the solar value of -3.50 ± 0.09 recommended by Lodders (2019). Therefore, we adopt $T_e(\text{[S III]})$ to estimate Cl²⁺/H.

5.1.2 Ni²⁺ abundance

The first estimation of the Ni abundance in an H II region was made by Osterbrock et al. (1992) for the Orion Nebula. They used estimates of the atomic data of Ni ions, considering [Ni II] and [Ni III] lines. Since then, the number of Ni abundance determinations in ionized nebulae is still very limited, both for PNe (Zhang & Liu 2006; García-Rojas et al. 2013; Delgado-Inglada et al. 2016) and H II regions (Mesa-Delgado et al. 2009; Delgado-Inglada et al. 2016). There is a considerable amount of [Ni II] and [Ni III] lines in our spectra. However, [Ni II] lines are affected by fluorescence (Lucy 1995) and their use to calculate the abundance of Ni⁺ is restricted to some particular cases as low-excitation nebulae (Zhang & Liu 2006). On the other hand, [Ni III] lines are, in principle, not affected by fluorescence effects and can be used to derive Ni²⁺ abundances. From all the detected [Ni III] lines, we chose [Ni III] $\lambda\lambda 6000, 6534, 6682, 6797, 6946$ and 7890 because they are not either affected by blends or telluric absorption.

As we commented in §4, all tested diagnostics based on [Ni III] lines do not provide reliable values of physical conditions, indicating inaccuracies between the observed lines and the theoretical predictions. Delgado-Inglada et al. (2016) studied the Fe/Ni ratio in eight PNe and three H II regions, including the Orion Nebula. They used different datasets for these last objects, including the high resolution ones from Esteban et al. (2004) and Mesa-Delgado et al. (2009) (which includes HH202), and some of their own ob-

servations covering approximately the same area as the Position 1 of [Esteban et al. \(1998\)](#) and the brightest part of the Orion Bar. We have compared our data with some observed flux ratios compiled by [Delgado-Inglada et al. \(2016\)](#) looking for possible undetected line blends or observational inaccuracies. For convenience, we have compared the predicted and observed flux ratios of [Ni III] $\lambda\lambda 6000, 6534$ and 6946 lines that arise from the same atomic level and their intensity ratios should be constant. In Table 9, we compare the observed flux ratios and the predicted ones using the atomic data of Ni²⁺ by [Bautista \(2001\)](#).

As Table 9 shows, the [Ni III] $\lambda 6534/\lambda 6000$ and $\lambda 6946/\lambda 6000$ intensity ratios are rather inconsistent with the predicted ones. This seems to be due to an inconsistency between predicted and measured flux in [Ni III] $\lambda 6000$ line. However, we discard the presence of observational features or sky emission affecting this line. In addition, there are no candidates of unusual lines in the literature or in the Atomic Line List v2.05b21 with a wavelength difference below to 0.15 \AA (a conservative limit for an appropriate deblending of Gaussian profiles at our spectral resolution) that may be blended with [Ni III] $\lambda 6000$ line.

An apparently discordant behaviour is also noticeable in the kinematic structure of [Ni III] lines. As we can see in Table 10, there is a considerably difference between the observed heliocentric velocity in each line contrary to what we would expect for lines that are emitted in the same volume or component of the nebula (see § 9.1). These differences are larger than the expected ones considering the uncertainties of the theoretical wavelengths given by the Atomic Line List v2.05b21: $\lambda\lambda 6000.16 \pm 0.05, 6533.76 \pm 0.06, 6682.16 \pm 0.06, 6797.05 \pm 0.07, 6946.39 \pm 0.07$ and 7889.93 ± 0.09 , which are taken from the work of [Sugar & Corliss \(1985\)](#).

The problems discussed above translate in an inconsistent pattern of Ni²⁺ abundances in all cuts and components. Table A5 shows that Ni²⁺/H⁺ ratios vary significantly from one line to another, with differences up to 0.8 dex. This problem would also affect the results obtained by [Esteban et al. \(2004\)](#), [Mesa-Delgado et al. \(2009\)](#) or [Delgado-Inglada et al. \(2016\)](#). We consider that the nowadays available energy levels and atomic data of Ni²⁺ are not accurate enough to derive confident values of its ionic abundances. Therefore, our Ni²⁺ abundances must be taken with care, since they include unknown uncertainties.

5.2 Ionic abundances from RLs

5.2.1 He⁺ abundance

To estimate the He⁺ abundance, we use the flux of some of the most intense He I lines: $\lambda\lambda 3188, 3614, 3889, 3965, 4026, 4388, 4438, 4471, 4713, 4922, 5016, 5876, 6678, 7065, 7281$. He I $\lambda\lambda 4121, 5048$ lines were discarded because they are contaminated by ghost lines (see § 4.3.2). The 15 selected lines correspond to both singlet and triplet configurations, as it is shown in Fig. A4. The fluxes of triplet lines are affected by the meta-stability of the 2^3S level. The comparatively much longer lifetime of 2^3S , promotes re-excitations of bounded electrons by self-absorption of line photons, altering the flux ratios predicted by recombination theory for some He I lines. For example, self-absorption of He I $\lambda 3188$ photons can increase the flux of He I $\lambda 3889, 5876$ and 7065 lines at the expense of He I $\lambda 3188$, which flux decreases accordingly. On the other hand, self-absorption of the He I $\lambda 3889$ line is also important and increase of the flux of He I $\lambda 7065$ at the expense of He I $\lambda 3889$. The effects of self-absorption are stronger as optical depth of the triplet lines related to the 2^3S level increases. However, the sum of the fluxes

of He I $\lambda\lambda 3188, 3889, 4713, 5876$, and 7065 lines should remain independent of the optical depth (parameterized by τ_{3889} or τ_{3188} , [Porter et al. 2007](#)).

In Table 12, we show the He⁺ abundances determined using the fluxes of He I $\lambda\lambda 3188, 3889, 4713, 5876$, and 7065 lines and the values of n_e and $T_e(\text{He I})$ corresponding to each component of each cut. In the same table, we also include the He⁺ abundance obtained from the sum of the fluxes of all the individual lines of the table and re-distributing it assuming $\tau_{3188} = \tau_{3889} = 0$. In Table 13 we show the He⁺ abundances determined from singlet lines and those triplet ones that are expected to be less affected by self-absorption (see Table 2 from [Benjamin et al. 2002](#)). Tables 12 and 13 show a good agreement between the average values of He⁺/H⁺ ratios included in Table 13 (the last row) and those obtained summing the fluxes of lines included in Table 12. This last table also shows that the self-absorption effects are less important in the high velocity gas than in the nebular one. This is noticeable in the larger dispersion of the abundances obtained with each individual line without considering the effects of self-absorption and that obtained redistributing the fluxes as expected at $\tau = 0$ in the nebular components. As it is discussed in [Osterbrock & Ferland \(2006\)](#), see their figure 4.5) if the nebula has ionized zones with different velocities, the self-absorption effects can be reduced due to the Doppler shift between the emitting and absorbing zones. For example, the effect of the self-absorption in the intense He I $\lambda 5876$ line is remarkable in the nebular component, giving He⁺ abundances about 0.05 dex higher than the sum value. In this sense, the common procedure of using a flux-weighted average of He I $\lambda 5876$ and other bright optical He I lines (as $\lambda\lambda 4471$ and 6678) for obtaining the mean He⁺ abundance would provide rather an upper limit of it.

Another interesting fact that can be noted in Table 13 is that the He⁺ abundance determined from the He I $\lambda 5016$ line is lower than that obtained from other lines in the high velocity components. An abnormally low flux of this line was noted by [Esteban et al. \(2004\)](#), and this was attributed to self-absorption effects in the singlet configuration of He I. [Porter et al. \(2007\)](#) discussed this, proposing that the most likely explanation is a deviation from case B of the He I $\lambda\lambda 537.0$ and 522.0 lines, that go to the ground level, partially escaping before being reabsorbed. This is probably the case in the high velocity components where any kind of self-absorption of photons from the "static" nebular gas should be reduced.

5.2.2 O²⁺ abundance

We calculate the O²⁺ abundance using the RLs presented in Table 14, using the n_e determined from O II lines for the nebular components and the adopted density based on [Fe III] lines in the high velocity components, following the results described in § 4.3.1. In all components, the $T_e(\text{high})$ was adopted. The abundance calculation (as well as the n_e estimation) is based on the recombination coefficients calculated by [Storey et al. \(2017\)](#). This coefficients consider the distribution of population among the O²⁺ levels with some improvements over similar estimates from [Bastin & Storey \(2006\)](#). Previous works on recombination coefficients of O II as [Storey \(1994\)](#) assumed that the O²⁺ levels are populated according to their statistical weight, which is not suitable for densities below the critical one.

In Table 14, we present the weighted average abundance for each multiplet. In the last row of Table 14 we give the final O²⁺ abundance obtained averaging the values obtained for multiplets 1, 2, 10, 20 and $3d - 4f$ transitions. These multiplets and transitions give consistent values and were also considered by [Esteban et al. \(2004\)](#)

Table 9. Comparison of the observed [Ni III] intensity ratios and theoretical ones from Bautista (2001).

Ratio	Mesa-Delgado et al. (2009) Esteban et al. (2004)	Shock HH202	Delgado-Ingla et al. (2016) Orion Bar	This work Nebular	This work High velocity Cut 2	Predicted
6534/6000	2.09 ± 0.94	1.58 ± 0.38	1.46 ± 0.40	1.54 ± 0.39	3.35 ± 1.40	2.19
6946/6000	-	0.28 ± 0.09	-	0.31 ± 0.11	0.82 ± 0.52	0.39

Table 10. Heliocentric velocities of [Ni III] lines (in km s⁻¹) for each component and cut. Typical error is between 1–2 km s⁻¹

λ (Å)	Cut 1		Cut 2		Cut 3		Cut 4	
	Nebula	High-Velocity	Nebula	High-Velocity	Nebula	High-Velocity	Nebula	High-Velocity
6000	21.39	-26.08	19.39	-	20.39	18.89		
6534	8.77	-32.52	7.86	-26.10	6.94	6.48		
6682	3.36	-	6.50	-	3.81	-		
6797	4.75	-42.00	2.55	-	1.22	1.66		
6946	6.97	-37.49	6.10	-32.31	4.38	6.10		
7890	20.32	-24.52	20.32	-19.20	19.18	19.56		

for determining their mean values. However, we decided to consider only the abundance obtained from multiplet 1 as representative of the O²⁺ abundance. This is because, although it gives values consistent with the average of the other aforementioned multiplets and transitions, the inclusion of the results for several multiplets with fainter lines increases the formal uncertainties of the final mean O²⁺ abundance.

5.2.3 Determination of the abundance of other heavy elements based on RLs.

Due to the high quality of our deep spectra, we were able to determine abundances of other heavy element ions such as O⁺, C²⁺ and Ne²⁺ based on the fluxes of RLs and the recombination coefficients presented in Table 5.

O⁺ abundances were obtained from the lines of multiplet 1 of O I $\lambda\lambda$ 7771.94, 7774.17 and 7775.39 together with the adopted density and temperature of the low ionization zone for each component of each cut. Due to the high spectral resolution of our data, these O I lines are not blended with telluric emission features as it is shown in Fig. 11. We do not detect the lines of multiplet 1 of O I in the high velocity components. In these cases, we have estimated upper limits of their intensity and corresponding abundances considering an hypothetical line with a flux of 3σ of the rms of the adjacent continuum. The resulting O⁺ abundances and the estimated upper limits for the shock components are shown in Table 15.

For C²⁺ and Ne²⁺, we adopt the temperature of the high ionization zone for each component of each cut. C II RLs from different transitions were considered to derive C²⁺ abundances, as it is shown in Table 15. Multiplet 6 of C II has two lines at 4267.00 and 4267.18 Å resolved at our spectral resolution, as shown in Fig. 12. In general, lines from all multiplets of C II considered give consistent values of C²⁺ abundances. RLs from multiplet 1 of Ne II were used to calculate the Ne²⁺ abundance. Although they are rather faint lines (see Fig. 13), the Ne²⁺ abundances derived from Ne II $\lambda\lambda$ 3694.21 and 3766.26 lines for each component of cut 2 are consistent with each other. In addition, the Ne²⁺ abundance we derive for the nebular component in cuts 2 and 3 is in good agreement with that obtained by Esteban et al. (2004) (see their Table 11).

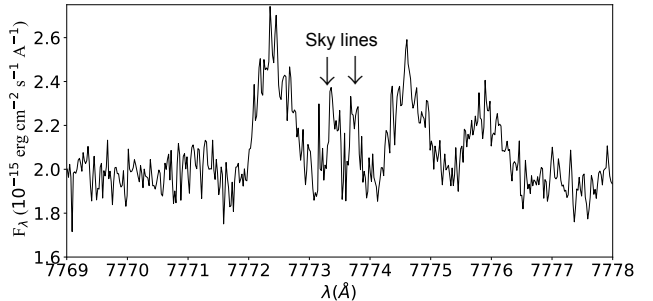


Figure 11. Lines of multiplet 1 of O I ($3s^5S^0$ - $3p^5P$) from the spectrum of Cut 2. Due to high spectral resolution, these lines are free of blending with sky emission features.

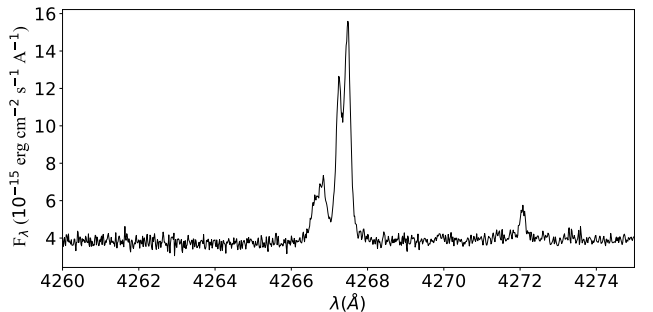


Figure 12. Lines of multiplet 6 of C II ($3d^2D$ - $4f^2F^0$) from the spectrum of Cut 2.

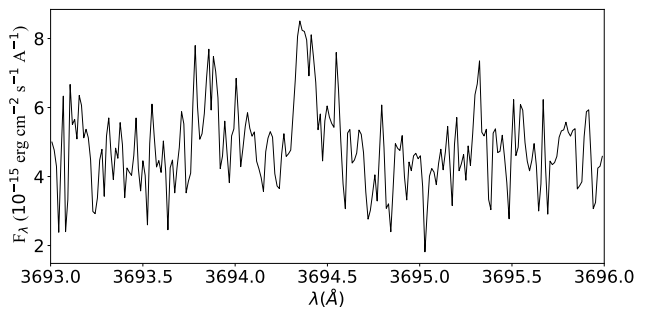


Figure 13. Lines of multiplet 1 of Ne II ($3s^4P$ - $3p^4P^0$) from the spectrum of Cut 2.

6 TEMPERATURE FLUCTUATIONS

Following the procedure described by Peimbert (1967), we define the average temperature as it is shown in Eq. (7) and the mean square temperature fluctuation as in Eq. (8).

$$T_0 = \frac{\int T_e n_e n_i dV}{\int n_e n_i dV}, \quad (7)$$

Table 11. Chemical abundances based on CEL's without considering the temperature fluctuations scenario ($t^2 = 0$).

Ion	Cut 1		Cut 2		Cut 3		Cut 4	Combined cuts
	Nebula	Shock	Nebula	Shock	Nebula	Nebula	Nebula	
O ⁺	7.88 ± 0.04	7.36 ^{+0.12} _{-0.09}	7.83 ^{+0.06} _{-0.05}	7.83 ^{+0.18} _{-0.12}	7.76 ^{+0.07} _{-0.06}	7.81 ^{+0.07} _{-0.06}	7.75 ± 0.05	
O ²⁺	8.32 ± 0.03	8.54 ^{+0.03} _{-0.02}	8.35 ± 0.03	8.51 ± 0.02	8.35 ^{+0.03} _{-0.02}	8.36 ± 0.03	8.37 ± 0.03	
N ⁺	7.00 ± 0.02	6.19 ^{+0.06} _{-0.05}	6.99 ± 0.03	6.61 ^{+0.10} _{-0.07}	6.91 ^{+0.04} _{-0.03}	6.98 ^{+0.04} _{-0.03}	6.89 ± 0.03	
Ne ²⁺	7.67 ± 0.04	7.91 ± 0.03	7.70 ^{+0.04} _{-0.03}	7.82 ^{+0.03} _{-0.02}	7.73 ± 0.03	7.75 ^{+0.04} _{-0.03}	7.73 ^{+0.04} _{-0.03}	
S ⁺	5.58 ± 0.05	4.88 ^{+0.08} _{-0.07}	5.57 ^{+0.05} _{-0.04}	5.41 ^{+0.11} _{-0.09}	5.53 ^{+0.06} _{-0.05}	5.59 ± 0.05	5.49 ± 0.05	
S ²⁺	6.79 ± 0.04	6.92 ^{+0.05} _{-0.04}	6.85 ^{+0.09} _{-0.07}	6.91 ± 0.05	6.86 ^{+0.05} _{-0.04}	6.82 ^{+0.05} _{-0.04}	6.85 ± 0.04	
Cl ⁺	3.72 ± 0.04	2.95 ^{+0.14} _{-0.13}	3.71 ± 0.04	<3.34	3.68 ± 0.04	3.75 ± 0.04	3.63 ± 0.04	
Cl ²⁺	4.88 ^{+0.06} _{-0.05}	5.01 ^{+0.06} _{-0.05}	4.93 ^{+0.06} _{-0.05}	5.09 ^{+0.08} _{-0.06}	4.96 ^{+0.06} _{-0.05}	4.95 ^{+0.06} _{-0.05}	4.94 ^{+0.05} _{-0.04}	
Cl ³⁺	3.28 ± 0.06	3.60 ± 0.05	3.28 ^{+0.04} _{-0.03}	3.41 ± 0.11	3.33 ± 0.04	3.45 ± 0.04	3.38 ± 0.05	
Ar ²⁺	6.31 ± 0.03	6.39 ± 0.02	6.31 ± 0.03	6.37 ± 0.03	6.33 ± 0.02	6.29 ± 0.03	6.32 ± 0.03	
Ar ³⁺	4.39 ^{+0.06} _{-0.05}	4.67 ^{+0.04} _{-0.03}	4.47 ^{+0.04} _{-0.03}	4.52 ± 0.07	4.50 ± 0.04	4.61 ^{+0.04} _{-0.03}	4.52 ^{+0.05} _{-0.04}	
*Fe ²⁺	5.77 ± 0.02	5.94 ± 0.05	5.82 ± 0.02	5.78 ± 0.05	5.78 ± 0.02	5.76 ± 0.03	5.80 ± 0.02	
**Fe ²⁺	5.52 ± 0.03	5.62 ± 0.07	5.57 ± 0.02	5.54 ± 0.06	5.52 ± 0.04	5.48 ± 0.03	5.53 ± 0.04	
Fe ³⁺	5.68 ^{+0.13} _{-0.11}	6.25 ^{+0.10} _{-0.09}	5.70 ^{+0.09} _{-0.08}	<6.58	5.73 ^{+0.11} _{-0.10}	5.73 ^{+0.13} _{-0.12}	5.75 ^{+0.11} _{-0.10}	
Ni ²⁺	4.37 ± 0.14	4.50 ± 0.08	4.33 ± 0.17	4.39 ^{+0.12} _{-0.10}	4.32 ± 0.16	4.36 ± 0.12	4.38 ± 0.10	

* indicates that T_e (high) was used.** indicates that T_e (low) was used.**Table 12.** He⁺ abundances for He I triplet lines most affected by self-absorption.

λ_0 (Å)	Cut 1		Cut 2		Cut 3		Cut 4	Combined Cuts
	Nebula	Shock	Nebula	Shock	Low Velocity	Shock + Nebula	Nebula	
3188	10.67 ± 0.02	10.92 ± 0.02	10.63 ± 0.02	10.97 ± 0.05	10.62 ± 0.02	10.68 ± 0.02	10.71 ± 0.02	
3889	10.60 ± 0.02	10.93 ± 0.02	10.52 ± 0.02	10.75 ± 0.02	10.42 ± 0.02	10.55 ± 0.02	10.61 ± 0.02	
4713	11.01 ± 0.03	11.10 ± 0.03	11.04 ± 0.03	11.02 ^{+0.03} _{-0.04}	11.07 ± 0.02	11.11 ± 0.02	11.07 ± 0.02	
5876	10.96 ± 0.01	10.95 ± 0.01	10.97 ± 0.01	10.92 ± 0.01	10.98 ± 0.01	10.96 ± 0.01	10.97 ± 0.01	
7065	11.34 ± 0.04	11.22 ^{+0.05} _{-0.04}	11.35 ± 0.04	11.18 ± 0.06	11.34 ± 0.04	11.37 ± 0.04	11.34 ± 0.04	
Sum	10.91 ± 0.02	10.97 ± 0.02	10.90 ± 0.02	10.93 ± 0.03	10.89 ± 0.02	10.90 ± 0.02	10.91 ± 0.02	

Table 13. He⁺ abundances for He I singlet lines and the triplet ones less affected by self-absorption.

λ_0 (Å)	Cut 1		Cut 2		Cut 3		Cut 4	Combined Cuts
	Nebula	Shock	Nebula	Shock	Low Velocity	Shock + Nebula	Nebula	
3614	10.93 ± 0.02	10.85 ± 0.04	10.89 ± 0.02	11.09 ± 0.05	10.86 ± 0.02	10.85 ± 0.02	10.89 ± 0.02	
3965	10.88 ± 0.01	10.86 ± 0.02	10.89 ± 0.01	10.93 ± 0.02	10.87 ± 0.01	10.88 ± 0.01	10.89 ± 0.01	
4026	10.89 ± 0.01	10.97 ± 0.01	10.90 ± 0.01	11.00 ± 0.01	10.93 ± 0.01	10.93 ± 0.01	10.93 ± 0.01	
4388	10.90 ± 0.01	10.96 ± 0.01	10.92 ± 0.01	10.97 ± 0.01	10.91 ± 0.01	10.91 ± 0.01	10.92 ± 0.01	
4438	10.95 ± 0.03	10.88 ± 0.04	10.92 ± 0.02	11.08 ± 0.07	10.92 ± 0.02	10.91 ± 0.03	10.94 ± 0.03	
4471	10.87 ± 0.01	10.96 ± 0.01	10.90 ± 0.01	10.93 ± 0.01	10.91 ± 0.01	10.93 ± 0.01	10.91 ± 0.01	
4922	10.90 ± 0.01	10.94 ± 0.01	10.92 ± 0.01	10.94 ± 0.01	10.92 ± 0.01	10.92 ± 0.01	10.92 ± 0.01	
5016	10.87 ± 0.01	10.78 ± 0.02	10.88 ± 0.01	10.84 ± 0.02	10.88 ± 0.01	10.88 ± 0.01	10.87 ± 0.01	
6678	10.90 ± 0.02	10.94 ± 0.02	10.91 ± 0.01	10.93 ± 0.02	10.92 ± 0.02	10.90 ± 0.01	10.92 ± 0.02	
7281	10.90 ± 0.03	10.95 ± 0.03	10.92 ± 0.03	10.93 ± 0.04	10.92 ± 0.03	10.91 ± 0.03	10.93 ± 0.03	
Average	10.89 ± 0.02	10.95 ± 0.03	10.90 ± 0.01	10.95 ± 0.03	10.90 ± 0.02	10.91 ± 0.02	10.91 ± 0.02	

$$t^2 = \frac{\int (T_e - T_0)^2 n_e n_i dV}{T_0 \int n_e n_i dV}. \quad (8)$$

In the case of a temperature derived from the ratio of two quantities that depend on two different powers of temperature, α and β respectively, as the case of the temperature derived from RLS or the ratio between the Balmer or Paschen discontinuities and the

flux of any other H I line, the measured temperature $T_{\alpha/\beta}$ depends on t^2 and T_0 as follows:

$$T_{\alpha/\beta} = T_0 \left(1 - \frac{\alpha + \beta - 1}{2} t^2 \right). \quad (9)$$

On the other hand, two quantities with an individual temperature dependence proportional to $\frac{e^{-kT}}{T^{1/2}}$, as the intensity of CELs,

Table 14: O²⁺ abundances with RLs.^J: Esta tabla debe ir en los apéndices

Mult.	Transition	λ_0	Cut 1	Nebula	Shock	Cut 2	Nebula	Shock	Cut 3	Nebula	Cut 4	Combined Cuts
1	$3s^4P-3p^4D^0$	4638.86	8.547 ± 0.038	8.938 ± 0.027	8.546 ± 0.019	$8.757^{+0.107}_{-0.109}$	8.566 ± 0.067	$8.519^{+0.031}_{-0.032}$	8.632 ± 0.044			
	4641.81	$8.433^{+0.017}_{-0.018}$	$8.809^{+0.017}_{-0.018}$	$8.516^{+0.014}_{-0.013}$	$8.828^{+0.027}_{-0.025}$	$8.502^{+0.014}_{-0.013}$	$8.509^{+0.017}_{-0.018}$	$8.575^{+0.017}_{-0.018}$	$8.575^{+0.017}_{-0.018}$	$8.575^{+0.017}_{-0.018}$	$8.575^{+0.017}_{-0.018}$	
	4649.13	$8.473^{+0.024}_{-0.018}$	8.793 ± 0.014	8.520 ± 0.011	$8.779^{+0.025}_{-0.025}$	8.536 ± 0.015	$8.534^{+0.016}_{-0.018}$	$8.534^{+0.016}_{-0.018}$	$8.534^{+0.016}_{-0.018}$	$8.534^{+0.016}_{-0.018}$	$8.534^{+0.016}_{-0.018}$	
	4650.84	$8.469^{+0.035}_{-0.031}$	8.912 ± 0.027	8.509 ± 0.019	$9.022^{+0.026}_{-0.025}$	8.521 ± 0.023	$8.558^{+0.016}_{-0.018}$	$8.558^{+0.016}_{-0.018}$	8.602 ± 0.028	8.602 ± 0.028	8.602 ± 0.028	
	4661.63	$8.534:$	$9.021^{+0.027}_{-0.026}$	$8.550:$	$8.981^{+0.033}_{-0.031}$	$8.602:$	$8.609:$	$8.609:$	$8.672:$	$8.672:$	$8.672:$	
	4673.73	$8.579^{+0.152}_{-0.149}$	9.041 ± 0.120	$8.478^{+0.070}_{-0.069}$	$8.965:$	$8.790^{+0.062}_{-0.060}$	$8.749^{+0.088}_{-0.087}$	$8.730^{+0.099}_{-0.095}$	$8.730^{+0.099}_{-0.095}$	$8.730^{+0.099}_{-0.095}$	$8.730^{+0.099}_{-0.095}$	
	4676.23	$8.400^{+0.052}_{-0.053}$	$8.748^{+0.047}_{-0.049}$	8.475 ± 0.022	$8.936^{+0.069}_{-0.068}$	8.497 ± 0.026	$8.507^{+0.031}_{-0.031}$	$8.507^{+0.031}_{-0.031}$	$8.543^{+0.034}_{-0.035}$	$8.543^{+0.034}_{-0.035}$	$8.543^{+0.034}_{-0.035}$	
	Average	8.465 ± 0.043	8.830 ± 0.073	8.515 ± 0.018	8.844 ± 0.088	8.517 ± 0.033	8.525 ± 0.026	8.525 ± 0.026	8.584 ± 0.022	8.584 ± 0.022	8.584 ± 0.022	
	2	$3s^4P-3p^4P^0$	4317.14	$8.498^{+0.052}_{-0.054}$	$9.099^{+0.030}_{-0.031}$	8.671 ± 0.022	-	$8.644^{+0.047}_{-0.048}$	8.656 ± 0.035	$8.723:$	$8.723:$	
	4345.56	8.582 ± 0.057	$9.194^{+0.043}_{-0.043}$	8.714 ± 0.026	9.147 ± 0.072	8.659 ± 0.031	8.726 ± 0.030	$8.829^{+0.043}_{-0.044}$	$8.829^{+0.043}_{-0.044}$	$8.829^{+0.043}_{-0.044}$	$8.829^{+0.043}_{-0.044}$	
5	$3s^2P-3p^2D^0$	4349.43	8.659 ± 0.040	$9.015^{+0.022}_{-0.021}$	8.678 ± 0.013	$8.995^{+0.051}_{-0.052}$	$8.650^{+0.021}_{-0.022}$	$8.715^{+0.026}_{-0.025}$	8.767 ± 0.030	8.767 ± 0.030	8.767 ± 0.030	
	4366.89	$8.631^{+0.041}_{-0.040}$	$9.237^{+0.026}_{-0.025}$	8.710 ± 0.022	9.208 ± 0.056	$8.672^{+0.030}_{-0.031}$	$8.724^{+0.030}_{-0.030}$	8.835 ± 0.030	8.835 ± 0.030	8.835 ± 0.030	8.835 ± 0.030	
	Average	8.595 ± 0.062	9.085 ± 0.091	8.686 ± 0.016	9.073 ± 0.097	8.656 ± 0.009	8.706 ± 0.027	8.802 ± 0.033	8.802 ± 0.033	8.802 ± 0.033	8.802 ± 0.033	
	4414.90	$8.807^{+0.053}_{-0.051}$	$8.939^{+0.046}_{-0.047}$	8.754 ± 0.025	$-$	$8.772^{+0.026}_{-0.027}$	$8.689^{+0.053}_{-0.052}$	$8.753^{+0.036}_{-0.035}$	$8.753^{+0.036}_{-0.035}$	$8.753^{+0.036}_{-0.035}$	$8.753^{+0.036}_{-0.035}$	
	4416.97	$8.622^{+0.069}_{-0.063}$	$-$	$8.769^{+0.031}_{-0.030}$	$-$	8.734 ± 0.039	$8.712^{+0.035}_{-0.035}$	$8.680^{+0.036}_{-0.034}$	$8.680^{+0.036}_{-0.034}$	$8.680^{+0.036}_{-0.034}$	$8.680^{+0.036}_{-0.034}$	
	Average	8.710 ± 0.093	$8.939^{+0.046}_{-0.047}$	8.760 ± 0.007	8.759 ± 0.018	8.702 ± 0.011	8.702 ± 0.027	8.712 ± 0.037	8.712 ± 0.037	8.712 ± 0.037	8.712 ± 0.037	
	4069.62	$8.459^{+0.064}_{-0.060}$	$-$	$8.246:$	$-$	$8.352:$	$8.657^{+0.071}_{-0.069}$	$8.299:$	$8.299:$	$8.299:$	$8.299:$	
	4069.88	$8.352^{+0.050}_{-0.049}$	$8.431:$	$8.297:$	$8.348:$	$8.386:$	$8.412^{+0.089}_{-0.089}$	$8.353:$	$8.353:$	$8.353:$	$8.353:$	
	4072.15	8.449 ± 0.026	$8.608^{+0.035}_{-0.034}$	$8.421^{+0.017}_{-0.018}$	$8.761^{+0.066}_{-0.067}$	$8.423^{+0.021}_{-0.022}$	$8.372^{+0.027}_{-0.026}$	8.467 ± 0.026	8.467 ± 0.026	8.467 ± 0.026	8.467 ± 0.026	
	4075.86	$8.436:$	$8.757:$	$-$	$-$	$-$	$8.407^{+0.026}_{-0.029}$	$-$	$-$	$-$	$-$	
10	$3p^4D^0-3d^4F$	4078.84	$8.299^{+0.166}_{-0.159}$	$8.998^{+0.093}_{-0.092}$	$8.503^{+0.040}_{-0.039}$	$8.787:$	$8.787:$	$8.810:$	$8.810:$	$8.810:$	$8.810:$	
	4085.11	8.212 ± 0.150	$9.385:$	8.509 ± 0.035	$9.393:$	8.408 ± 0.065	$8.699^{+0.044}_{-0.043}$	$9.013:$	$9.013:$	$9.013:$	$9.013:$	
	4092.93	$-$	$8.550:$	$8.598^{+0.049}_{-0.047}$	$8.579:$	$8.453^{+0.073}_{-0.071}$	$8.627:$	8.467 ± 0.026	8.467 ± 0.026	8.467 ± 0.026	8.467 ± 0.026	
	Average	8.421 ± 0.048	8.623 ± 0.093	8.450 ± 0.052	$8.761^{+0.066}_{-0.067}$	8.423 ± 0.009	8.413 ± 0.099	$8.433^{+0.045}_{-0.043}$	$8.433^{+0.045}_{-0.043}$	$8.433^{+0.045}_{-0.043}$	$8.433^{+0.045}_{-0.043}$	
	4590.97	$8.414^{+0.062}_{-0.060}$	$8.595^{+0.062}_{-0.061}$	$8.385^{+0.034}_{-0.033}$	$8.674^{+0.073}_{-0.072}$	8.387 ± 0.031	8.415 ± 0.057	$8.433^{+0.045}_{-0.043}$	$8.433^{+0.045}_{-0.043}$	$8.433^{+0.045}_{-0.043}$	$8.433^{+0.045}_{-0.043}$	
	4121.46	$8.791:$	$-$	8.865 ± 0.030	$-$	$8.806:$	$8.862:$	$8.762:$	$8.762:$	$8.762:$	$8.762:$	
	4132.80	$8.451^{+0.069}_{-0.069}$	9.029 ± 0.056	$8.565^{+0.027}_{-0.026}$	$9.031^{+0.150}_{-0.152}$	8.512 ± 0.035	8.579 ± 0.044	$8.651^{+0.053}_{-0.051}$	$8.651^{+0.053}_{-0.051}$	$8.651^{+0.053}_{-0.051}$	$8.651^{+0.053}_{-0.051}$	
	4153.30	$8.622^{+0.038}_{-0.037}$	9.059 ± 0.031	8.605 ± 0.019	$8.983^{+0.023}_{-0.024}$	$8.603^{+0.023}_{-0.024}$	8.623 ± 0.037	8.725 ± 0.032	8.725 ± 0.032	8.725 ± 0.032	8.725 ± 0.032	
	Average	8.565 ± 0.079	9.051 ± 0.013	8.616 ± 0.093	8.988 ± 0.014	8.568 ± 0.044	8.603 ± 0.022	8.701 ± 0.034	8.701 ± 0.034	8.701 ± 0.034	8.701 ± 0.034	
	4104.99	$-$	$8.761:$	$8.363^{+0.126}_{-0.123}$	$-$	$8.458^{+0.102}_{-0.098}$	8.494 ± 0.097	$-$	$-$	$-$	$-$	
15	$3s^2D-3p^2F^0$	4110.79	$8.811:$	$9.584:$	$8.805:$	$9.167:$	$8.766:$	$9.250:$	$9.030:$	$9.030:$	$9.030:$	
	4119.22	$8.563^{+0.049}_{-0.048}$	$8.842^{+0.061}_{-0.059}$	$8.626^{+0.023}_{-0.022}$	$-$	$8.475^{+0.072}_{-0.074}$	$8.722^{+0.036}_{-0.034}$	$8.605^{+0.044}_{-0.043}$	$8.605^{+0.044}_{-0.043}$	$8.605^{+0.044}_{-0.043}$	$8.605^{+0.044}_{-0.043}$	
	Average	$8.563^{+0.048}_{-0.048}$	$8.842^{+0.061}_{-0.059}$	8.626 ± 0.087	$9.167:$	8.469 ± 0.008	8.674 ± 0.087					
	4189.79	$8.344^{+0.047}_{-0.044}$	8.638 ± 0.048	$8.307^{+0.031}_{-0.029}$	$8.810^{+0.122}_{-0.120}$	$8.329^{+0.096}_{-0.096}$	$8.380^{+0.070}_{-0.070}$	$8.074^{+0.092}_{-0.092}$	$8.074^{+0.092}_{-0.092}$	$8.074^{+0.092}_{-0.092}$	$8.074^{+0.092}_{-0.092}$	
	Average	8.200 ± 0.128	8.279 ± 0.323	8.107 ± 0.172	$8.810^{+0.122}_{-0.120}$	8.146 ± 0.119	8.217 ± 0.138					
	4087.15	8.588 ± 0.092	$8.868^{+0.117}_{-0.119}$	$8.644^{+0.065}_{-0.065}$	$9.152^{+0.120}_{-0.120}$	$8.431^{+0.057}_{-0.055}$	$8.526^{+0.096}_{-0.095}$	8.651 ± 0.082	8.651 ± 0.082	8.651 ± 0.082	8.651 ± 0.082	
	4089.29	$8.451^{+0.058}_{-0.057}$	$8.939:$	$8.518^{+0.052}_{-0.052}$	$8.744:$	$8.422^{+0.028}_{-0.027}$	$8.412^{+0.048}_{-0.048}$	8.555 ± 0.036	8.555 ± 0.036	8.555 ± 0.036	8.555 ± 0.036	
	4095.64	$-$	8.824 ± 0.100	$8.499^{+0.054}_{-0.053}$	$9.396:$	$8.545:$	$-$	$-$	$-$	$-$	$-$	
	4097.26	$8.547^{+0.059}_{-0.056}$	$-$	$8.551^{+0.053}_{-0.053}$	$-$	8.577 ± 0.031	$8.592^{+0.039}_{-0.039}$	$8.497^{+0.036}_{-0.036}$	$8.497^{+0.036}_{-0.036}$	$8.497^{+0.036}_{-0.036}$	$8.497^{+0.036}_{-0.036}$	
36	$3p^2F-3d^2G$	4275.55	$8.464^{+0.068}_{-0.067}$	$8.680^{+0.106}_{-0.110}$	$8.520^{+0.047}_{-0.046}$	$-$	$8.475^{+0.053}_{-0.053}$	$8.554^{+0.053}_{-0.053}$	$8.554^{+0.053}_{-0.053}$	$8.554^{+0.053}_{-0.053}$	$8.554^{+0.053}_{-0.053}$	
	$3d^4F-4fG^2[3]^0$	4095.64	$8.464^{+0.068}_{-0.067}$	8.767 ± 0.082	8.534 ± 0.032	$9.152^{+0.094}_{-0.095}$	8.468 ± 0.067	8.507 ± 0.060	8.507 ± 0.060	8.507 ± 0.060	8.507 ± 0.060	
	$3d^4F-4fG^2[$											

Table 15. O⁺, C²⁺ and Ne²⁺ abundances based on RLs.

Mult.	Transition	λ_0	Cut 1 Nebula	Cut 2 Shock	O ⁺ Nebula	Cut 3 Shock	Nebula	Cut 4 Nebula	Combined Cuts
1	$3s^5S^0-3p^5P$	7771.94							
		7774.17	8.344 ± 0.100	<7.91	8.250 ± 0.064	<7.95	8.275 ± 0.073	$8.274^{+0.068}_{-0.069}$	8.187 ± 0.073
		7775.39							
6	$3d^2D-4f^2F^0$	4267.00							
		4267.18	$8.349^{+0.030}_{-0.031}$	8.457 ± 0.017	8.347 ± 0.017	8.557 ± 0.026	8.339 ± 0.013	$8.328^{+0.021}_{-0.022}$	8.371 ± 0.026
		4267.26							
16.04	$4d^2D-6f^2F^0$	6151.27	-	9.054:	8.376:	-	8.441 ± 0.120	-	-
		6151.53							
17.02	$4f^2F^0-5g^2G$	9903.46	$8.326^{+0.043}_{-0.045}$	$8.465^{+0.066}_{-0.063}$	8.363 ± 0.035	$8.622^{+0.138}_{-0.136}$	$8.301^{+0.057}_{-0.056}$	$8.353^{+0.043}_{-0.042}$	$8.377^{+0.057}_{-0.056}$
		9903.89							
17.04	$4f^2F^0-6g^2G$	6461.95	8.354 ± 0.091	8.704:	8.298 ± 0.065	-	8.318 ± 0.060	8.351 ± 0.071	$8.353^{+0.118}_{-0.116}$
		6462.13							
17.06	$4f^2F^0-7g^2G$	5342.38	8.619:	-	$8.449^{+0.059}_{-0.060}$	-	$8.502^{+0.064}_{-0.065}$	-	-
		5342.50							
		Adopted	8.342 ± 0.030	8.458 ± 0.021	8.351 ± 0.025	8.560 ± 0.026	8.340 ± 0.029	8.334 ± 0.022	8.371 ± 0.026
1	$3s^4P-3p^4P^0$	3694.21	-	$8.643^{+0.072}_{-0.073}$	$8.095^{+0.063}_{-0.065}$	-	8.315:	-	-
		3766.26	-	$8.515^{+0.137}_{-0.135}$	$8.034^{+0.089}_{-0.092}$	-	$8.036^{+0.153}_{-0.150}$	-	-
		Adopted	-	8.603 ± 0.057	8.072 ± 0.029	-	8.036 ± 0.150	-	-

will produce a line intensity ratio with a temperature dependence

on $e^{\frac{\Delta E_2 - \Delta E_1}{kT_{\lambda_1/\lambda_2}}}$. We can derive the temperature T_{λ_1/λ_2} :

$$T_{\lambda_1/\lambda_2} = T_0 \left[1 + \left(\frac{\Delta E_1 + \Delta E_2}{kT_0} - 3 \right) \frac{t^2}{2} \right] \quad (10)$$

When α and β in Eq. (9) are negative, the low-temperature zones within the line of sight will have a larger weight on $T_{\alpha/\beta}$, while in the cases where $\frac{\Delta E_1 + \Delta E_2}{kT_0}$ is larger than 3, the contribution of the high-temperature zones will be more important (Peimbert 1967).

On the basis of Eq. (9) and the estimations of the α and β coefficients given by Peimbert & Costero (1969) and Zhang et al. (2005), for the H I and He I temperature, respectively, we have Eq. (11) and Eq. (12).

$$T(\text{H I})_{\text{BJ-PJ}} = T_0 \left(1 - 1.67t^2 \right), \quad (11)$$

$$T(\text{He I})_{7281/6678} = T_0 \left(1 - 1.07t^2 \right). \quad (12)$$

On the other hand, for estimations of temperatures based on intensity ratios of CELs, we have Eq. (13), Eq. (14) and Eq. (15).

$$T([\text{O III}])_{4363/4959+5007} = T_0 \left[1 + \left(\frac{91300}{T_0} - 3 \right) \frac{t^2}{2} \right], \quad (13)$$

$$T([\text{S III}])_{6312/9069+9531} = T_0 \left[1 + \left(\frac{54000}{T_0} - 3 \right) \frac{t^2}{2} \right], \quad (14)$$

$$T([\text{N II}])_{5755/6584} = T_0 \left[1 + \left(\frac{68950}{T_0} - 3 \right) \frac{t^2}{2} \right]. \quad (15)$$

We have applied the combination of Eq. (11) and Eq. (13) using $T(\text{H I})$ and $T([\text{O III}])$ to estimate t^2 (Peimbert 2003; Esteban et al. 2004; García-Rojas et al. 2004, 2005, 2007). Implicitly, this assumes that $t^2(\text{H}^+) \approx t^2(\text{O}^{2+})$ and $T_0(\text{H}^+) \approx T_0(\text{O}^{2+})$. The same procedure has been used with Eq. (14) and Eq. (15) (Peimbert & Costero 1969; Esteban et al. 1998) in order to estimate representative values of t^2 for different ionization zones. In Table (16), we show the t^2 and T_0 values obtained for each combination of the temperature indicators in the spectrum of the combined cuts, the only one where all the different temperature indicators are available. We have to emphasize the excellent agreement between the results obtained by combining $T(\text{H I})$ and the T_e diagnostics based on CELs ratios with what it is obtained using $T(\text{He I})$.

However, the above procedure may not be entirely accurate. From equations (7) and (8), it is clear that the values of t^2 and T_0 depend on the integrated volume. Thus, since each ion X^{i+} will have its own Strömgren sphere, each one will have a representative $t^2(X^{i+})$ and $T_0(X^{i+})$. Considering another ion, Y^{i+} , the assumption $t^2(X^{i+}) \approx t^2(Y^{i+})$ will be only correct if X^{i+} and Y^{i+} occupy the same nebular volume. In the case of H^+ and O^{2+} , if there is an appreciable amount of O in other states apart of O^{2+} , the value of $t^2(\text{H}^+)$ may differ from $t^2(\text{O}^{2+})$. Based on a set of Cloudy photoionization models with different input parameters, Kingdon & Ferland (1995) derived t^2 in two manners: as t_{str}^2 from the formal definition of Eq. (8) and the t_{obs}^2 obtained from the comparison of equations (11) and (13). They found that generally $t_{\text{str}}^2 \neq t_{\text{obs}}^2$, with the difference increasing with the T_{eff} of the ionizing sources. However, for the T_{eff} typical of the ionizing stars of H II regions (between 30,000 and 50,000 k), the approximation $t_{\text{str}}^2 \approx t_{\text{obs}}^2$ seems to be valid. The main drawback one faces in determining t_{obs}^2 is its high intrinsic uncertainty. As we mentioned in § 4.4, the determination of temperature based on the Balmer or Paschen discontinuities is very sensitive to the noise level of the nebular continuum around the position of the discontinuities. Even with the procedure followed in this work, fitting the continuum at both sides of the discontinuities several times up to a statistically representative number of tests, the

Table 16. t^2 and T_0 derived from the different combinations of Eq. (11) and Eq. (12) with Eq. (13), Eq. (14) and Eq. (15) for the spectra of all cuts combined.

	T([O III])		T([S III])		T([N II])	
	t^2	T_0	t^2	T_0	t^2	T_0
T(H I) _{BJ}	0.020 ± 0.017	7770 ± 850	0.051 ± 0.030	8240 ± 980	0.068 ± 0.023	8510 ± 960
T(H I) _{PJ}	0.019 ± 0.025	7800 ± 1260	0.050 ± 0.042	8250 ± 1420	0.068 ± 0.033	8530 ± 1430
T(He I)	0.018 ± 0.012	7840 ± 520	0.054 ± 0.024	8160 ± 570	0.075 ± 0.018	8360 ± 570

inherent dispersion in the resulting temperature is larger than what is obtained from diagnostics based on CEL ratios. The sources of uncertainty in $T(\text{He I})$ are slightly smaller, but they are still important. Uncertainties on T_e of a similar order are expected when using Eq. (9). Assuming the two ionization zones scheme for H II regions, a better approximation to t^2 can be obtained using equations (16) and (17), proposed by Peimbert et al. (2002).

$$\gamma = \frac{\int n_e (\text{O}^+) dV}{\int n_e n (\text{O}^+) dV + \int n_e n (\text{O}^{2+}) dV}, \quad (16)$$

$$T_0(\text{H}^+) = \gamma T_0(\text{O}^+) + (1 - \gamma) T_0(\text{O}^{2+}). \quad (17)$$

To use Eq. (17), we need to estimate the fraction of the total O in O^+ form. For the spectrum of the combined cuts, γ varies from 0.36 to 0.23 according to whether the abundances are determined from RLs or CELs, respectively. A reasonable approximation is to take the average value $\gamma \approx 0.3$. On the other hand, He^+ should be present in both, the O^+ and O^{2+} zones. Although there may be coexistence of He^0 and H^+ , the volume that He^0 occupies should be small at the ionization conditions of the Orion Nebula and it can be assumed that the volume containing H^+ and He^+ should be approximately the same. This assumption is reinforced by the fact that the parameter $\eta = (\text{O}^+/\text{O}^{2+})(\text{S}^2+/S^+)$ (Vilchez & Pagel 1988), which is a measure of the radiation hardness and is correlated with the T_{eff} of the ionizing source, has a value of $\log(\eta) = 0.74$ for the combined cuts spectrum. Pagel et al. (1992) showed that for $\log(\eta) < 0.9$, the amount of He^0 is negligible for a large variety of photoionization models. Therefore, we can assume $T_0(\text{H}^+) \approx T_0(\text{He}^+)$ and $t^2(\text{H}^+) \approx t^2(\text{He}^+)$. Based on the previous discussion, we combined Eq. (11) and Eq. (12) for the combined cuts spectrum, obtaining $t^2(\text{H}^+) \approx 0.036$ and $T_0(\text{H}^+) \approx 8000$ K. Using these values in Eq. (17) and assuming that the volume occupied by O^+ and N^+ is the same, and that, at first order, $\frac{T([\text{OIII}])}{T([\text{NII}])} \approx \frac{T_0(\text{O}^{2+})}{T_0(\text{N}^+)} \approx 0.85$, we obtain $T_0(\text{O}^{2+}) \approx 7580$ and $T_0(\text{N}^+) \approx 8950$. Then, from Eq. (13) and Eq. (15), we estimate $t_{\text{high}}^2 = t^2(\text{O}^{2+}) \approx 0.025$ and $t_{\text{low}}^2 = t^2(\text{N}^+) \approx 0.050$.

The remarkably good agreement between the values obtained with Eq. (17) and those presented in Table 16 reinforces the suitability of the temperature fluctuations paradigm to describe the results in the "combined cuts" spectrum. Considering the numerical values obtained for the combined cuts spectrum, we adopt the average values $t_{\text{high}}^2 = 0.021 \pm 0.003$, $t_{\text{inter}}^2 = 0.051 \pm 0.009$ and $t_{\text{low}}^2 = 0.064 \pm 0.011$, where the uncertainties correspond to the standard deviation of the average. Unfortunately, $T(\text{H I})$ based on the Balmer and Paschen discontinuities can not be calculated for the individual components of the different cuts, and the estimations of t^2 must rely exclusively on the calculated $T(\text{He I})$. However, cal-

culations following the same procedure as the previously described to obtain the values presented in Table 16 for the individual components of each cut show similar results. These values are presented in Table A6, indicating that the values adopted for the combined cuts spectrum may be also representative for the other components of each cut.

Using Eq. (15), Eq. (14) and Eq. (13) with the adopted t^2 values for each ionization zone, T_0 is estimated in each case for all components. Following the same scheme described in § 5.1, we estimate the ionic abundances within the the paradigm of temperature inhomogeneities and results are shown in Table 17.

7 THE ABUNDANCE DISCREPANCY FACTOR

A major problem in the analysis of photoionized regions is the discrepancy between the chemical abundances derived from RLs and CELs, known as the abundance discrepancy (AD) problem. The relatively weak RLs, give systematically higher abundances than CELs. This difference is commonly quantified through the abundance discrepancy factor (ADF, Liu et al. 2000), defined here as:

$$\text{ADF} \left(X^i \right) = \log \left(\frac{n(X^i)_{\text{RLs}}}{n(X^i)_{\text{CEls}}} \right). \quad (18)$$

There is an extensive collection of works dedicated to this problem in the literature (see Torres-Peimbert et al. 1980; Liu et al. 2001; Stasińska et al. 2007; Tsamis et al. 2011; Nicholls et al. 2012, and references therein). Although there is no definitive solution, there are several hypotheses to explain the AD. For example, temperature fluctuations (see § 6), which would primarily affect abundances based on CELs, underestimating the real values; semi-ionized gas clumps, overestimating abundances based on RLs and underestimating those of CELs; chemical inhomogeneities with different physical conditions, affecting both estimates depending on each specific case and so on. It is even possible that the AD is the result of the sum of various phenomena affecting each nebula in a different degree. Using a set of deep spectra of Galactic H II regions, García-Rojas & Esteban (2007) found that the ADF is fairly constant around a factor 2, showing no trend with ionization degree, T_e or the effective temperature of the ionizing stars. They found that temperature fluctuations is the most likely explanation for the AD in H II regions.

In Table 18, we present the ADF obtained from O^+ , O^{2+} , Ne^{2+} and C^{2+} abundances determined from RLs and CELs for each component. The abundances based on CELs do not consider temperature fluctuations. In the case of C^{2+} , the value of the abundance from CELs have been taken from the UV observations reported by Walter et al. (1992). We have considered the mean value of their positions number 5 and 7, which are the nearest to our slit and give $12 + \log(\text{C}^{2+}/\text{H}^+) = 7.835$. We do not estimate the $\text{ADF}(\text{C}^{2+})$ for the high-velocity component since the UV CELs values can only

Table 17. Chemical abundances based on CEL's derived within the paradigm of temperature inhomogeneities ($t^2 > 0$).

Ion	Cut 1		Cut 2		Cut 3		Cut 4	Combined cuts
	Nebula	Shock	Nebula	Shock	Nebula	Nebula	Nebula	
O ⁺	8.18 ^{+0.10} _{-0.08}	7.65 ^{+0.20} _{-0.12}	8.14 ^{+0.12} _{-0.09}	8.14 ^{+0.29} _{-0.16}	8.05 ^{+0.13} _{-0.09}	8.12 ^{+0.13} _{-0.09}	8.05 ^{+0.11} _{-0.08}	8.05 ^{+0.11} _{-0.08}
O ²⁺	8.48 ^{+0.06} _{-0.05}	8.72 ^{+0.04} _{-0.03}	8.50 ^{+0.05} _{-0.04}	8.67 ± 0.04	8.51 ± 0.04	8.52 ^{+0.05} _{-0.04}	8.52 ^{+0.05} _{-0.04}	8.53 ^{+0.05} _{-0.04}
N ⁺	7.18 ^{+0.05} _{-0.04}	6.36 ^{+0.11} _{-0.08}	7.17 ^{+0.07} _{-0.05}	6.80 ^{+0.15} _{-0.10}	7.09 ^{+0.07} _{-0.05}	7.16 ^{+0.07} _{-0.06}	7.07 ^{+0.06} _{-0.05}	7.07 ^{+0.06} _{-0.05}
Ne ²⁺	7.86 ^{+0.07} _{-0.06}	8.12 ± 0.04	7.89 ^{+0.06} _{-0.05}	8.02 ^{+0.05} _{-0.04}	7.91 ^{+0.05} _{-0.04}	7.94 ^{+0.06} _{-0.05}	7.93 ^{+0.06} _{-0.05}	7.93 ^{+0.06} _{-0.05}
S ⁺	5.75 ^{+0.07} _{-0.06}	5.04 ^{+0.12} _{-0.08}	5.75 ^{+0.07} _{-0.06}	5.58 ^{+0.16} _{-0.11}	5.70 ^{+0.08} _{-0.07}	5.77 ^{+0.08} _{-0.06}	5.66 ^{+0.07} _{-0.06}	5.66 ^{+0.07} _{-0.06}
S ²⁺	6.87 ^{+0.05} _{-0.04}	7.01 ^{+0.06} _{-0.05}	6.94 ^{+0.06} _{-0.05}	6.99 ^{+0.07} _{-0.06}	6.95 ^{+0.06} _{-0.05}	6.91 ± 0.05	6.94 ± 0.05	6.94 ± 0.05
Cl ⁺	3.87 ± 0.05	3.09 ^{+0.16} _{-0.14}	3.86 ^{+0.06} _{-0.05}	<3.49	3.81 ^{+0.06} _{-0.05}	3.90 ^{+0.07} _{-0.06}	3.76 ^{+0.06} _{-0.05}	3.76 ^{+0.06} _{-0.05}
Cl ²⁺	5.00 ^{+0.07} _{-0.06}	5.15 ^{+0.09} _{-0.07}	5.06 ^{+0.08} _{-0.06}	5.22 ^{+0.10} _{-0.08}	5.09 ^{+0.08} _{-0.06}	5.08 ^{+0.08} _{-0.06}	5.07 ^{+0.07} _{-0.06}	5.07 ^{+0.07} _{-0.06}
Cl ³⁺	3.30 ± 0.06	3.71 ± 0.05	3.38 ± 0.04	3.51 ^{+0.10} _{-0.11}	3.43 ± 0.04	3.55 ^{+0.05} _{-0.04}	3.48 ^{+0.06} _{-0.05}	3.48 ^{+0.06} _{-0.05}
Ar ²⁺	6.42 ± 0.04	6.51 ± 0.03	6.42 ^{+0.04} _{-0.03}	6.48 ^{+0.04} _{-0.03}	6.43 ± 0.03	6.40 ^{+0.04} _{-0.03}	6.43 ^{+0.04} _{-0.03}	6.43 ^{+0.04} _{-0.03}
Ar ³⁺	4.55 ^{+0.07} _{-0.06}	4.84 ^{+0.05} _{-0.04}	4.63 ^{+0.06} _{-0.05}	4.68 ^{+0.08} _{-0.07}	4.66 ^{+0.05} _{-0.04}	4.79 ^{+0.06} _{-0.05}	4.69 ^{+0.06} _{-0.05}	4.69 ^{+0.06} _{-0.05}
Fe ^{2+*}	5.93 ± 0.02	6.11 ± 0.05	5.97 ± 0.02	5.94 ± 0.05	5.94 ± 0.02	5.92 ± 0.03	5.96 ± 0.01	5.96 ± 0.01
Fe ^{2+**}	5.75 ± 0.02	5.84 ± 0.06	5.81 ± 0.02	5.77 ± 0.06	5.75 ± 0.02	5.72 ± 0.03	5.76 ± 0.02	5.76 ± 0.02
Fe ³⁺	5.99 ^{+0.16} _{-0.12}	6.59 ^{+0.12} _{-0.10}	6.00 ^{+0.12} _{-0.09}	<6.68	6.23 ^{+0.18} _{-0.16}	6.05 ^{+0.16} _{-0.13}	6.16 ^{+0.18} _{-0.15}	6.16 ^{+0.18} _{-0.15}
Ni ²⁺	4.52 ± 0.19	4.68 ± 0.09	4.51 ± 0.18	4.57 ^{+0.18} _{-0.12}	4.48 ± 0.16	4.51 ± 0.13	4.54 ± 0.11	4.54 ± 0.11

* indicates that T_e (high) was used.

** indicates that T_e (low) was used.

be compared with the nebular component. It is a common procedure to estimate t^2 by looking for a temperature T_0 that produces the agreement between the abundance determined from CELs and RLs, but this is only valid if the temperature fluctuations are the cause of AD. We remark that we do not use this procedure in this work, since this hypothesis might not be the only valid for the high velocity components. Our determinations of t^2 are exclusively those described in § 6. Therefore $t^2 > 0$, does not necessarily mean $\text{ADF} = 0$, unless the measured value of t^2 is compatible with this.

From Table 18, is remarkable that the ADF is slightly different for each ion and higher in the high-velocity components. Using the value of t^2 adopted for each ionization zone of the nebular components (see Table 17), we obtain abundances based on CELs consistent with those determined from RLs and, therefore, making the ADF consistent with zero within the uncertainties. This suggests that the temperature fluctuation paradigm is capable of explaining the difference between the ADF in O⁺ and O²⁺. However, considering the high velocity components, the ionic abundances determined from CELs assuming $t^2 > 0$ give smaller values for the ADF but is not zero. For example, in the case of the high-velocity component of cut 3, the ADF(O²⁺) goes from 0.33 to 0.17 when considering $t^2 = 0.021$. This suggests the presence of another effect apart the classic description of temperature inhomogeneities.

8 TOTAL ABUNDANCES

We have to use ionization correction factors (ICFs) to estimate the contribution of the unseen ions in the total abundance of some elements for some studied components. Following the analysis of the different ICF schemes for C, N, Ne, S and Ar done by Arellano-Córdova et al. (2020), we adopt the ICFs shown in Table 19 for these elements. In the case of He, Fe and Ni, we use the ICFs from Kunth & Sargent (1983), Rodríguez & Rubin (2005) and Delgado-Ingla et al. (2016), respectively. Results of total abundances based on CELs are presented in Table 20 and in Table 21, for the case of

$t^2 = 0$ and $t^2 > 0$. Total abundances based in RLs are presented in Table 22. In this case, we do not expect significant changes in the total abundances within the temperature fluctuation paradigm due to the low dependence on temperature of RLs. The ICFs are generally based on the degree of ionization measured with the ionic abundances of O. For consistency, in the case of abundances based on CELs, we use the degree of ionization determined also with CELs. Analogously in the case of RLs.

8.1 Total abundances with CELs

8.1.1 Oxygen, Chlorine and Ar

In the cases of O and Cl, all the present ionization states are observed and the calculation of their total abundance does not require ICF. In the case of the shock component of cut 3, we could only estimate an upper limit for Cl⁺. However, even if we assume this upper limit as the real value, the contribution of this ion to the total Cl abundance is negligible. In the case of Ar, the ICF model of Izotov et al. (2006) shows that the contribution of Ar⁺ to the total abundance of Ar is negligible in all the analyzed components. Thus, Ar/H=Ar²⁺/H⁺+Ar³⁺/H⁺. As we analyzed in § 5.1.1, the Cl/O ratio is highly consistent with the solar value adopted by Lodders (2019) for the case of $t^2 = 0$. In the case of $t^2 > 0$, the average Cl/O value for the different components is -3.57 ± 0.03 also consistent with the solar value of -3.50 ± 0.09 . In the case of Ar, the average value of Ar/O is -2.16 ± 0.03 for $t^2 = 0$ and -2.23 ± 0.03 for $t^2 > 0$, both within the value -2.23 ± 0.12 adopted by Lodders.

8.1.2 Nitrogen, Neon and Sulphur

The estimation of the total abundances of N, Ne and S strongly depends on the ICFs shown in Table 19. The case of N is notorious, in a scheme of the form $N = \text{ICF} \times N^+/H^+$, the ICF value reaches values between 4 and 16 for the nebular and the high-velocity components, respectively. Given the high degree of ionization of M42

Table 18. Abundance discrepancy factor (ADF) for different ions in the components of each cut.

Cut	Component	ADF(O ⁺)	ADF(O ²⁺)	ADF(Ne ²⁺)	ADF(C ²⁺) [*]
1	Nebular	0.46 ± 0.14	0.15 ± 0.07	-	0.51 ± 0.03
2	High Velocity	<0.55	0.29 ± 0.10	0.79 ± 0.09	-
2	Nebular	0.42 ± 0.12	0.17 ± 0.05	0.37 ± 0.04	0.52 ± 0.03
3	High Velocity	<0.12	0.33 ± 0.11	-	-
3	Nebular	0.52 ± 0.14	0.17 ± 0.06	0.31 ± 0.15	0.51 ± 0.03
4	Nebular	0.46 ± 0.14	0.17 ± 0.06	-	0.50 ± 0.02
Combined cuts		0.44 ± 0.12	0.21 ± 0.05	-	0.54 ± 0.03

* We adopt $12 + \log(C^{2+}/H^+) = 7.835$ from UV CELs considering the slit positions 5 and 7 of [Walter et al. \(1992\)](#).

Table 19. ICFs used to estimate the abundance of unseen ions.

Element	ICF Reference
He	Kunth & Sargent (1983)
C	Berg et al. (2019)
N	Peimbert & Costero (1969)
Ne	Izotov et al. (2006)
S	Stasińska (1978)
Ar	Rodríguez & Rubin (2005)
Fe	Delgado-Ingla et al. (2016)
Ni	Delgado-Ingla et al. (2016)

and even more in the high-velocity components, the calculation of total N may be somewhat uncertain. However, in the nebular components for $t^2 = 0$, the average value of N/O is -0.86 ± 0.02 , in complete agreement with the suggested solar value of -0.88 ± 0.14 ([Lodders 2019](#)). In the case of $t^2 > 0$ for the nebular components, the value of the ratio N/O = -0.98 ± 0.02 suggests an underestimation of N. In the high-velocity components, both in the case of $t^2 = 0$ and in $t^2 > 0$, the N/O ratios show that the central value of N may be underestimated. The most likely explanation is an uncertain ICF value under the conditions of such a high degree of ionization. Ne/O values do not change appreciably between nebular and high-velocity components. The average values are -0.65 ± 0.03 and -0.61 ± 0.02 for case $t^2 = 0$ and $t^2 > 0$, respectively, somewhat smaller than the solar value of -0.58 ± 0.12 ([Lodders 2019](#)), but within the error range. S/O values also do not differ appreciably between high-velocity and nebular components. For $t^2 = 0$ the average value is S/O = -1.51 ± 0.05 and for $t^2 > 0$ S/O = -1.64 ± 0.05 , while the solar value from [Lodders \(2019\)](#) is -1.58 ± 0.08 .

8.1.3 Nickel

Ni/H abundances are estimated using the ICF scheme derived by [Delgado-Ingla et al. \(2016\)](#) and are presented in Table 20 and Table 21 for $t^2 = 0$ and $t^2 > 0$, respectively. The estimation of this abundance is rather uncertain as discussed in § 5.1.2.

8.1.4 Iron

Considering the absence of He II lines in our spectra, we do not expect to have Fe⁴⁺ in the nebula and therefore $\text{Fe/H} = \text{Fe}^{2+}/\text{H}^+ + \text{Fe}^{2+}/\text{H}^+ + \text{Fe}^{3+}/\text{H}^+$. We have determined the abundance of Fe²⁺ and Fe³⁺ for all the components of each cut with the exception of the high-velocity component of cut 3, where we could only

estimate an upper limit to Fe³⁺. In the high velocity components, the absence of usually relatively intense [Fe II] lines as $\lambda\lambda 4287$, 5158 and 5262, together with the high ionization degree of the gas, are indicative of a negligible contribution of Fe⁺ to the total abundance. Thus, in these cases $\text{Fe/H} = \text{Fe}^{2+}/\text{H}^+ + \text{Fe}^{3+}/\text{H}^+$. In the nebular components, although a large number of [FeII] lines have been detected, their emission is mainly produced by fluorescence ([Rodríguez 1999; Verner et al. 2000](#)). Therefore, most of the observed lines will not provide reliable estimates of Fe⁺ abundance. Unfortunately, [Fe II] $\lambda 8617$, a line almost insensitive to fluorescence ([Lucy 1995; Baldwin et al. 1996](#)) can not be observed due to the physical gap of the CCDs in the Red Arm of UVES. However, previous studies with direct estimations of Fe⁺ in the Orion Nebula as [Rodríguez \(2002\)](#) or [Mesa-Delgado et al. \(2009\)](#), obtain $\text{Fe}^+/\text{Fe}^{+2}$ ratios between 0.05 and 0.27. Considering the approximation $\text{Fe/H} = \text{Fe}^{2+}/\text{H}^+ + \text{Fe}^{3+}/\text{H}^+$, the neglected Fe^+/H^+ ratio would contribute to Fe/H up to 0.06 dex in the worst case (calculating $\text{Fe}^{+2}/\text{H}^+$ with $T_e(\text{high})$ and assuming $\text{Fe}^+/\text{Fe}^{+2} = 0.27$). This maximum increase is within the range of uncertainties associated with the sum of Fe²⁺ and Fe³⁺ abundances and therefore, it seems reasonable to consider $\text{Fe/H} \approx \text{Fe}^{2+}/\text{H}^+ + \text{Fe}^{3+}/\text{H}^+$ for the nebular component as well.

[Rodríguez & Rubin \(2005\)](#) proposed two ICFs for Fe, one derived from photoionization models and the other from data with detection of [Fe III] and [Fe IV] lines. The values of Fe/H obtained using both ICFs are discrepant, perhaps due to errors in the atomic data of the ions involved, and the true total Fe abundance is expected to be in between the values obtained from both ICFs ([Rodríguez & Rubin 2005; Delgado-Ingla et al. 2014](#)). We use the described ICFs only in the high-velocity component of cut 3. The abundance Fe/H for that component is presented as a limited range, defined from the predictions of both ICFs, as shown in Table 20 and Table 21.

In the high velocity component of cut 2, the abundance of Fe is higher than in the nebular components independently of whether the temperature $T_e(\text{low})$ or $T_e(\text{high})$ is taken to derive $\text{Fe}^{2+}/\text{H}^+$. The same behavior is observed in the high-velocity component of cut 3 for $t^2 = 0$, although the uncertainty in Fe/H do not allow us to be conclusive in the case of $t^2 > 0$ when Fe^{2+} is derived with $T_e(\text{low})$. However, as it is discussed in § 4.2, the representative temperature to derive $\text{Fe}^{2+}/\text{H}^+$ in HH529II and HH529III is likely to be $T_e(\text{high})$ while in the nebular components is $T_e(\text{low})$.

In the case of $t^2 = 0$, the average Fe/O ratio in the nebular components is -2.53 ± 0.02 , while for HH529II is -2.14 ± 0.08 which represents an increase in the total abundance of gaseous Fe by a factor of 2.45. The same increase is observed in case of $t^2 > 0$.

For HH529III the increase is in a range of between a factor 1.35 and 2.40 in the case of $t^2 = 0$, while at $t^2 > 0$ it is limited to a factor of 1.30. The solar value recommended by Lodders (2019) is $\text{Fe}/\text{O} = -1.28 \pm 0.08$, This implies that only 6% of the total Fe is present gaseous phase in the nebular component, while this fraction amounts to 14% for HH529II and between 8% and 14% for HH529III.

8.2 Total abundances with RLs

8.2.1 Oxygen

The total O abundances based on RLs are determined directly from $\text{O}/\text{H} = \text{O}^+/\text{H}^+ + \text{O}^{2+}/\text{H}^+$. In the high-velocity components, the absence of O I RLs indicate an small contribution of O^+/H^+ in the total O/H abundance. In § 5.2.3 we estimate an upper limit to this ionic abundance in HH529II and HH529III, which can contribute up to 0.05 dex to the total O/H value. Thus, for these high-velocity components the total O/H abundance is determined from the O^{2+}/H^+ value considering the possible O^+/H^+ contribution within the error range.

8.2.2 Helium

Considering both the absence of an ionization front and the emission of lines of neutral elements together with a hardness radiation of $\log(\eta) < 0.9$ (see § 6), it is likely that the fraction He^0/H^+ in the high velocity components is negligible. For these cases we take $\text{He}/\text{H} = \text{He}^+/\text{H}^+$. In the nebular components, we estimate the fraction of neutral helium within the ionized zone with the ICF scheme of Kunth & Sargent (1983). We estimate that the He^0/H^+ fraction is approximately 10%, consistent with the other ICF schemes tested in Méndez-Delgado et al. (2020) for the Orion Nebula. The He/H abundances are practically the same among all the components in all cuts, as it is shown in Table 22. However, the dependence of the total amount of He^0 with the T_{eff} of the ionizing star is not considered in the usual ICF schemes for He and may introduce errors as it is discussed by Delgado-Ingla et al. (2014) for Planetary Nebulae. Despite this, in the Orion Nebula, we expect to have a small contribution of He^0/H^+ , where the radiation softness parameter gives values of $\log(\eta) < 0.9$ also for the nebular components.

8.2.3 Carbon and Neon

In the case of the high-velocity components, due to the high degree of ionization estimated from the ionic O abundances based on RLs, we expect to have a negligible contribution of C^+/H^+ in the total C/H abundance. We expect the same in the case of Ne^+/H^+ for HH529II. In these cases we take ICF=1. For the nebular components, we use the ICF from Peimbert & Costero (1969) for Ne, as in § 8.1.2 but using the ionic abundances of O based on RLs. The resulting Ne/O ratio for RLs is -0.44 ± 0.03 and -0.23 ± 0.10 for the nebular components and HH529II respectively. This indicates that the relative abundance of Ne over O is higher using RLs than CELs (See § 8.1.2), although in the nebular components, both cases are in agreement with the solar value of -0.58 ± 0.12 (Lodders 2019), given the wide range of uncertainties of this quantity. In the case of HH529II, the Ne/O is out from the solar value and may indicate an overestimation of $\text{Ne}^{2+}/\text{H}^+$.

To estimate the contribution of C^+/H^+ to the total C/H abundance, for the nebular components, we use the ICF presented by Berg et al. (2019). It is important to note that this ICF may

not be completely adequate to our case, for two main reasons: it has been optimized for low-metallicity objects (up to $\text{O}/\text{H}=8.0$) and indirectly involves the use of CELs, since it depends on $\log([\text{O III}] \lambda 5007/[\text{O II}] \lambda 3727)$. Despite this, the results obtained with this scheme are more consistent with the expected solar values, compared to other ICFs published in the literature, as is discussed by Arellano-Córdova et al. (2020). For comparison, we present the C/H derived with the ICF of Amayo et al. (in prep) (private communication), whose scheme is optimized for a wider range of metallicity. Table 22 shows that the results with both ICFs are consistent, although there is a slight difference, probably due to an overestimation of C/H by the ICF of Berg et al. (2019). The average C/O value for the nebular components is -0.20 ± 0.02 using the ICF of Berg et al. (2019) and -0.26 ± 0.02 using the scheme of Amayo et al. (in prep). This last value is the most consistent one with the recommended solar value of -0.26 ± 0.09 . The C/O value for HH529II is -0.37 ± 0.08 while for HH529III is -0.28 ± 0.12 .

8.3 Overmetallicity in the high-velocity components?

A notable aspect among the total abundances calculated and commented previously, is the fact that the metallic abundances are higher in HH529II and HH529III than in the nebular components. The clearest example is the O, an element whose relative abundance does not require an ICF. In this case, we have a difference of between 0.10 and 0.14 dex with the abundances present in the nebular components, both in the case of abundances based on CELs and RLs.

This difference is in accordance with the 0.12 ± 0.03 dex of O which may be depleted into dust grains in the Orion Nebula (Mesa-Delgado et al. 2009). Nevertheless, the abundance of elements like Ar, Ne, S and Cl grows proportionally to that of O, so the Ar/O, Ne/O, S/O and Cl/O ratios do not change appreciably between the nebular components and the high-velocity ones. Since Ar and Ne are noble elements, it is not expected to have them depleted into dust grains. Thus, this indicate that the increase of the O/H abundance in HH529II and HH529III is not entirely due to the destruction of dust grains. On the other hand, as it was discussed in § 8.1.4, the abundance of Fe/H is higher in the high-velocity components and also the Fe/O ratio, therefore an increase in the gaseous proportion of Fe, linked to a destruction of dust grains is confirmed.

The fact that the increase of around 0.12 dex in the O/H abundance is also observed in the determination based on RLs rules out the possibility that it is due to an inadequate estimation of the temperature used to calculate the ionic abundances based on CELs within the classic Direct-Method. In addition to this, the same behaviour was observed by Blagrave et al. (2006), using different data with which they studied separately the high-velocity emission that includes part of HH529II and HH529III. The same data from Blagrave et al. (2006) was reanalyzed by Simón-Díaz & Stasińska (2011) finding again a higher O/H abundance in the HH object than in the nebular component. Due to the above, an observational error or in the procedure to estimate the chemical abundances is unlikely.

One possibility is that the source of origin of the Herbig-Haro object has somehow expelled a knot of H-deficient material within the main flow of gas. In this scenario, since the heating of the gas is mainly due by photoionization of H and He and cooled by collisional excitation of metallic ions (Péquignot et al. 2002), we would expect a lower temperature in the metallic knot, up to an order of magnitude (Péquignot et al. 2002). However, since the main coolants are the IR fine-structure CELs as $[\text{O III}] 52, 88 \mu\text{m}$ (Yuan et al. 2011), the temperature diagnostics based on optical CELs, would show mainly

Table 20. Total abundances based on CELs with $t^2 = 0.0$.

Element	Cut 1		Cut 2		Cut 3		Cut 4		Combined cuts
	Nebula	Shock	Nebula	Shock	Nebula	Shock	Nebula	Shock	
O	8.45 ± 0.02	8.57 ± 0.03	8.46 ± 0.03	8.59 ± 0.04	8.45 ± 0.03	8.47 ± 0.03	8.46 ± 0.03	8.46 ± 0.03	
N	7.57 ± 0.04	$7.40^{+0.16}_{-0.10}$	$7.62^{+0.07}_{-0.05}$	$7.37^{+0.26}_{-0.14}$	$7.60^{+0.08}_{-0.07}$	$7.64^{+0.08}_{-0.06}$	$7.60^{+0.06}_{-0.05}$	$7.60^{+0.06}_{-0.05}$	
Ne	7.81 ± 0.04	7.94 ± 0.03	7.82 ± 0.04	7.90 ± 0.04	7.83 ± 0.03	7.86 ± 0.04	7.82 ± 0.04	7.82 ± 0.04	
S	6.89 ± 0.04	$7.18^{+0.07}_{-0.06}$	$6.96^{+0.08}_{-0.09}$	$7.05^{+0.08}_{-0.06}$	6.98 ± 0.05	6.94 ± 0.05	6.98 ± 0.04	6.98 ± 0.04	
Cl	4.92 ± 0.06	5.03 ± 0.05	4.97 ± 0.06	5.11 ± 0.06	4.99 ± 0.06	4.99 ± 0.06	4.97 ± 0.05	4.97 ± 0.05	
Ar	6.32 ± 0.03	6.40 ± 0.02	6.32 ± 0.03	6.38 ± 0.03	6.34 ± 0.02	6.30 ± 0.03	6.33 ± 0.03	6.33 ± 0.03	
Fe*	6.03 ± 0.06	6.42 ± 0.07	6.07 ± 0.04	$6.19 < \text{Fe} < 6.44$	6.06 ± 0.05	6.05 ± 0.06	6.08 ± 0.05	6.08 ± 0.05	
Fe**	5.91 ± 0.07	6.34 ± 0.08	5.94 ± 0.05	$5.97 < \text{Fe} < 6.20$	5.94 ± 0.07	5.92 ± 0.08	5.95 ± 0.07	5.95 ± 0.07	
Ni	4.59 ± 0.14	$5.12^{+0.15}_{-0.10}$	$4.58^{+0.18}_{-0.17}$	$4.71^{+0.18}_{-0.12}$	$4.60^{+0.17}_{-0.16}$	$4.62^{+0.13}_{-0.12}$	$4.67^{+0.11}_{-0.10}$	$4.67^{+0.11}_{-0.10}$	

* indicates that T_e (high) was used.** indicates that T_e (low) was used.**Table 21.** Total abundances based on CELs with $t^2 > 0.0$.

Element	Cut 1		Cut 2		Cut 3		Cut 4		Combined cuts
	Nebula	Shock	Nebula	Shock	Nebula	Shock	Nebula	Shock	
O	8.66 ± 0.05	8.76 ± 0.04	8.66 ± 0.05	8.78 ± 0.07	8.64 ± 0.04	8.67 ± 0.05	8.65 ± 0.05	8.65 ± 0.05	
N	$7.66^{+0.11}_{-0.08}$	$7.45^{+0.35}_{-0.16}$	$7.69^{+0.14}_{-0.10}$	$7.41^{+0.44}_{-0.21}$	$7.68^{+0.16}_{-0.10}$	$7.71^{+0.15}_{-0.10}$	$7.68^{+0.13}_{-0.09}$	$7.68^{+0.13}_{-0.09}$	
Ne	8.04 ± 0.08	8.16 ± 0.04	8.05 ± 0.07	$8.13^{+0.09}_{-0.08}$	8.04 ± 0.06	$8.08^{+0.08}_{-0.07}$	$8.05^{+0.07}_{-0.06}$	$8.05^{+0.07}_{-0.06}$	
S	6.95 ± 0.05	$7.24^{+0.10}_{-0.07}$	7.03 ± 0.06	$7.10^{+0.11}_{-0.08}$	$7.05^{+0.07}_{-0.06}$	$7.01^{+0.06}_{-0.05}$	$7.05^{+0.06}_{-0.05}$	$7.05^{+0.06}_{-0.05}$	
Cl	5.04 ± 0.06	5.17 ± 0.09	5.10 ± 0.07	5.24 ± 0.10	5.12 ± 0.07	5.12 ± 0.07	5.10 ± 0.07	5.10 ± 0.07	
Ar	6.44 ± 0.04	6.52 ± 0.03	6.43 ± 0.04	6.49 ± 0.04	6.44 ± 0.03	6.42 ± 0.04	6.44 ± 0.04	6.44 ± 0.04	
Fe*	6.26 ± 0.09	6.71 ± 0.09	6.29 ± 0.06	$6.32 < \text{Fe/H} < 6.48$	6.41 ± 0.12	6.29 ± 0.09	6.37 ± 0.11	6.37 ± 0.11	
Fe**	6.19 ± 0.10	6.66 ± 0.10	6.22 ± 0.07	$6.15 < \text{Fe/H} < 6.31$	6.35 ± 0.14	6.22 ± 0.11	6.31 ± 0.13	6.31 ± 0.13	
Ni	4.70 ± 0.19	$5.22^{+0.26}_{-0.13}$	$4.71^{+0.19}_{-0.18}$	$4.81^{+0.27}_{-0.23}$	$4.71^{+0.18}_{-0.16}$	$4.72^{+0.15}_{-0.13}$	$4.78^{+0.13}_{-0.12}$	$4.78^{+0.13}_{-0.12}$	

* indicates that T_e (high) was used.** indicates that T_e (low) was used.**Table 22.** Total abundances based on RLs.

Element	Cut 1		Cut 2		Cut 3		Cut 4		Combined cuts
	Nebula	Shock	Nebula	Shock	Nebula	Shock	Nebula	Shock	
O	8.71 ± 0.03	8.83 ± 0.07	8.70 ± 0.03	8.84 ± 0.09	8.71 ± 0.03	8.72 ± 0.03	8.73 ± 0.03	8.73 ± 0.03	
He	10.94 ± 0.02	10.95 ± 0.03	10.94 ± 0.01	10.95 ± 0.03	10.94 ± 0.02	10.95 ± 0.02	10.94 ± 0.02	10.94 ± 0.02	
C*	8.56 ± 0.04		8.52 ± 0.03		8.52 ± 0.04		$8.51^{+0.04}_{-0.03}$	$8.51^{+0.04}_{-0.03}$	
C**	$8.48^{+0.08}_{-0.07}$	8.46 ± 0.02	8.45 ± 0.05	8.56 ± 0.03	$8.45^{+0.07}_{-0.06}$	8.44 ± 0.06	$8.45^{+0.06}_{-0.05}$	$8.45^{+0.06}_{-0.05}$	
Ne	-		8.60 ± 0.06	8.26 ± 0.04	-	8.23 ± 0.15	-	-	

* Total abundances of the nebular components derived with the ICF of Berg et al. (2019).

** Total abundances of the nebular components derived with the ICF of Amayo et al. (in prep.).

the physical conditions of the "normal" metallicity gas flowing in the HH. The origin of this hypothetical knot may be in the evaporation of protoplanetary discs around newly formed stars (Yuan et al. 2011), such as the one that gives rise to HH529. A deeper analysis of this scenario requires IR spectroscopy together with bi-abundance photoionization models, which goes beyond the purpose of this work. Subsequent analysis of new photoionized Herbig-Haro objects such as HH529I (in prep.), can give new information.

9 KINEMATICAL ANALYSIS FROM UVES DATA

We calculate the radial velocity of each line in the heliocentric framework by comparing its observed wavelength (after applying the radial velocity correction) with its theoretical wavelength in air. All the theoretical values have been taken from the Atomic Line List v2.05b21 (Van Hoof 2018). Wavelengths from this compilation list are mainly calculated from the theoretical energy difference between the levels connected by the transition. The exception are the hydrogenic lines, which include a weighted average of all the fine structure components.

We detect some evident inaccuracies in the theoretical wavelengths of [Cl III], [Cl IV] and [Ne III] in the Atomic Line List

v2.05b21. This conclusion is based on the discrepant velocities that those lines show with respect to the rest of lines in the shock components, that show fairly similar velocities independently of the ionization state of the ions and the elements (see § 9.1). For example, in the case of [Ne III] $\lambda\lambda$ 3869, 3967, the Atomic Line List v2.05b21 gives $\lambda\lambda$ 3869.07 \pm 0.09 and 3967.79 \pm 0.10 based on the works of Persson et al. (1991) and Feuchtgruber et al. (1997). These wavelengths give velocities about -20 km s $^{-1}$ displaced with respect to the mean velocity obtained for the rest of the lines. In this case, we decided to adopt the wavelengths $\lambda\lambda$ 3868.75 and 3967.46 obtained by Bowen (1955) from high-resolution spectroscopy of nebulae. The [Cl III] and [Cl IV] lines show a similar problem; in this case, we adopt the reference wavelengths used by Esteban et al. (2004) that give consistent velocities. The wavelengths adopted for [S III] lines deserve special attention. The values given by the Atomic Line List v2.05b21 are $\lambda\lambda$ 6312.1 \pm 0.36, 8829.4 \pm 0.49, 9068.6 \pm 0.52 and 9530.6 \pm 0.57, taken from the work by Kaufman & Martin (1993). There is a small (but noticeable at our spectral resolution) discrepancy in the velocity obtained for [S III] λ 6312 and the rest of the lines of about 10 km s $^{-1}$. Assuming the velocities measured for the H I lines and a large number of other bright lines of the shock component, our best estimation of the rest wavelengths of the observed [S III] lines are $\lambda\lambda$ 6312.07 \pm 0.01, 8829.70 \pm 0.01, 9068.93 \pm 0.04 and 9530.98 \pm 0.01.

9.1 Radial velocity structure

In Table A7, we present the average velocity and full width at half maximum (FWHM) of each kind of line observed for the shock and nebular components of cut 2 and the shock component of cut 3. The behaviour of the nebular component of cut 2 is representative of what is observed in the nebular components of the other cuts. In each column, we include in parentheses the number of lines of each kind whose values have been averaged. In this analysis, we discard lines with known blends and those affected by ghosts or by telluric emissions/absorptions. For O I, O II, C II and Ne II lines, we include only the lines used in § 5.2 for abundance determinations, ensuring that they are pure recombination lines and not affected by fluorescence. In the special case of [S III] lines we consider only the λ 6312 line, due to the aforementioned inaccuracies in the theoretical wavelengths of the rest of the [S III] lines. Fig. 14, shows the heliocentric velocity as a function of ionization potential relation for the data collected in Table A7.

From Fig. 14, it is clear that the nebular component presents a pattern consistent with the “blister” model for the Huygens Region of the Orion Nebula (O’Dell 2001; Ferland 2001; O’Dell et al. 2020, and references therein). The basic idea is that a layer of gas of the Orion Molecular Cloud (OMC) facing the direction towards the Sun is ionized by θ^1 Ori C, which is located in the foreground of OMC. As the gas gets ionized, it is accelerated towards the observer. Velocities of [O I], [C I], and [N I] are similar to the average velocity of the molecules in the OMC (~ 28 km s $^{-1}$ Goudis 1982; O’Dell 2018, and references therein). This behaviour has been observed in previous works (Kaler 1967; Fehrenbach 1977; O’Dell & Wen 1992; Esteban & Peimbert 1999) and there is evidence that this emission arise from the partially ionized zone of the nebula. A rapid drop in the observed velocity (which means an increase in velocity compared to the OMC’s systemic velocity) of the ions whose ionization potential are between 6.77 and 13.6 eV is observed for the nebular component. Elements with ionization potentials beyond 13.6 eV exhibit a constant radial velocity around 16.4 ± 0.8 km s $^{-1}$. The difference between the radial velocity pattern of the

nebular component and HH529II (which presents a constant radial velocity, independent of the ionization potential, panel (d) from Fig. 14) shows that the dispersion presented in the subfigures (a), (b) and (c) from Fig. 14 is not due to errors in the measurement of the spectral position of the lines or to a complex velocity structure. It is due to inaccuracies in the rest-frame reference wavelengths. By eliminating the aforementioned dispersion, we demonstrate that the acceleration of the gas in the Orion Nebula is linear with the ionization potential between 6.77 and 13.6 eV, and that is zero after 13.6 eV.

The difference of 5.18 ± 1.25 km s $^{-1}$ between the constant radial velocity patters presented by HH529II and HH529III is due to the presence of unresolved lower velocity components in the cut 3, as its shown in Fig. 15.

In all components, the radial velocities of the O I, O II, C II and Ne II lines that have been used to derive abundances are consistent with the velocity of the CELs of the recombining ions. This reinforces the assumption that they are produced by pure recombination. The clearest case are the O I lines considered here (those from multiplet 1) in the nebular component. If they were not coming from recombination processes, they would be mainly emitted in neutral and partially ionized zones of the nebula, showing a heliocentric velocity similar to the systematic one of the OMC, around ~ 10 Km s $^{-1}$ higher (from the observer’s reference system) than the observed value.

As shown, there is a significant dispersion in the rest-frame theoretical wavelengths, which can be troublesome for kinematic studies with high spectral resolution. From the lines observed in HH529II, and the velocity of -29.08 ± 0.36 , derived from the average of 51 hydrogen lines, we deduce a list of rest-frame wavelengths in air that eliminate the observed dispersion and are more suitable. It should be noted, that these wavelengths are entirely deduced from our observations and assuming that the rest-frame wavelengths of hydrogen are the best studied. The results are appended in a online table.

9.2 Electron temperature from thermal broadening of the line profiles

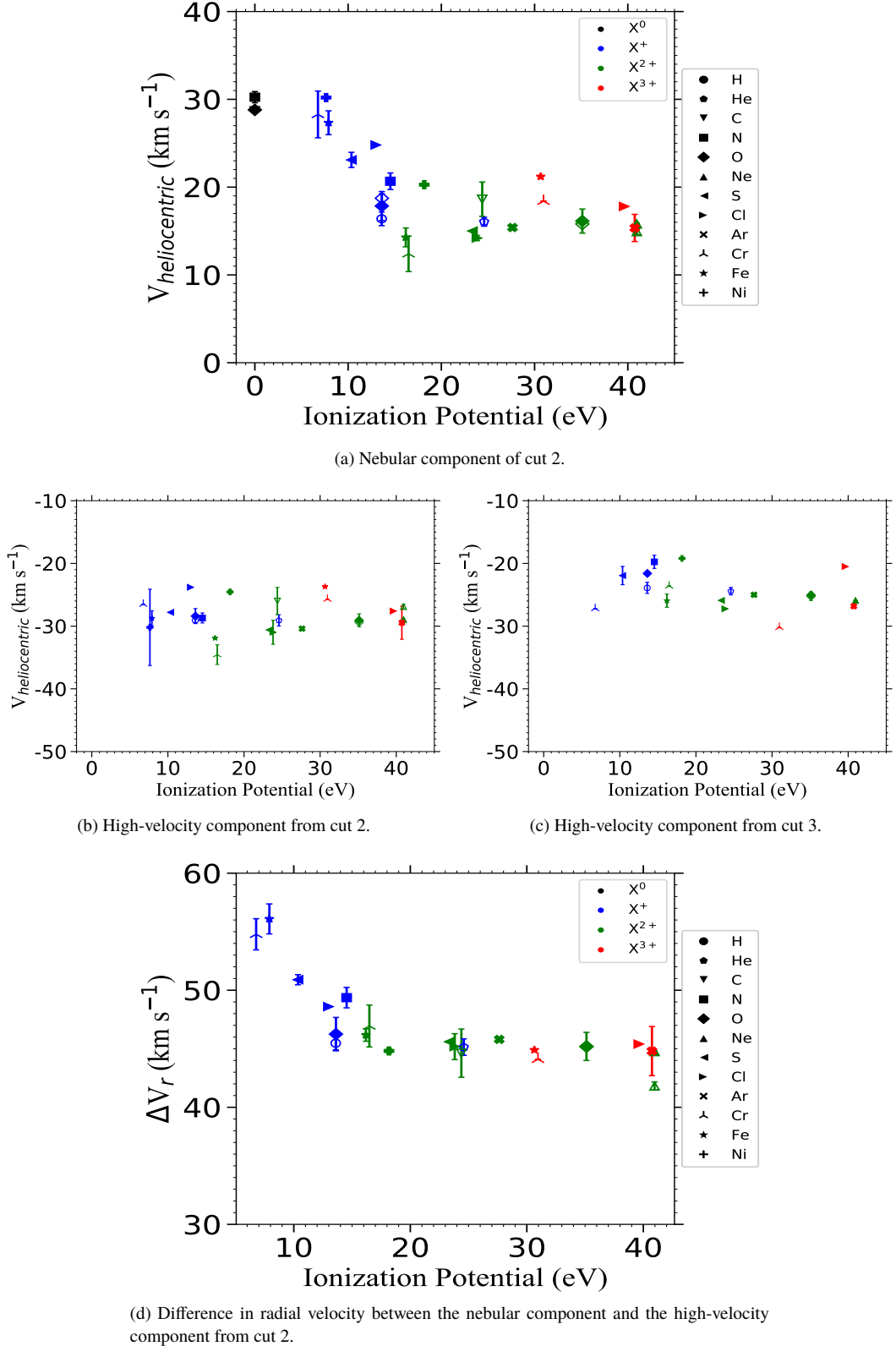
The observed line widths are the result of several physical processes. Apart from the instrumental width, σ_{ins} , the main contributors are the thermal width, σ_{th} , the fine structure broadening, σ_{fs} and the non-thermal contribution, σ_{nt} , which includes effects as turbulence and any other additional broadening process. Following García-Díaz et al. (2008, their equation 2), we use Eq. (19) to express the relationship commented above.

$$\sigma_{\text{obs}}^2 = \sigma_{\text{th}}^2 + \sigma_{\text{fs}}^2 + \sigma_{\text{ins}}^2 + \sigma_{\text{nt}}^2. \quad (19)$$

The thermal contribution of Eq. (19) is the Doppler broadening and depends linearly on the temperature, $\sigma_{\text{th}}^2 = 82.5 T_4/A$ (km/s) 2 , where A is the atomic weight of the emitting ion and $T_4 = T_e/10^4$ (García-Díaz et al. 2008).

In principle, using Eq. (19) we can estimate T_e from the subtraction of the observed widths of H I and [O III] lines. The instrumental width affects the same for both kinds of lines and should be cancelled in the subtraction. García-Díaz et al. (2008) estimated σ_{fs}^2 (H I) = 10.233 (km/s) 2 , finding that σ_{fs}^2 ([O III]) is negligible. On the other hand, σ_{nt}^2 (H I) is not strictly equal to σ_{nt}^2 ([O III]), since the nebular volume occupied by both ions is different. García-Díaz et al.

Figure 14. Observed heliocentric motion of the ions as a function of the ionization potential for the nebular component and the high-velocity ones. Filled and empty symbols represent CELs and RLs, respectively.



(2008), define f as the fraction of the volume of H^+ occupied by O^{2+} and $(1-f)$ the fraction filled by O^+ and other ions with lower degree of ionization, as N^+ . We assume the average value $\langle f \rangle = 0.76$ estimated by García-Díaz et al. (2008) for the Orion Nebula. Using equations 7 to 10 from García-Díaz et al. (2008), we obtain $T_e = 8340 \pm 410$ k for the nebular component. In the case of the shock components, we assume $f = 1.0$ and obtain $T_e = 8670 \pm 50$ K and $T_e = 10474 \pm 790$ K for cuts 2 and 3, respectively.

The resulting T_e values obtained from the observed line widths in the nebular component of cut 2 (representative of the nebular component of the rest of the cuts) and the shock component of the same cut, are in remarkably good agreement with those obtained from the $[\text{O III}]$ line ratios, shown in Table 7. In the case of the shock component of cut 3, the large difference between the values obtained from both methods is due to the contamination by several unresolved velocity components, as it is shown in Fig. 15 and discussed in § 10, that broadens the lines and provides wrong higher temperatures.

10 PROPER MOTIONS OF HH 529 II AND III

The plane-of-sky motions of the bow shocks in HH 529 have been previously reported in Table 3 of O'Dell & Henney (2008) and in sec 3.3.1.3 of O'Dell et al. (2015). However, the reported tangential velocities are very disparate, so we have re-measured the proper motions, using *Hubble Space Telescope* (*HST*) imaging over 20 years as it is described in § 2. The 1995 and 2015 images were aligned to the 2005 ACS image using Astrodrizzle⁵ and rebinned to the ACS pixel scale of 0.05 arcsec. The 2005 image itself has been aligned to the absolute astrometric reference of 2MASS, as painstakingly described in sec 3.3 of Roberto et al. (2013). Proper motions are estimated for the two intervals, 1995–2005 and 2005–2015, using the Fourier Local Correlation Tracking (FLCT) method (Welsch et al. 2004; Fisher & Welsch 2008)⁶ with a kernel width of 10 pixels (0.5 arcsec). For an assumed distance of 417 pc, a shift of 1 pixel in 10 years corresponds to approximately 10 km s^{-1} . A potential disadvantage of using the ACS data in this study is that the F658N ACS filter is relatively broad and includes both $\text{H}\alpha \lambda 6563$ and $[\text{N II}] \lambda 6583$, whereas the WFPC2 and WFC3 F656N filters are narrower and more effectively isolate $\lambda 6563$. Ionization gradients in the nebula can therefore contribute to differences in the images obtained, which would obscure the signal due to the gas motions. However, the degree of ionization in HH 529 III and II is so high that this turns out not to be an issue in this object. Results are presented in Table 23 and Figure 15.

We find that HH 529 III consists of at least two distinct moving structures. The large outer curved bow, which we call III a, is relatively smooth, spanning about 7 arcsec in its brightest part, but with fainter wings (best visible on the ratio image) that extend farther. We cover the bright part of the bow with 5 sample ellipses: a1 to a5, where a3 seems to be the apex of the bow but a2 is the one that falls in the UVES slit. Roughly 0.7 arcsec to the east of III a is a smaller, knottier bow, which we call III b and cover with 3 sample ellipses: b1, b2 and b3. The brightest knot is b2, but it is the b1 sample that falls in the UVES slit. HH 529 II is found to consist of three distinct

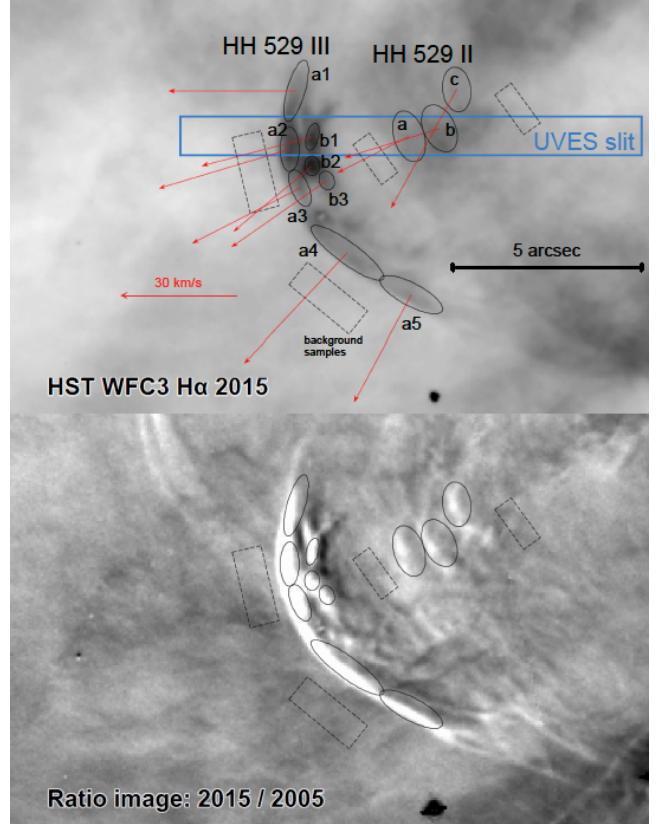


Figure 15. Tangential velocities of shock features in HH 529 II and III derived from 3 epochs of HST imaging. Upper panel shows various discrete features identified in the bow shocks (black ellipses with arrows indicating the average proper motion of each feature). Small dashed rectangles indicate regions where the nebular background brightness was measured and the large blue rectangle shows the position of the spectrograph slit. The background negative grayscale shows an *HST* WFC3 image in the F656N filter from 2015. Lower panel shows the ratio between the 2015 image and an *HST* ACS image in the F658N filter from 2005 (white means brighter in 2015). This highlights the changes in the nebula over that 10-year period, which are principally due to motions of the shocked gas.

bows with separations of order 1 arcsec, which we call II a, II b, and II c, with II a and II b falling in the UVES slit.

10.1 Physical aspects of the high velocity components

From a dynamical point of view, Dyson (1984) shown that the interaction of the outflows from low-mass protostars is isothermal. Moreover, this is the appropriate situation for a shock immersed in a fully ionized medium, where the temperature is defined by the thermal equilibrium of an ionized gas. In this case, the compression of the gas is not limited as in the adiabatic case. Using the total or 3D velocity (v_{tot}) of the shock components within the reference framework of the shock, and the sound speed in an ionized gas c_0 , we can estimate the Mach number M , using Eq. (20) and Eq. (21).

$$M = \frac{|v_{\text{tot}}|}{c_0}, \quad (20)$$

$$c_0 = \sqrt{\frac{\gamma k T}{\mu_0 m_H}}. \quad (21)$$

⁵ <https://drizzlepac.readthedocs.io>

⁶ We used version 1.07 of FLCT, obtained from <http://cgem.ssl.berkeley.edu/cgi-bin/cgem/FLCT/home>, together with version 1.04 of the Python wrapper pyflct, obtained from <https://github.com/PyDL/pyflct>.

Table 23. Proper motions of shock features

Feature	UVES cut	V_t km s $^{-1}$	PA deg	Contrast $S(\text{H}\alpha)/S(\text{H}\alpha, \text{BG})$
(1)	(2)	(3)	(4)	(5)
HH 529 III a1		33 ± 3	90 ± 3	0.46 ± 0.14
HH 529 III a2	3	36 ± 1	107 ± 7	0.82 ± 0.11
HH 529 III a3		32 ± 1	117 ± 3	0.52 ± 0.14
HH 529 III a4		39 ± 2	137 ± 5	0.41 ± 0.07
HH 529 III a5		32 ± 1	152 ± 10	0.27 ± 0.07
HH 529 III b1	3	30 ± 2	105 ± 3	0.95 ± 0.09
HH 529 III b2		27 ± 1	130 ± 1	1.14 ± 0.10
HH 529 III b3		30 ± 2	125 ± 4	0.64 ± 0.07
HH 529 II a	2	21 ± 9	117 ± 58	0.25 ± 0.03
HH 529 II b	2	26 ± 5	107 ± 4	0.35 ± 0.08
HH 529 II c		35 ± 9	151 ± 87	0.22 ± 0.03

COLUMNS: (1) Name of shock feature (see Fig. 15 for positions). (2) Spatial cut of the UVES spectrum where this feature appears, if any. (3) Mean tangential velocity for each feature, weighted by background-subtracted surface brightness, $S(\text{H}\alpha)$, of each pixel. (4) Mean position angle of proper motion, weighted in the same way. (5) Mean relative $\text{H}\alpha$ brightness with respect to nebular background. For columns 3, 4, and 5, the \pm uncertainties correspond to the root-mean-square variation over each sample region and do not include systematic uncertainties, which are of order 2 km s $^{-1}$

In § 9.1, the heliocentric velocities of the different ions were presented for both shocks. Considering the OMC reference framework (~ 28 km s $^{-1}$, Goudis 1982) and the average tangential motion of 35 ± 2 km s $^{-1}$ estimated in § 10 for HH529, we obtain total velocities of -62.60 ± 1.34 km s $^{-1}$ and -66.95 ± 1.09 km s $^{-1}$ for the high velocity component of cut 3 (HH529III) and cut 2 (HH529II) respectively. Considering $T_e = 8400 \pm 150$ K for the nebular component and $\gamma = 1$ (isothermal process), we obtain $c_0 = 11.80 \pm 0.10$ km s $^{-1}$. Thus, assuming that both are external working surfaces, we derive a Mach number of $M = 5.31 \pm 0.12$ and $M = 5.68 \pm 0.10$ for HH529III and HH529II, respectively.

In the case of an isothermal shock, the ratio between the gas densities before (n_{pre}) and after (n_{post}) the shock follows Eq. (22).

$$\frac{n_{\text{post}}}{n_{\text{pre}}} = M^2 \quad (22)$$

Using this value presented in Table 7, we obtain a pre-shock density $n_{\text{pre}} = 1560 \pm 280$ cm $^{-3}$ for HH529III. This value is consistent with densities determined in photoionized areas of the Orion Nebula outside the Huygens region, where the density decreases radially (Mesa-Delgado et al. 2008). This would place HH529III in the foreground of the main ionization front. On the other hand, considering also HH529II an external working surface, we would obtain a pre-shock density $n_{\text{pre}} = 370 \pm 60$ cm $^{-3}$, indicating that HH529II is impacting the ambient gas in a zone more external from where HH529III does. Thus, HH529II would be located well ahead towards the observer. This scenario seems unlikely, considering the similar ionization state of the gas in both HH objects. In addition to this, the multiple velocity components included in HH529III that increase the real dispersion of the velocity with respect to what is observed in HH529II and the fact that HH529III is denser than HH529II almost a factor 4 (see § 4), evidence that HH529II can correspond to an "internal working surface" (Masciadri & Raga 2001) of the jet beam. This internal shock may have its origin in a somewhat later ejection of material from the common origin of HH529 (located at the star COUP 666 by O'Dell et al. 2015), flow-

ing along the jet beam opened by the main shock front (HH529III). This scenario has been studied in detail by Raga & Reipurth (2004) for HH jets emerging from a neutral cloud into an H II region.

In both high-velocity components, it is noticeable the absence of [OI] (see Fig. 2) and the weakness of lines of low ionization potential ions. This proves that HH529II and HH529III are objects fully photoionized and do not contain a trapped ionization front (Masciadri & Raga 2001), contrary to what was found by Mesa-Delgado et al. (2009) for HH202S. Due to the fact that HH529 is fully photoionized, we can assure that the entire jet beam inside the HII region is observable in optical emission lines, contrary to partially ionized or neutral Herbig-Haro objects, where only limited regions can be observed (Raga et al. 2000a,b). Considering the velocity flow angle with respect the sky plane of $\sim 62^\circ$ estimated in this work for the HH529 system, the observed spectra of the high-velocity components should integrate the emission along an important fraction of the ionized jet beam, including the compressed gas in the leading working surface and the gas of the jet beam behind.

In § 8.1.4, we have observed an increase in the gaseous proportion of Fe in the high-velocity components with respect to the values found in the nebular gas. Taking the solar value of Fe/O = -1.28 ± 0.08 compiled by Lodders (2019), the percentage of Fe in the gaseous phase is around 6% in the nebular components while for HH529 is around 14%. In the case of HH202S, Mesa-Delgado et al. (2009) found that this proportion is around 44%. These results are consistent with theoretical studies predicting that fast shocks are effective destroying dust grains (see Jones et al. 1994; Mouri & Taniguchi 2000, and references therein).

However, this also indicate that most of the Fe is still depleted into dust grains in the shocks associated with these HH objects. Another evidence of surviving dust is the detection of thermal dust mid-IR emission at 11.7 μm coincident with both HH529II and III as well as HH202S (Smith et al. 2005). Those authors find that the dust emission is seen behind the shocks or density enhancements within the body of the jet beam, indicating that the dust is either heated by radiation coming from $\theta^1\text{Ori C}$ or locally by trapped Ly α emission from the high-density zones behind the shocks. A key factor is determining observationally the relationship between the level of depletion of Fe and some particular characteristic of each HH, such as its 3D velocity. For now, the results of HH529 and HH202 seem to indicate that the fraction of gaseous Fe in the shock front grows proportional to the velocity of the HH. However, we need more objects to establish a clear relationship. This will be revealed by including other photoionized Herbig-Haro objects, whose analysis we have in preparation.

11 SUMMARY AND CONCLUSIONS

ACKNOWLEDGEMENTS

We acknowledge support from the State Research Agency (AEI) of the Spanish Ministry of Science, Innovation and Universities (MCIU) and the European Regional Development Fund (FEDER) under grants AYA2015-65205-P and AYA2017-83383-P. JGR acknowledges support from an Advanced Fellowship from the Severo Ochoa excellence program (SEV-2015-0548). KZA-C acknowledges support from Mexican CONACYT posdoctoral grant 364239. The authors acknowledge support under grant P/308614 financed by funds transferred from the Spanish Ministry of Science, Innovation and Universities, charged to the General State Budgets and with funds transferred from the General Budgets of the Autonomous Community of the Canary Islands by the MCIU.

REFERENCES

- Arellano-Córdova K. Z., Esteban C., García-Rojas J., Méndez-Delgado J. E., 2020, *MNRAS*, **496**, 1051
- Astropy Collaboration et al., 2013, *A&A*, **558**, A33
- Aver E., Olive K. A., Skillman E. D., 2011, *J. Cosmology Astropart. Phys.*, **2011**, 043
- Baldwin J. A., et al., 1996, *ApJ*, **468**, L115
- Ballester P., Modigliani A., Boitquin O., Cristiani S., Hanuschik R., Kaufer A., Wolf S., 2000, *The Messenger*, **101**, 31
- Bally J., Reipurth B., 2018, *Research Notes of the American Astronomical Society*, **2**, 46
- Bally J., Sutherland R. S., Devine D., Johnstone D., 1998, *AJ*, **116**, 293
- Bally J., O'Dell C. R., McCaughrean M. J., 2000, *AJ*, **119**, 2919
- Bastin R. J., Storey P. J., 2006, in Barlow M. J., Méndez R. H., eds, IAU Symposium Vol. 234, Planetary Nebulae in our Galaxy and Beyond. pp 369–370, doi:10.1017/S1743921306003280
- Bautista M. A., 2001, *A&A*, **365**, 268
- Benjamin R. A., Skillman E. D., Smits D. P., 2002, *ApJ*, **569**, 288
- Berg D. A., Erb D. K., Henry R. B. C., Skillman E. D., McQuinn K. B. W., 2019, *ApJ*, **874**, 93
- Berg D. A., Pogge R. W., Skillman E. D., Croxall K. V., Moustakas J., Rogers N. S. J., Sun J., 2020, *ApJ*, **893**, 96
- Blagrade K. P. M., Martin P. G., Baldwin J. A., 2006, *ApJ*, **644**, 1006
- Blagrade K. P. M., Martin P. G., Rubin R. H., Dufour R. J., Baldwin J. A., Hester J. J., Walter D. K., 2007, *ApJ*, **655**, 299
- Bohigas J., 2015, *MNRAS*, **453**, 1281
- Bowen I. S., 1955, *ApJ*, **121**, 306
- Brown R. L., Mathews W. G., 1970, *ApJ*, **160**, 939
- Butler K., Zeippen C. J., 1989, *A&A*, **208**, 337
- D'Odorico S., Cristiani S., Dekker H., Hill V., Kaufer A., Kim T., Primas F., 2000, Performance of UVES, the echelle spectrograph for the ESO VLT and highlights of the first observations of stars and quasars. pp 121–130, doi:10.1111/12.390133
- Davey A. R., Storey P. J., Kisielius R., 2000, *A&AS*, **142**, 85
- Delgado-Inglada G., Morisset C., Stasińska G., 2014, *MNRAS*, **440**, 536
- Delgado-Inglada G., Mesa-Delgado A., García-Rojas J., Rodríguez M., Esteban C., 2016, *MNRAS*, **456**, 3855
- Domínguez-Guzmán G., Rodríguez M., Esteban C., García-Rojas J., 2019, arXiv e-prints, p. arXiv:1906.02102
- Dyson J. E., 1984, *Ap&SS*, **106**, 181
- Ellis D. G., Martinson I., 1984, *Phys. Scr.*, **30**, 255
- Espíritu J. N., Peimbert A., Delgado-Inglada G., Ruiz M. T., 2017, *Rev. Mex. Astron. Astrofís.*, **53**, 95
- Esteban C., Peimbert M., 1999, *A&A*, **349**, 276
- Esteban C., Peimbert M., Torres-Peimbert S., Escalante V., 1998, *MNRAS*, **295**, 401
- Esteban C., Peimbert M., García-Rojas J., Ruiz M. T., Peimbert A., Rodríguez M., 2004, *MNRAS*, **355**, 229
- Fang X., Liu X. W., 2011, *MNRAS*, **415**, 181
- Fang X., Liu X. W., 2013, *MNRAS*, **429**, 2791
- Fehrenbach C., 1977, *A&AS*, **29**, 71
- Ferland G. J., 2001, *PASP*, **113**, 41
- Ferland G. J., Henney W. J., O'Dell C. R., Porter R. L., van Hoof P. A. M., Williams R. J. R., 2012, *ApJ*, **757**, 79
- Feuchtgruber H., et al., 1997, *ApJ*, **487**, 962
- Fisher G. H., Welsch B. T., 2008, in Howe R., Komm R. W., Balasubramanian K. S., Petrie G. J. D., eds, Astronomical Society of the Pacific Conference Series Vol. 383, Subsurface and Atmospheric Influences on Solar Activity. p. 373 (arXiv:0712.4289)
- Fritzsche S., Fricke B., Geschke D., Heitmann A., Sienkiewicz J. E., 1999, *ApJ*, **518**, 994
- Froese Fischer C., Tachiev G., 2004, *Atomic Data and Nuclear Data Tables*, **87**, 1
- Froese Fischer C., Rubin R. H., Rodríguez M., 2008, *MNRAS*, **391**, 1828
- Galavis M. E., Mendoza C., Zeippen C. J., 1995, *A&AS*, **111**, 347
- García-Díaz M. T., Henney W. J., López J. A., Doi T., 2008, *Rev. Mex. Astron. Astrofís.*, **44**, 181
- García-Rojas J., Esteban C., 2007, *ApJ*, **670**, 457
- García-Rojas J., Esteban C., Peimbert M., Rodríguez M., Ruiz M. T., Peimbert A., 2004, *ApJS*, **153**, 501
- García-Rojas J., Esteban C., Peimbert A., Peimbert M., Rodríguez M., Ruiz M. T., 2005, *MNRAS*, **362**, 301
- García-Rojas J., Esteban C., Peimbert A., Rodríguez M., Peimbert M., Ruiz M. T., 2007, *Rev. Mex. Astron. Astrofís.*, **43**, 3
- García-Rojas J., Peña M., Morisset C., Delgado-Inglada G., Mesa-Delgado A., Ruiz M. T., 2013, *A&A*, **558**, A122
- García-Rojas J., Madonna S., Luridiana V., Sterling N. C., Morisset C., Delgado-Inglada G., Toribio San Cipriano L., 2015, *MNRAS*, **452**, 2606
- Goudis C., 1982, The Orion complex: A case study of interstellar matter. Vol. 90, doi:10.1007/978-94-009-7712-9,
- Grieve M. F. R., Ramsbottom C. A., Hudson C. E., Keenan F. P., 2014, *ApJ*, **780**, 110
- Izotov Y. I., Stasińska G., Meynet G., Guseva N. G., Thuan T. X., 2006, *A&A*, **448**, 955
- Johansson S., Zethson T., Hartman H., Ekberg J. O., Ishibashi K., Davidson K., Gull T., 2000, *A&A*, **361**, 977
- Jones A. P., Tielens A. G. G. M., Hollenbach D. J., McKee C. F., 1994, *ApJ*, **433**, 797
- Kaler J. B., 1967, *ApJ*, **148**, 925
- Kaufman V., Martin W. C., 1993, *Journal of Physical and Chemical Reference Data*, **22**, 279
- Kaufman V., Sugar J., 1986, *Journal of Physical and Chemical Reference Data*, **15**, 321
- Kingdon J. B., Ferland G. J., 1995, *ApJ*, **450**, 691
- Kisielius R., Storey P. J., Davey A. R., Neale L. T., 1998, *A&AS*, **133**, 257
- Kisielius R., Storey P. J., Ferland G. J., Keenan F. P., 2009, *MNRAS*, **397**, 903
- Kunth D., Sargent W. L. W., 1983, *ApJ*, **273**, 81
- Liu X. W., Storey P. J., Barlow M. J., Danziger I. J., Cohen M., Bryce M., 2000, *MNRAS*, **312**, 585
- Liu X. W., Luo S. G., Barlow M. J., Danziger I. J., Storey P. J., 2001, *MNRAS*, **327**, 141
- Lodders K., 2019, arXiv e-prints, p. arXiv:1912.00844
- Lucy L. B., 1995, *A&A*, **294**, 555
- Luridiana V., Morisset C., Shaw R. A., 2015, *A&A*, **573**, A42
- Masciadri E., Raga A. C., 2001, *A&A*, **376**, 1073
- McLaughlin B. M., Lee T.-G., Ludlow J. A., Land i E., Loch S. D., Pindzola M. S., Ballance C. P., 2011, *Journal of Physics B Atomic Molecular Physics*, **44**, 175206
- McNabb I. A., Fang X., Liu X. W., Bastin R. J., Storey P. J., 2013, *MNRAS*, **428**, 3443
- Méndez-Delgado J. E., Esteban C., García-Rojas J., Arellano-Córdova K. Z., Valeri M., 2020, *MNRAS*, **496**, 2726
- Mendoza C., 1983, in Aller L. H., ed., IAU Symposium Vol. 103, Planetary Nebulae. pp 143–172
- Mendoza C., Zeippen C. J., 1982a, *MNRAS*, **198**, 127
- Mendoza C., Zeippen C. J., 1982b, *MNRAS*, **199**, 1025
- Mendoza C., Zeippen C. J., 1983, *MNRAS*, **202**, 981
- Mesa-Delgado A., Esteban C., García-Rojas J., 2008, *ApJ*, **675**, 389
- Mesa-Delgado A., Esteban C., García-Rojas J., Luridiana V., Bautista M., Rodríguez M., López-Martín L., Peimbert M., 2009, *MNRAS*, **395**, 855
- Moehler S., Dreizler S., LeBlanc F., Khalack V., Michaud G., Richer J., Sweigart A. V., Grundahl F., 2014a, *A&A*, **565**, A100
- Moehler S., et al., 2014b, *A&A*, **568**, A9
- Mouri H., Taniguchi Y., 2000, *ApJ*, **534**, L63
- Nicholls D. C., Dopita M. A., Sutherland R. S., 2012, *ApJ*, **752**, 148
- Noll S., Kausch W., Barden M., Jones A. M., Szyszka C., Kimeswenger S., Vinther J., 2012, *A&A*, **543**, A92
- O'Dell C. R., 2001, *ARA&A*, **39**, 99
- O'Dell C. R., 2018, *MNRAS*, **478**, 1017
- O'Dell C. R., Henney W. J., 2008, *AJ*, **136**, 1566
- O'Dell C. R., Wen Z., 1992, *ApJ*, **387**, 229
- O'Dell C. R., Ferland G. J., Henney W. J., Peimbert M., García-Díaz M. T., Rubin R. H., 2015, *ApJ*, **150**, 108

- O'Dell C. R., Abel N. P., Ferland G. J., 2020, *ApJ*, **891**, 46
- Olive K. A., Skillman E. D., 2004, *ApJ*, **617**, 29
- Osterbrock D. E., Ferland G. J., 2006, Astrophysics of gaseous nebulae and active galactic nuclei
- Osterbrock D. E., Tran H. D., Veilleux S., 1992, *ApJ*, **389**, 305
- Pagel B. E. J., Simonson E. A., Terlevich R. J., Edmunds M. G., 1992, *MNRAS*, **255**, 325
- Peimbert M., 1967, *ApJ*, **150**, 825
- Peimbert A., 2003, *ApJ*, **584**, 735
- Peimbert M., Costero R., 1969, Boletin de los Observatorios Tonantzintla y Tacubaya, **5**, 3
- Peimbert A., Peimbert M., 2013, *ApJ*, **778**, 89
- Peimbert A., Peimbert M., Luridiana V., 2002, *ApJ*, **565**, 668
- Péquignot D., Petitjean P., Boisson C., 1991, *A&A*, **251**, 680
- Péquignot D., Amara M., Liu X. W., Barlow M. J., Storey P. J., Morisset C., Torres-Peimbert S., Peimbert M., 2002, in Henney W. J., Franco J., Martos M., eds, Revista Mexicana de Astronomia y Astrofisica Conference Series Vol. 12, Revista Mexicana de Astronomia y Astrofisica Conference Series. pp 142–143
- Persson W., Wahlström C.-G., Jönsson L., Di Rocco H. O., 1991, *Phys. Rev. A*, **43**, 4791
- Podobedova L. I., Kelleher D. E., Wiese W. L., 2009, Journal of Physical and Chemical Reference Data, **38**, 171
- Porter R. L., Ferland G. J., MacAdam K. B., 2007, *ApJ*, **657**, 327
- Porter R. L., Ferland G. J., Storey P. J., Detisch M. J., 2012, *MNRAS*, **425**, L28
- Porter R. L., Ferland G. J., Storey P. J., Detisch M. J., 2013, *MNRAS*, **433**, L89
- Price-Whelan A. M., et al., 2018, *AJ*, **156**, 123
- Quinet P., 1996, *A&AS*, **116**, 573
- Raga A. C., Reipurth B., 2004, Rev. Mex. Astron. Astrofis., **40**, 15
- Raga A. C., López-Martín J., López J. A., Meaburn J., 2000a, in Arthur S. J., Brickhouse N. S., Franco J., eds, Revista Mexicana de Astronomia y Astrofisica Conference Series Vol. 9, Revista Mexicana de Astronomia y Astrofisica Conference Series. pp 191–193
- Raga A., et al., 2000b, *MNRAS*, **314**, 681
- Ramsbottom C. A., Bell K. L., 1997, *Atomic Data and Nuclear Data Tables*, **66**, 65
- Roberto M., et al., 2013, *ApJS*, **207**, 10
- Rodríguez M., 1999, *A&A*, **348**, 222
- Rodríguez M., 2002, *A&A*, **389**, 556
- Rodríguez M., 2020, *MNRAS*, **495**, 1016
- Rodríguez M., Rubin R. H., 2005, *ApJ*, **626**, 900
- Simón-Díaz S., Stasińska G., 2011, *A&A*, **526**, A48
- Smith N., Bally J., Shuping R. Y., Morris M., Kassis M., 2005, *AJ*, **130**, 1763
- Stasińska G., 1978, *A&A*, **66**, 257
- Stasińska G., Tenorio-Tagle G., Rodríguez M., Henney W. J., 2007, *A&A*, **471**, 193
- Storey P. J., 1994, *A&A*, **282**, 999
- Storey P. J., Hummer D. G., 1995, *MNRAS*, **272**, 41
- Storey P. J., Zeippen C. J., 2000, *MNRAS*, **312**, 813
- Storey P. J., Sochi T., Badnell N. R., 2014, *MNRAS*, **441**, 3028
- Storey P. J., Sochi T., Bastin R., 2017, *MNRAS*, **470**, 379
- Sugar J., Corliss C., 1985, Atomic energy levels of the iron-period elements: Potassium through Nickel
- Tayal S. S., 2004, *A&A*, **418**, 363
- Tayal S. S., 2011, *ApJS*, **195**, 12
- Tayal S. S., Zatsariny O., 2010, *ApJS*, **188**, 32
- Tody D., 1993, IRAF in the Nineties. p. 173
- Torres-Peimbert S., Peimbert M., Daltabuit E., 1980, *ApJ*, **238**, 133
- Tsamis Y. G., Walsh J. R., Vilchez J. M., Péquignot D., 2011, *MNRAS*, **412**, 1367
- Van Hoof P. A. M., 2018, *Galaxies*, **6**
- Verner E. M., Verner D. A., Baldwin J. A., Ferland G. J., Martin P. G., 2000, *ApJ*, **543**, 831
- Vilchez J. M., Pagel B. E. J., 1988, *MNRAS*, **231**, 257
- Walter D. K., Dufour R. J., Hester J. J., 1992, *ApJ*, **397**, 196
- Welsch B. T., Fisher G. H., Abbott W. P., Regnier S., 2004, *ApJ*, **610**, 1148
- Wesson R., Jones D., García-Rojas J., Boffin H. M. J., Corradi R. L. M., 2018, *MNRAS*, **480**, 4589
- Wiese W. L., Fuhr J. R., Deters T. M., 1996, Journal of Physical and Chemical Reference Data, Monograph 7, 403
- Yuan H. B., Liu X. W., Péquignot D., Rubin R. H., Ercolano B., Zhang Y., 2011, *MNRAS*, **411**, 1035
- Zhang Y., Liu X. W., 2006, in Barlow M. J., Méndez R. H., eds, IAU Symposium Vol. 234, Planetary Nebulae in our Galaxy and Beyond. pp 547–548 ([arXiv:astro-ph/0605180](https://arxiv.org/abs/astro-ph/0605180)), doi:10.1017/S1743921306004170
- Zhang H. L., Pradhan A. K., 1997, *A&AS*, **126**, 373
- Zhang, Hong Lin 1996, *Astron. Astrophys. Suppl. Ser.*, **119**, 523
- Zhang Y., Liu X. W., Liu Y., Rubin R. H., 2005, *MNRAS*, **358**, 457

Table A1. Slope and intercept for Eq. 4 for a range of densities.

$n_e \left(\text{cm}^{-3} \right)$	α	β
100	92984	-7455
500	81830	-6031
1000	77896	-5527
2000	69126	-4378
3000	65040	-3851
4000	62517	-3529
5000	60744	-3305
6000	59402	-3137
7000	58334	-3004
8000	57456	-2895
9000	56715	-2804
10000	56077	-2726
12000	55637	-2676
15000	55087	-2611
20000	54364	-2523
25000	53796	-2452
30000	53329	-2392
40000	52591	-2297
45000	52289	-2257
50000	52019	-2222

APPENDIX A: SOME EXTRA MATERIAL

J: In this appendix we show some of the Tables and Figures of the paper. Bla bla bla

This paper has been typeset from a $\text{\TeX}/\text{\LaTeX}$ file prepared by the author.

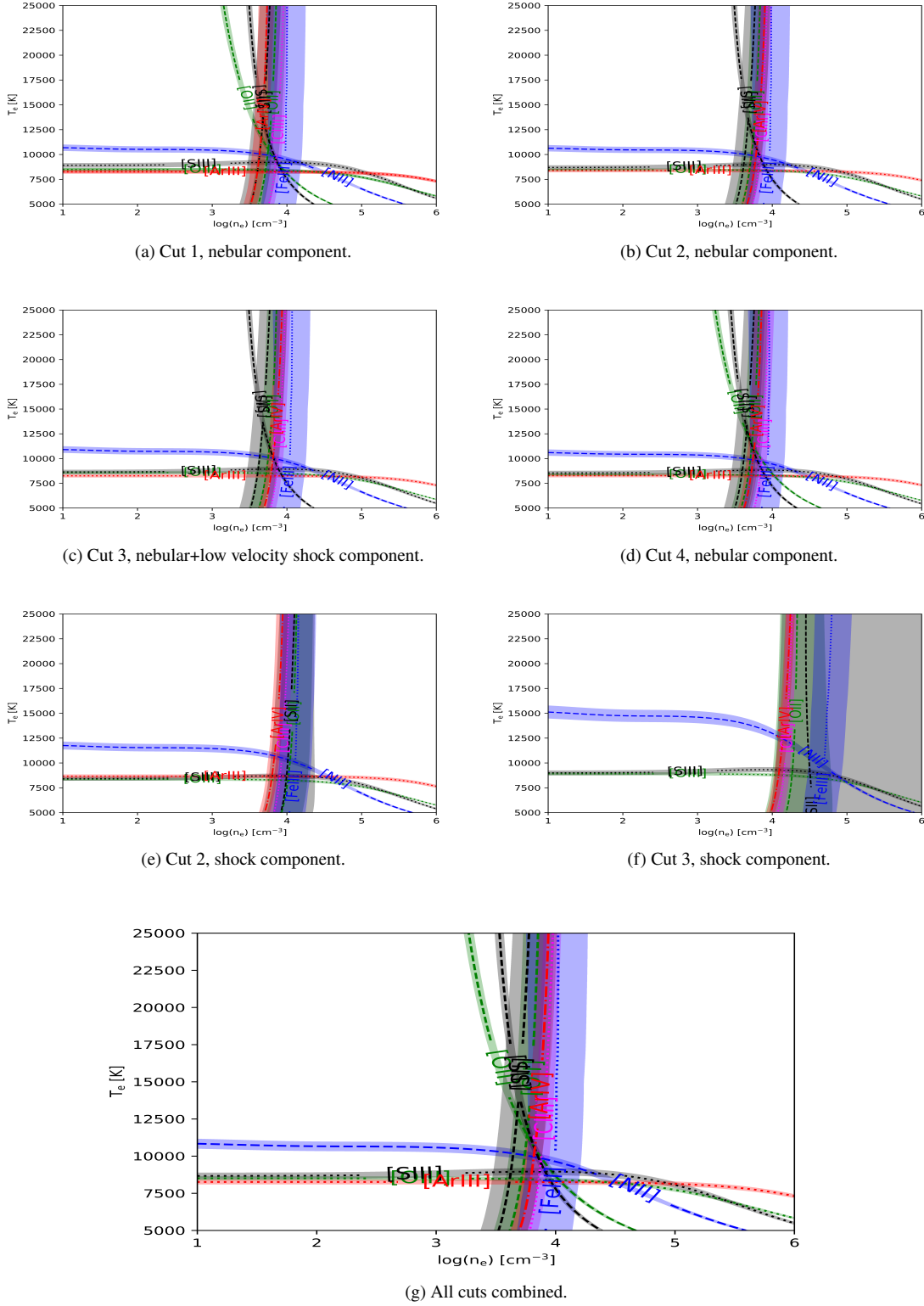
Figure A1. Plasma diagnostic plots for the different cuts and components in the spectra of HH 529 III.

Table A2. Fe²⁺ abundances based on T_e (low).

λ	Cut 1		Cut 2		Cut 3		Cut 4	Combined cuts
	Nebula	Shock	Nebula	Shock	Nebula	Nebula	Nebula	
4658	5.51 ± 0.02	5.59 ^{+0.08} _{-0.06}	5.56 ^{+0.04} _{-0.03}	5.49 ^{+0.11} _{-0.08}	5.51 ± 0.04	5.47 ^{+0.05} _{-0.04}	5.52 ± 0.03	
4702	5.51 ± 0.02	5.59 ^{+0.08} _{-0.07}	5.56 ^{+0.04} _{-0.03}	5.50 ^{+0.12} _{-0.08}	5.52 ± 0.04	5.47 ^{+0.05} _{-0.04}	5.52 ^{+0.04} _{-0.03}	
4734	5.48 ± 0.03	5.58 ^{+0.09} _{-0.07}	5.56 ± 0.04	5.61 ^{+0.13} _{-0.09}	5.50 ^{+0.05} _{-0.04}	5.47 ^{+0.05} _{-0.04}	5.52 ± 0.04	
4755	5.51 ^{+0.03} _{-0.02}	5.61 ^{+0.09} _{-0.07}	5.58 ^{+0.04} _{-0.03}	5.56 ^{+0.12} _{-0.09}	5.52 ^{+0.05} _{-0.04}	5.49 ^{+0.05} _{-0.04}	5.54 ^{+0.04} _{-0.03}	
4770	5.51 ± 0.03	5.63 ^{+0.09} _{-0.07}	5.59 ± 0.04	5.62 ^{+0.12} _{-0.09}	5.55 ^{+0.05} _{-0.04}	5.48 ^{+0.05} _{-0.04}	5.56 ^{+0.04} _{-0.03}	
4778	5.51 ± 0.04	5.75 ^{+0.09} _{-0.07}	5.59 ± 0.04	5.46 ^{+0.16} _{-0.11}	5.51 ^{+0.05} _{-0.04}	5.42 ^{+0.06} _{-0.05}	5.55 ± 0.04	
4881	5.53 ± 0.02	5.61 ^{+0.09} _{-0.06}	5.58 ^{+0.04} _{-0.03}	5.55 ^{+0.12} _{-0.09}	5.53 ± 0.04	5.49 ^{+0.05} _{-0.04}	5.54 ± 0.03	
5011	5.52 ± 0.04	5.78 ^{+0.08} _{-0.07}	5.56 ± 0.04	5.66 ^{+0.12} _{-0.09}	5.51 ^{+0.05} _{-0.04}	5.51 ^{+0.06} _{-0.05}	5.57 ± 0.04	
5271	5.55 ± 0.02	5.61 ^{+0.08} _{-0.06}	5.58 ^{+0.04} _{-0.03}	5.53 ^{+0.11} _{-0.08}	5.55 ± 0.04	5.52 ± 0.04	5.55 ± 0.03	
5412	5.57 ^{+0.06} _{-0.05}	5.68 ^{+0.10} _{-0.08}	5.60 ^{+0.05} _{-0.04}	-	5.57 ^{+0.05} _{-0.04}	5.58 ^{+0.07} _{-0.06}	5.56 ± 0.05	
8838	5.37 ^{+0.11} _{-0.10}	5.41 ^{+0.19} _{-0.15}	5.48 ^{+0.08} _{-0.07}	-	5.34 ^{+0.09} _{-0.08}	5.47 ^{+0.11} _{-0.09}	5.34 ^{+0.09} _{-0.08}	
Weighted Average	5.52 ± 0.03	5.62 ± 0.07	5.57 ± 0.02	5.54 ± 0.06	5.52 ± 0.04	5.48 ± 0.03	5.53 ± 0.04	

Table A3. Fe²⁺ abundances based on T_e (high).

λ	Cut 1		Cut 2		Cut 3		Cut 4	Combined cuts
	Nebula	Shock	Nebula	Shock	Nebula	Nebula	Nebula	
4658	5.77 ^{+0.05} _{-0.04}	5.92 ^{+0.03} _{-0.02}	5.81 ± 0.03	5.75 ± 0.02	5.78 ± 0.03	5.75 ± 0.03	5.79 ± 0.03	
4702	5.76 ^{+0.05} _{-0.04}	5.92 ± 0.03	5.80 ± 0.03	5.75 ^{+0.04} _{-0.03}	5.78 ± 0.03	5.74 ± 0.03	5.79 ^{+0.04} _{-0.03}	
4734	5.74 ^{+0.05} _{-0.04}	5.91 ^{+0.04} _{-0.03}	5.81 ^{+0.04} _{-0.03}	5.87 ^{+0.06} _{-0.05}	5.77 ^{+0.04} _{-0.03}	5.75 ^{+0.04} _{-0.03}	5.79 ± 0.04	
4755	5.76 ^{+0.05} _{-0.04}	5.94 ± 0.03	5.83 ± 0.03	5.82 ± 0.05	5.79 ± 0.03	5.76 ± 0.03	5.81 ± 0.03	
4770	5.76 ^{+0.05} _{-0.04}	5.96 ± 0.03	5.84 ± 0.03	5.87 ± 0.05	5.81 ^{+0.04} _{-0.03}	5.75 ^{+0.04} _{-0.03}	5.82 ^{+0.04} _{-0.03}	
4778	5.76 ^{+0.06} _{-0.05}	6.08 ± 0.04	5.84 ^{+0.04} _{-0.03}	5.72 ± 0.09	5.78 ^{+0.04} _{-0.03}	5.70 ^{+0.05} _{-0.04}	5.82 ± 0.04	
4881	5.79 ± 0.04	5.94 ± 0.03	5.83 ± 0.03	5.80 ± 0.04	5.79 ± 0.03	5.76 ± 0.03	5.80 ± 0.03	
5011	5.76 ^{+0.06} _{-0.05}	6.09 ± 0.04	5.79 ± 0.03	5.90 ^{+0.07} _{-0.06}	5.76 ± 0.03	5.77 ^{+0.05} _{-0.04}	5.82 ± 0.04	
5271	5.77 ± 0.04	5.91 ± 0.03	5.81 ± 0.03	5.76 ^{+0.04} _{-0.03}	5.79 ± 0.03	5.77 ± 0.03	5.79 ± 0.03	
5412	5.80 ^{+0.07} _{-0.06}	5.97 ^{+0.07} _{-0.06}	5.83 ± 0.04	-	5.81 ± 0.04	5.83 ± 0.06	5.80 ± 0.05	
8838	5.73 ^{+0.12} _{-0.11}	5.87 ± 0.13	5.83 ^{+0.07} _{-0.06}	-	5.72 ^{+0.08} _{-0.07}	5.86 ± 0.09	5.72 ^{+0.09} _{-0.08}	
Weighted Average	5.77 ± 0.02	5.94 ± 0.05	5.82 ± 0.02	5.78 ± 0.05	5.78 ± 0.02	5.76 ± 0.03	5.80 ± 0.02	

Table A4. Cl²⁺ and Cl abundances and Cl/O ratio using T_e (low), T_e ([S III]) and T_e (high).

Cut	Component	O ²⁺ /O	Cl ²⁺ /H ⁺	T_e (low)		T_e ([S III])		T_e (high)		
		Cl/H	Cl/O	Cl ²⁺ /H ⁺	Cl/H	Cl/O	Cl ²⁺ /H ⁺	Cl/H	Cl/O	
1	Nebular	0.73 ± 0.04	4.78 ± 0.02	4.83 ± 0.02	-3.63 ± 0.03	4.88 ^{+0.06} _{-0.05}	4.92 ± 0.06	-3.53 ± 0.07	5.01 ± 0.03	5.04 ± 0.03
2	Shock	0.94 ± 0.04	4.80 ^{+0.08} _{-0.06}	4.83 ± 0.07	-3.74 ± 0.07	5.01 ^{+0.05} _{-0.04}	5.03 ± 0.05	-3.54 ± 0.05	5.08 ± 0.03	5.10 ± 0.03
2	Nebular	0.77 ± 0.05	4.81 ^{+0.04} _{-0.03}	4.86 ± 0.04	-3.61 ± 0.06	4.93 ^{+0.06} _{-0.05}	4.97 ± 0.06	-3.49 ± 0.07	5.03 ± 0.03	5.06 ± 0.03
3	Shock	0.83 ± 0.05	4.94 ^{+0.10} _{-0.08}	4.96 ± 0.08	-3.63 ± 0.09	5.09 ^{+0.06} _{-0.05}	5.11 ± 0.06	-3.48 ± 0.07	5.16 ± 0.04	5.17 ± 0.04
3	Low velocity shock+nebula	0.79 ± 0.05	4.80 ^{+0.04} _{-0.03}	4.85 ± 0.04	-3.60 ± 0.06	4.96 ^{+0.06} _{-0.05}	4.99 ± 0.06	-3.46 ± 0.07	5.03 ^{+0.03} _{-0.02}	5.06 ± 0.03
4	Nebular	0.78 ± 0.05	4.79 ± 0.04	4.85 ± 0.04	-3.62 ± 0.06	4.95 ^{+0.05} _{-0.04}	4.99 ± 0.06	-3.48 ± 0.07	5.03 ± 0.03	5.06 ± 0.03
-	Combined cuts	0.81 ± 0.05	4.79 ± 0.03	4.84 ± 0.03	-3.62 ± 0.05	4.94 ^{+0.05} _{-0.04}	4.97 ± 0.05	-3.50 ± 0.06	5.02 ± 0.03	5.05 ± 0.03

Table A5. Ni²⁺ abundances per line.

λ	Cut 1		Cut 2		Cut 3		Cut 4		Combined cuts
	Nebula	Shock	Nebula	Shock	Nebula	Nebula	Nebula	Nebula	
6000	4.52 ± 0.08	4.42 ^{+0.13} _{-0.11}	4.34 ^{+0.07} _{-0.06}	-	4.40 ± 0.07	4.42 ^{+0.10} _{-0.09}	4.35 ± 0.08		
6534	4.22 ^{+0.10} _{-0.11}	4.61:	4.19 ± 0.06	4.44:	4.16 ± 0.07	4.18 ± 0.11	4.26 ± 0.07		
6682	4.76 ^{+0.14} _{-0.13}	-	4.70 ^{+0.14} _{-0.13}	-	4.44 ^{+0.14} _{-0.13}	-	-		
6797	4.50 ^{+0.23} _{-0.22}	4.94:	4.79 ± 0.08	-	4.77 ± 0.10	4.81:	4.77 ± 0.14		
6946	3.94 ^{+0.26} _{-0.23}	4.75 ^{+0.19} _{-0.17}	4.23 ± 0.11	4.50:	4.21 ± 0.11	4.23 ^{+0.15} _{-0.14}	4.31:		
7890	4.42 ± 0.04	4.52 ^{+0.08} _{-0.06}	4.49 ± 0.04	4.39 ^{+0.12} _{-0.10}	4.45 ^{+0.05} _{-0.04}	4.45 ^{+0.05} _{-0.04}	4.46 ± 0.04		
Weighted Average	4.37 ± 0.14	4.50 ± 0.08	4.33 ± 0.17	4.39^{+0.12}_{-0.10}	4.32 ± 0.16	4.36 ± 0.12	4.38 ± 0.10		

Table A6. Values of t^2 estimated for each component, based on the combination of Eq.(12) with Eq.(13), Eq.(14) and Eq.(15).

Cut	Component	$t^2(\text{O}^{2+})$	$t^2(\text{S}^{2+})$	$t^2(\text{N}^+)$
1	Nebular	0.004 ± 0.012	0.040 ± 0.026	0.053 ± 0.018
2	Shock	0.025 ± 0.013	0.062 ± 0.026	0.095 ± 0.024
2	Nebular	0.008 ± 0.012	0.039 ± 0.025	0.058 ± 0.018
3	Shock	0.027 ± 0.017	0.068 ± 0.033	0.087 ± 0.033
3	Low velocity shock+nebula	0.010 ± 0.013	0.036 ± 0.026	0.064 ± 0.019
4	Nebular	0.022 ± 0.014	0.062 ± 0.027	0.079 ± 0.020

Table A7. Average velocities and FWHM for the observed ions for selected cuts and components.

Ion	I.P. (eV)	Nebular Cut 2		Shock Cut 2		Shock Cut 3	
		$\langle V \rangle$ (Km s $^{-1}$)	$\langle \text{FWHM} \rangle$ (Km s $^{-1}$)	$\langle V \rangle$ (Km s $^{-1}$)	$\langle \text{FWHM} \rangle$ (Km s $^{-1}$)	$\langle V \rangle$ (Km s $^{-1}$)	$\langle \text{FWHM} \rangle$ (Km s $^{-1}$)
[O I]	0.00	28.80 ± 0.03 (2)	11.80 ± 0.02 (2)	-	-	-	-
[C I]	0.00	28.70 ± 0.03 (3)	9.49 ± 0.10 (3)	-	-	-	-
[N I]	0.00	30.25 ± 0.64 (3)	9.51 ± 0.60 (3)	-	-	-	-
[Cr II]	6.77	28.28 ± 2.66 (5)	9.71 ± 1.19 (5)	-26.50 ± 1.00 (1)	25.60 ± 1.00 (1)	-27.20 ± 1.00 (1)	39.40 ± 1.00 (1)
[Ni II]	7.64	30.20 ± 0.08 (10)	11.75 ± 0.63 (10)	-30.20 ± 6.09 (3)	15.81 ± 2.83 (3)	-	-
[Fe II]	7.90	27.33 ± 1.36 (34)	11.84 ± 2.29 (34)	-28.76 ± 1.21 (2)	13.66 ± 0.97 (2)	-	-
[S II]	10.36	23.10 ± 0.86 (4)	21.52 ± 0.90 (4)	-27.80 ± 0.03 (4)	16.29 ± 0.45 (4)	-21.94 ± 1.46 (6)	22.92 ± 1.00 (6)
[Cl III]	12.97	24.80 ± 1.00 (1)	20.40 ± 1.00 (1)	-23.80 ± 1.00 (1)	18.90 ± 1.00 (1)	-	-
H I	13.60	16.39 ± 0.78 (51)	24.95 ± 0.16 (51)	-29.08 ± 0.36 (51)	27.20 ± 0.01 (51)	-23.90 ± 0.89 (45)	33.12 ± 0.44 (45)
[O II]	13.62	17.85 ± 1.65 (2)	18.69 ± 0.69 (2)	-28.40 ± 1.20 (2)	20.04 ± 1.10 (2)	-21.60 ± 0.03 (2)	25.27 ± 0.53 (2)
O I	13.62	18.73 ± 0.50 (3)	23.29 ± 0.86 (3)	-	-	-	-
[N II]	14.53	20.67 ± 0.95 (4)	19.45 ± 0.05 (4)	-28.70 ± 0.80 (4)	18.13 ± 0.45 (4)	-19.75 ± 1.05 (3)	25.98 ± 0.19 (3)
[Fe III]	16.19	13.83 ± 1.09 (21)	12.10 ± 0.32 (21)	-31.90 ± 0.02 (17)	13.56 ± 0.34 (17)	-26.43 ± 1.07 (13)	25.11 ± 2.47 (13)
[Cr III]	16.49	12.40 ± 2.02 (4)	16.98 ± 4.86 (4)	-34.54 ± 1.56 (3)	20.24 ± 1.56 (3)	-23.60 ± 1.00 (1)	10.80 ± 1.00 (1)
[Ni III]	18.17	20.28 ± 0.15 (2)	15.36 ± 0.87 (2)	-24.54 ± 0.24 (2)	12.80 ± 1.57 (2)	-19.20 ± 1.00 (1)	25.70 ± 1.00 (1)
[S III]	23.34	15.00 ± 1.00 (1)	12.70 ± 1.00 (1)	-30.60 ± 1.00 (1)	15.10 ± 1.00 (1)	-25.90 ± 1.00 (1)	25.10 ± 1.00 (1)
[Cl III]	23.81	14.20 ± 0.30 (4)	12.44 ± 0.29 (4)	-30.98 ± 1.91 (3)	16.16 ± 1.06 (3)	-27.24 ± 0.08 (2)	25.81 ± 1.08 (2)
C II	24.38	18.63 ± 1.95 (6)	13.71 ± 0.69 (6)	-26.00 ± 2.18 (5)	21.61 ± 1.82 (5)	-23.39 ± 1.93 (2)	46.05 ± 4.30 (2)
He I	24.59	15.87 ± 0.53 (75)	15.81 ± 0.33 (75)	-29.08 ± 0.90 (66)	21.52 ± 1.23 (66)	-24.42 ± 0.60 (42)	26.51 ± 0.63 (42)
[Ar III]	27.63	15.40 ± 0.04 (2)	11.10 ± 0.04 (2)	-30.40 ± 0.04 (2)	16.10 ± 0.04 (2)	-25.00 ± 1.00 (1)	25.10 ± 1.00 (1)
[Fe IV]	30.65	21.20 ± 1.00 (1)	12.30 ± 1.00 (1)	-23.70 ± 1.00 (1)	19.40 ± 1.00 (1)	-	-
[Cr IV]	30.96	18.40 ± 1.00 (1)	12.10 ± 1.00 (1)	-25.70 ± 1.00 (1)	21.90 ± 1.00 (1)	-30.20 ± 1.00 (1)	39.40 ± 1.00 (1)
[O III]	35.12	16.13 ± 1.37 (3)	11.75 ± 0.45 (3)	-29.07 ± 1.03 (3)	17.60 ± 0.01 (3)	-25.03 ± 0.42 (3)	25.02 ± 0.70 (3)
O II	35.12	15.80 ± 0.03 (6)	12.64 ± 0.44 (6)	-29.38 ± 0.12 (6)	18.89 ± 0.43 (6)	-25.23 ± 0.68 (6)	31.78 ± 3.46 (6)
[Cl IV]	39.61	17.80 ± 1.00 (1)	10.50 ± 1.00 (1)	-27.60 ± 1.00 (1)	21.90 ± 1.00 (1)	-20.50 ± 1.00 (1)	33.10 ± 1.00 (1)
[Ar IV]	40.74	15.35 ± 1.55 (2)	11.69 ± 0.69 (2)	-29.45 ± 2.65 (2)	21.20 ± 2.20 (2)	-26.83 ± 0.07 (2)	27.88 ± 2.92 (2)
[Ne III]	40.96	15.80 ± 0.10 (2)	12.35 ± 0.05 (2)	-28.95 ± 0.05 (2)	16.22 ± 0.04 (2)	-25.90 ± 0.03 (2)	25.50 ± 0.03 (2)
Ne II	40.96	14.92 ± 0.33 (2)	14.44 ± 1.49 (2)	-26.89 ± 0.37 (2)	22.28 ± 0.14 (2)	-	-
N I	14.53	29.82 ± 0.25 (16)	9.47 ± 0.20 (16)	-29.80 ± 1.00 (1)	36.00 ± 1.00 (1)	-25.40 ± 1.00 (1)	29.40 ± 1.00 (1)
Si II	16.35	19.25 ± 2.45 (10)	19.42 ± 1.35 (10)	-29.18 ± 1.06 (8)	17.35 ± 1.78 (8)	-26.90 ± 1.16 (7)	23.89 ± 2.25 (7)
Si III	33.49	12.91 ± 1.00 (1)	13.23 ± 2.79 (1)	-31.80 ± 1.00 (1)	10.80 ± 1.00 (1)	-	-
Ne I	21.57	16.66 ± 2.38 (6)	15.66 ± 0.65 (6)	-31.78 ± 5.50 (3)	23.81 ± 2.20 (3)	-	-
S II	23.34	16.50 ± 0.69 (5)	16.69 ± 4.21 (5)	-26.88 ± 0.44 (3)	25.49 ± 3.34 (3)	-34.90 ± 1.00 (1)	33.10 ± 1.00 (1)
N II	29.60	15.07 ± 2.57 (25)	13.65 ± 1.94 (25)	-29.93 ± 1.10 (10)	18.33 ± 2.29 (10)	-25.31 ± 3.86 (7)	24.49 ± 7.94 (7)
S III	34.79	16.06 ± 0.80 (4)	13.83 ± 2.61 (4)	-29.04 ± 1.87 (4)	25.21 ± 3.48 (4)	-38.86 ± 4.34 (3)	15.85 ± 4.12 (3)
N III	47.45	11.52 ± 0.81 (2)	11.94 ± 0.16 (2)	-36.50 ± 1.00 (1)	22.70 ± 1.00 (1)	-	-

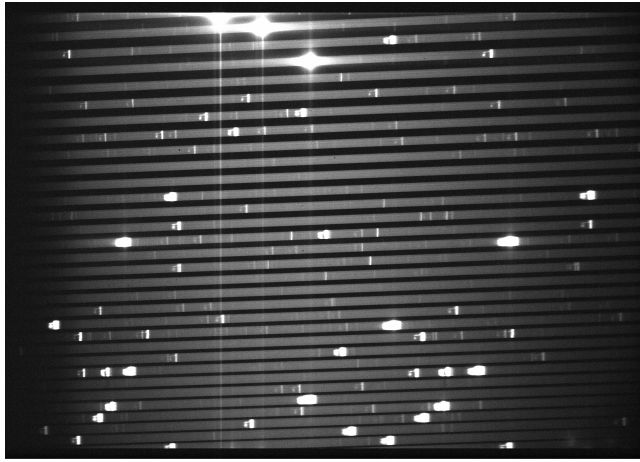


Figure A2. Image of part of the echelle orders extracted in the UVES blue arm using dichroic #2 setting ($\Delta\lambda = 3750 - 4995 \text{ \AA}$). The contrast highlights reflections in the optical system of the spectrograph that can affect some lines. We have established that order 1 is the order at the bottom and 31 at the top.

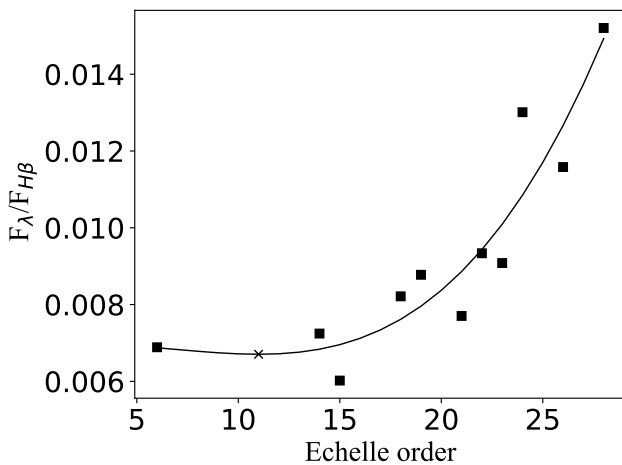


Figure A3. Least Squares fit of the flux emission for the third source of "ghost lines" in the echelle orders. The prediction for the ghost line at $\lambda = 4089.07$ (in the order 11) is marked with a cross.

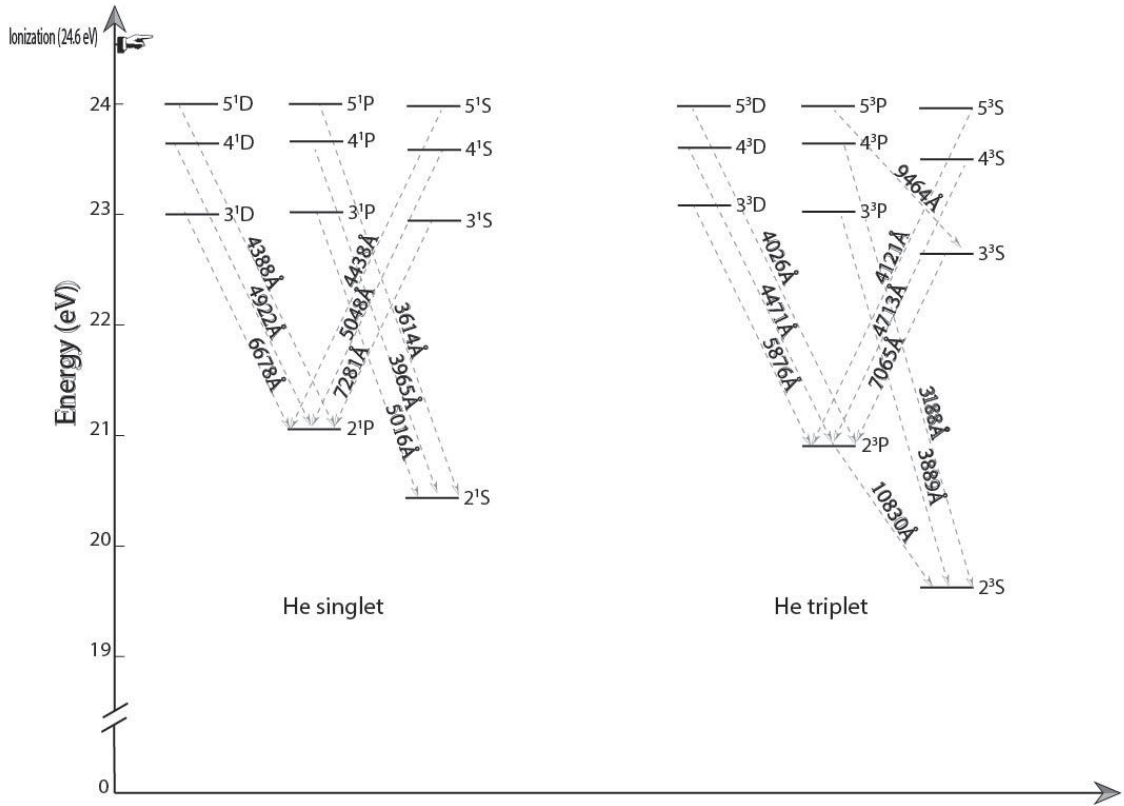
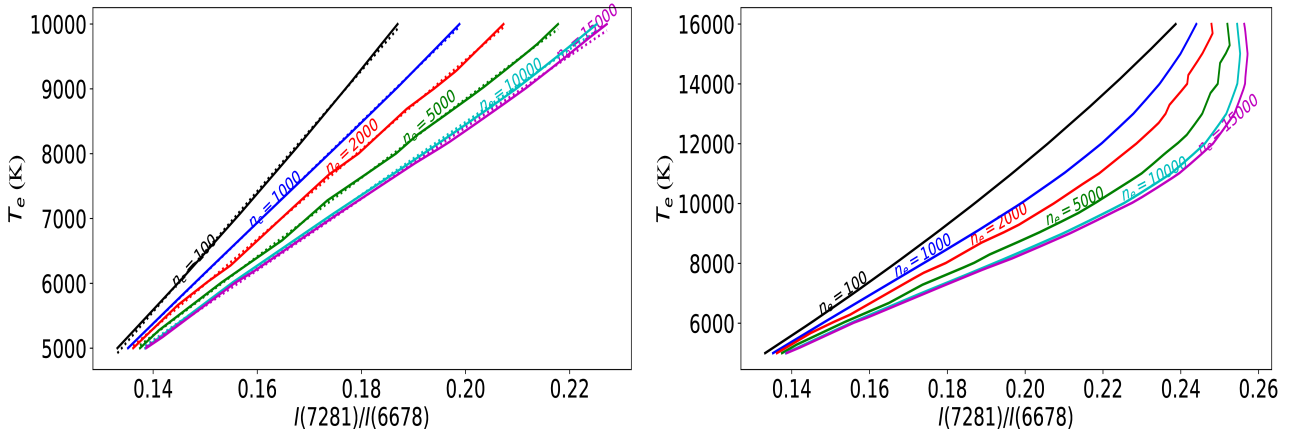


Figure A4. Grotrian diagram of He I for both configurations: triplet and singlet.

Figure A5. Dependence of $I(\text{He I } \lambda 7281)/I(\text{He I } \lambda 6678)$ on the physical conditions.



(a) A linear fit is accurate for $T_e \leq 10000$ K.

(b) A linear fit is not accurate for $T_e > 10000$ K.